Virtual staining of slide-free microscopy images with deep learning

By

TANISHQ MATHEW ABRAHAM
DISSERTATION

Submitted in partial satisfaction of the requirements for the degree of

DOCTOR OF PHILOSOPHY

in

Biomedical Engineering

in the

OFFICE OF GRADUATE STUDIES

of the

UNIVERSITY OF CALIFORNIA

DAVIS

Approved:

Richard Levenson, Chair

Randy Carney

Jinyi Qi

Orin Bloch

Faisal Mahmood

Committee in Charge

2023

“Discovery consists of seeing what everybody has seen and thinking what nobody has thought.”

– Albert Szent-Gyorgyi

Nobel Prize in Physiology or Medicine, 1937

Dedication

To my mother, Dr. Taji Abraham, who quit her PhD to raise me and has been my greatest advocate throughout my educational years.

To my father, Bijou Abraham, who has consistently provided unwavering support and guidance.

To my sister, Tiara Abraham, for being my close friend and providing encouragement.

Without the love I have received from my family, I would not be here today.

Virtual staining of slide-free microscopy images with deep learning

Tanishq Mathew Abraham

Department of Biomedical Engineering

Abstract

Histopathology is the study of tissue to look for disease. In the context of clinical medicine, it involves the microscopic examination of patient tissue samples. The standard histopathology workflow can take several hours or even days, due to the cumbersome tissue processing steps needed. This long timeline makes the standard workflow ill-suited for time-sensitive applications such as intraoperative surgical guidance. Slide-free microscopy (SFM) techniques allow for imaging of fresh tissue samples without the need for time-consuming tissue processing steps, but they often produce images that do not closely resemble conventional histology and thus may be harder to interpret by pathologists. Therefore, the present work explored the use of deep learning to convert SFM images so as to resemble hematoxylin and eosin (H&E) stained slides. This process is referred to as microscopy modality conversion or virtual staining. The dissertation focuses on virtual staining applied to three SFM methods: microscopy with ultraviolet surface excitation (MUSE), fluorescence-imitating brightfield imaging (FIBI), and quantitative oblique back illumination microscopy (qOBM).

In this work, three unpaired image-to-image translation algorithms were evaluated for MUSE-to-H&E conversion, and it was concluded that an unpaired image-to image translation algorithm based on CycleGAN (cycle-consistent generative adversarial network) proved to be the methodology that performed best. FIBI, a novel SFM technique, was shown to have significant advantages when deployed for rapid histology. CycleGANs were also developed for FIBI-to-H&E conversion, and we demonstrated clinical utility of FIBI-to-H&E conversion in a preliminary dermatopathologist validation study. CycleGANs were also applied to provide H&E-like appearance for the monochrome qOBM images;

performance was validated using a neural network classifier test and a user study with neuropathologists. Overall, the results of this work point to the general effectiveness of CycleGANs for SFM virtual staining.

This work also explored important considerations such as impact of data quality and curation on results and usefulness of transfer learning. Current limitations and future directions of virtual staining research are also discussed, such as a need for improved evaluation tools of virtual staining methods and the development of diagnostic AI with SFM-enabled by virtual staining. The virtual staining techniques explored will hopefully enable novel, alternative workflows in histopathology that utilize SFM, potentially saving time, labor, and costs in cancer screening, treatment guidance, and more.

Acknowledgements

"No one who achieves success does so without acknowledging the help of others. The wise and confident acknowledge this help with gratitude" – Unknown

I would like to acknowledge some of the people whose support I am grateful for, but I am filled with gratitude for everyone who has helped me reach this culmination of my entire academic journey.

There are people, from school teachers to college counselors to professors that took a bet on me and decided to allow a young child either skip grades or take college classes or join their lab. I am grateful to all of them. I am thankful to my second-grade teacher, Ms. Janelle Niebauer, who tirelessly sought venues for me to pursue my radically accelerated education. I especially thank my first college professor, Steve Sterling, who encouraged and supported my curiosity and passion for learning when I first took his geology college class at 7. There were also many who did not believe I was capable enough and placed many barriers in my way. Overcoming such challenges at a young age has taught me a lot about perseverance and tenacity.

I would like to thank my PhD advisor, Dr. Richard Levenson, for his support, encouragement, and guidance during this journey. Being his first graduate student and given Dr. Levenson had not gone through a PhD program, the graduate experience was a learning process for both of us. Nevertheless, I learned a lot of skills from Dr. Levenson, and I appreciated how Dr. Levenson connected me with other researchers and mentors in order to make sure I was appropriately supported. He helped me become a better scientific researcher and communicator. Being a pathologist, Dr. Levenson helped me develop an eye for histopathology and cultivated my interest in the field. His trademark humor always lightened the mood during stressful times. Glad that we both made it out alive!

I would also like to thank Prof. Farzad Fereidouni for his guidance and support throughout my PhD. I am also grateful for the support of other past and current members of the Levenson Lab: Austin Todd, Arshia Rangchi, Taryn Morningstar, and Nathan Anderson.

Thank you to my PhD dissertation committee members for all their support and guidance. My conversations with Prof. Randy Carney were always very insightful and illuminating. Prof. Jinyi Qi always asked thoughtful questions about my research with I greatly appreciated. Dr. Orin Bloch provided a beneficial clinical perspective as I pursued this research. Prof. Faisal Mahmood's expertise in AI for pathology was very valuable and he provided plenty of useful feedback.

I am grateful for the support and mentorship of Jeremy Howard, the founder of fast.ai. His fast.ai course had a profound impact on me and enabled me to transition to deep learning research. He also facilitated a very fruitful collaboration with University of San Francisco researchers and provided compute for my preliminary experiments. Over the past year, we also have had the opportunity to work closely on generative AI and medical AI projects and I have learned a lot from him. I am also grateful to the broader fast.ai community and other online communities like Kaggle and EleutherAI for all of their support and encouragement.

I am grateful for the support provided by Stability AI and its CEO, Emad Mostaque. The fellowship provided by Stability AI over the past year and a half allowed me to focus on my research without worrying about funding, and the special compute they provided greatly accelerated my research.

I am thankful for all the wonderful collaborators that I have had the opportunity to work closely with: Andrew Shaw, Prof. Daniel O'Connor, Tess Engel, Paloma Casteleiro Costa, Caroline Filan, and Prof. Paco Robles. Their insights, ideas, and feedback have all been very valuable and I greatly appreciated their support throughout my journey.

I am grateful for all the friends I have made at UC Davis, both as an undergraduate and graduate student. Throughout my 7 years at UC Davis that spanned my entire teenage years, I have made many cherished memories. Under the leadership of Chancellor Gary May, UC Davis staff and faculty, I was able to thrive in the Aggie community. I especially remember my first UC Davis class, Prof. William Tavernetti's Differential Equations who later on became a good mentor to me in my undergrad years. I

am also thankful for my extended family and our several close family friends who always share words of encouragement and celebrate each of my achievements. I am thankful for the prayers of my grandmother, Mrs. Annamma Abraham, and late grandfather, Mr. V.P. Abraham. I am also grateful to my aunts Dr. Tripthi & Dr. Trini Mathew for their encouragement.

I would like to thank all the well-wishers from around the world. Learning about how my educational journey has inspired others and the many students around the world who reach out to me sharing their aspirations has motivated me to achieve my dreams and goals.

I am also grateful that my 90-year-old grandmother, Dr. Thankam Mathew, who has been an inspiration as one of the first woman veterinarians in India to receive her PhD, is able to witness me complete my PhD. I am humbled that even at this age, she is interested in learning about my research. I also remember my late grandfather Dr. Zachariah Mathew, a veterinarian who also received his PhD. He was extremely proud of my accomplishments and was always interested to listen to my research ideas and also share his own ideas. I'm grateful he had the opportunity to see me receive my bachelor's degree and start my PhD. I am blessed with their prayers, love and encouragement.

I would like to thank my family for their constant support, advice, and especially encouragement. Without the love I have received from them, I would not be here today. I am grateful for the close bond I share with my younger sister, Tiara Abraham, who has helped me making my days less stressful with her music and jokes and has even provided feedback on my scholarly writing. As we have been paving our own unique paths, we have learned a lot from each other over the years as well. My parents have always ensured I received the best environment and resources for me to explore my passions and talents. My father, Bijou Abraham, being a talented software engineer and mathematician helped me during my early days of coding and learning calculus at 6 years old. He worked hard to provide the financial foundation for our family and to help me achieve my dreams. He has consistently provided unwavering support and encouragement to me. My mother, Dr. Taji Abraham, a veterinarian, has been my greatest advocate throughout my educational years. When I could not enroll and be on campus alone as a 7-year-old college

student, my mother enrolled in two college classes so that I could continue with my passion for learning. I will cherish the time when she was my college classmate. About 20 years ago, my mother quit her PhD in order to raise me and my younger sister. So, I am glad to now honor her sacrifices for our family and dedicate this PhD to my mother.

Lastly, I am thankful for God's blessing and the talent given to me which I hope to share with the rest of the world.

Table of Contents

Dedication iii

Abstract iv

Acknowledgements vi

Table of Contents x

1. Introduction and Background 1

1.1 - Histopathology and its use in intraoperative consultation 1

1.2 - Overview of slide-free microscopies 3

1.3 - Microscopy with ultraviolet surface excitation (MUSE) 6

1.4 - Fluorescence-imitating brightfield imaging (FIBI) 9

1.5 - Quantitative oblique back illumination microscopy (qOBM) 10

1.6 - An overview of deep learning for pathology 12

1.6.1 What is deep learning? 12

1.6.2 Common deep learning tasks in histopathology 13

1.6.3 Commonly used deep learning methodologies 15

1.7 - An overview of microscopy modality conversion 16

1.7.1 - Physics-based approaches to microscopy modality conversion 16

1.7.2 - Deep learning for virtual staining – working with pixel-paired data 17

1.7.3 - Deep learning for virtual staining – working with pixel-unpaired data 19

1.7.4 - Evaluation of virtual staining methods 20

1.8 - Summary and Objectives 22

2. Slide-free MUSE Microscopy to H&E Histology Modality Conversion 23

2.1 - Introduction 23

2.2 - Methodology 24

2.2.1 - CycleGAN 24

2.2.2 - DualGAN 25

2.2.3 - GANILLA 25

2.2.4 - Color mapping tool 25

2.2.5 - Tiled inference 25

2.2.6 - Quantitative evaluation of the models 26

2.2.7 - Datasets and implementation 26

2.3 - Results 26

2.3.1 - Training on unprocessed MUSE images 26

2.3.2 - MUSE-to-H&E translation 27
2.3.3 - Inference 27
2.3.4 - Critic training 28
2.4 - Discussion 30
2.5 Conclusion 31
3. Fluorescence imitating brightfield imaging (FIBI) for rapid slide-free histology 32
3.1 - Introduction 32
3.2 - Materials and Methods 35
3.2.1 - Typical processes for sample staining and positioning 35
3.2.2 - Optical design and components 36
3.2.3 - Image acquisition and pre-processing 37
3.2.4 - AI-based color mapping from FIBI to virtual H&E 38
3.2.5 - Effect of FIBI on downstream conventional histology and immunohistochemistry 39
3.3 - Results 40
3.3.1 - Imaging and virtual sectioning 40
3.3.2 - Conversion of FIBI images to virtual H&E appearance 42
3.3.3 - Image quality and resolution of FIBI 45
3.3.4 - High-resolution extended field of view imaging 45
3.3.5 - Block-face imaging 46
3.3.6 - Minimal impact on downstream slide preparation and molecular analysis 46
3.3.7 - 2.5-dimensional surface profiling and novel contrasts 47
3.4 - Discussion 48
3.5 - Supplementary Information 52
3.5.1 - Supplementary Figures 52
4. Pilot study of FIBI (Fluorescence Imitating Brightfield Imaging) for rapid, slide-free dermatopathology 54
4.1 - Background 54
4.2 - Methods 54
4.3 - Results 57
4.5 - Conclusion 64
5. Label- and slide-free tissue histology using 3D epi-mode quantitative phase imaging and virtual H&E staining 65
5.1 - Introduction 65
5.2 - Methods 68

5.2.1 - Label-free qOBM imaging 68
5.2.2 - Sample preparation and imaging 69
5.2.3 - Virtual H&E staining with CycleGAN 70
5.2.4 - Quantitative evaluation of virtual H&E staining results 73
5.2.5 - Computational Hardware and Software 73
5.2.6 - Clinical validation of vH&E images of brain tissue 73
5.3 - Results 74
5.3.1 - Virtual staining of label-free qOBM images of fresh mouse liver 74
5.3.2 - Virtual staining of label-free microscopy images of rat brain tumor 76
5.3.3 - Virtual H&E staining of mosaics and tomographic volumes 81
5.3.4 - Virtual staining of label-free microscopy images of human glioma specimens 82
5.3.5 - Neuropathologist validation of virtually stained qOBM images 86
5.4 - Discussion 87
5.5 - Supplementary Information 91
5.5.1 – Supplementary Notes 91
5.5.2 - Supplementary Figures 93
6. Conclusion 98
6.1 - Significance 98
6.2 - Data-centric AI and the power of simple frameworks 98
6.3 - Limitations and future directions 99
6.3.1 - Hallucinations of CycleGANs 99
6.3.2 - Alternative unpaired image-to-image translation approaches 100
6.3.3 - Alternative imaging strategies to collect paired datasets 103
6.3.4 - Virtual staining evaluation 104
6.3.5 - Incorporating the unique details provided by SFM 106
6.3.6 - Diagnostic AI with slide-free microscopy, enabled by virtual staining 107
References 109

1. Introduction and Background

1.1 - Histopathology and its use in intraoperative consultation

Histopathology is the study of tissue to look for disease. In the context of clinical medicine, it involves the microscopic examination of patient tissue samples. Typically, a clinician will collect a tissue biopsy sample or surgical resection from a patient. This tissue sample undergoes formalin fixation and paraffin embedding (FFPE) [1]. Specifically, the formalin fixation of the tissue ensures the tissue structure and morphology remains intact. The paraffin embedding allows for subsequent sectioning of the tissue. Thin tissue sections (usually about 4-6 um) are placed on microscope slides and stained with dyes that generate optical contrast for distinguishing cell nuclei, cytoplasmic components, extracellular matrix structures, and other microscopic features. The slides are primarily imaged with brightfield microscopy, where white light is transmitted through specimens that are only a few microns thick, generating contrasts based on the absorbance of the specimens. The chemical staining of the tissue specimens modulates the absorbance properties to highlight different tissue and cellular components. The most used stains are hematoxylin and eosin, which are often employed in combination (H&E). Hematoxylin preferentially stains nuclei purplish-blue, while eosin preferentially stains cytoplasm and extracellular matrix pink. This blue/pink contrast allows for close inspection of individual cells while also providing a general overview of the structure and distribution of cells.

Apart from the incorporation of digital scanning in some clinical settings, this histology workflow has remained the same for over a century, owing to its simplicity and reliability. Note, however, that this procedure is neither low cost nor quick. The standard FFPE workflow, from tissue sample to an interpreted slide, is often many hours long or longer (days, weeks, or sometimes never, depending on the accessibility of histology facilities in low-resource settings). Additionally, the chemical stains can be expensive and difficult to procure.

One important use-case of histopathology is intraoperative consultation during a surgery [2]. Specifically, an on-site surgical pathologist will examine tissue resections collected during the surgery, to identify the presence of tumor at the surgical margins and indicate if further tissue should be resected. This intraoperative guidance is crucial for surgeons to ensure complete resection of the tumor, and ensuring safe and maximally achievable resections is important for improving survival [3], [4].

Unfortunately, the standard FFPE histopathology workflow is not suitable for intraoperative guidance due to its long timeline. Instead, tissue is prepared via frozen sectioning, resulting in much shorter preparation times (~20-60 minutes). However, the frozen section procedure demands considerable expertise, produces artifacts that lead to technically unsatisfactory and difficult-to-interpret results, and is still fairly time-consuming and disruptive in the context of a surgical procedure [5].

For this reason, alternative approaches to intraoperative consultation have been developed, but they often come with disadvantages that preclude their adoption in the surgery room. Many of these technologies are aimed for *in situ* imaging of the resection site either before or after tissue resection. For example, in the context of glioma resection, intraoperative MRI technologies have been developed, but can be time-consuming and prevents the use of ferromagnetic equipment and tools in the surgery room [6]. Another promising direction is the use of exogenous fluorescence-based intraoperative imaging, but success is highly dependent on the properties of the fluorescent dye. For example, 5-aminolevulinic acid as a fluorescent contrast agent for gliomas suffers from poor sensitivity and variability [7], while indocyanine green is nonspecific and has poor stability [8]. Autofluorescence techniques that rely on endogenous fluorophores (nicotinamide adenine dinucleotide and flavin adenine dinucleotide) suffer from low specificity [9]. Additionally, all intraoperative fluorescence-based imaging relies on the use of appropriately sensitive optics and sensors.

Therefore, reimagining of the histopathology workflow may instead be a more promising route.

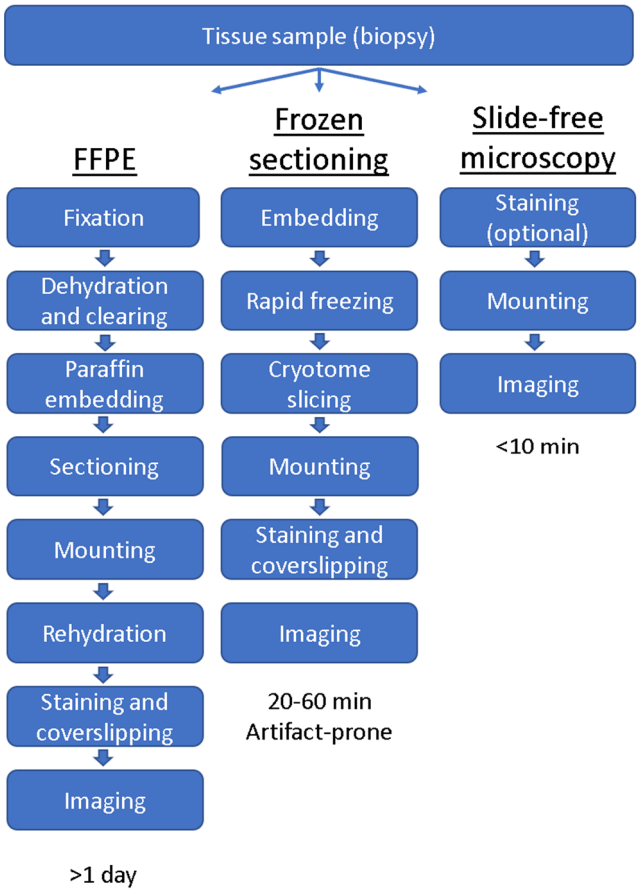

Figure 1.1 – A comparison of histopathology workflows. The standard FFPE workflow is much longer than the frozen sectioning workflow, which can be artifact prone. Slide-free microscopy does not require time-consuming tissue processing.

1.2 - Overview of slide-free microscopies

Slide-free microscopy (SFM) techniques allow for the direct *ex vivo* examination of fresh, unsectioned specimens without time-consuming tissue processing [10] and therefore overcomes the challenges of FFPE and frozen section procedures (Figure 1.1). In the context of intraoperative guidance, it allows resected specimens to be imaged within a few minutes. There is much diversity in the capabilities and functioning of a slide-free microscopy system, with some methods requiring tissue staining or clearing, requiring highly sophisticated optical setup, to others that are label-free, can have the potential to image in vivo, or utilize low-cost and simple optical setups. A SFM technique should have the following properties:

1. The ability to obtain relevant optical contrast that highlights diagnostically/clinically relevant microstructures. In standard histology, this is provided by the histological stains like H&E.
2. The ability to image a specific, often very thin, in-focus volume, eliminating other out-of-focus contributions. In standard histology, this is provided by physical sectioning.
3. The ability to image a large field of view (FOV) with a high enough resolution. There is a tradeoff between imaging speed and FOV imaged and resolution. In recent years, standard histology has relied on whole-slide imaging (WSI) scanners.
4. Have a high enough depth-of-field to account for the differences in sample surface topology. This is not an issue when working with thin tissue on slides.

A brief overview of existing SFM techniques is provided here. Please refer to Liu et al. [2] and Krishnamurthy et al. [11] for a more comprehensive review.

Confocal microscopy is one of the first microscopy techniques to be explored for slide-free histopathology applications [12]. It utilizes a point source of light, usually a laser, to illuminate a small focal spot in the specimen, and manages to provide optical sectioning by filtering the collected light through a pinhole that rejects out-of-focus light. There are two approaches to confocal microscopy: reflectance confocal microscopy (RCM) and fluorescence confocal microscopy (FCM). RCM detects light backscattering and obtains its contrast from the intrinsic optical properties of the tissue. FCM utilizes fluorophores that stain cellular structures. While confocal microscopy has some disadvantages, including slower imaging speed and higher instrumentation costs, able to provide cellular-level resolution that is useful for SFM applications. Confocal microscopy has seen significant utility in dermatopathology and has been clinically validated for such use-cases [13]. Examination of tissue specimens other than skin for histopathology applications are being investigated as well [14].

Advances in computational microscopy has enabled novel approaches to conduct slide-free microscopy. One such approach is structured illumination microscopy (SIM), which projects the illumination in user-defined patterns to enable optical sectioning [15] necessary for slide-free imaging. It

is able to image large FOVs (multi-centimeter) with submicron-level resolution at high imaging speeds (video-rate) [16].

Some SFM technologies can image tissue in a volumetric manner, enabling novel 3D histopathology applications. 3D spatial information is not available in standard histology as it only looks at a single thin cross section of a specimen. Therefore, 3D histopathology is an underexplored area, and volumetric SFM may enable a more comprehensive and accurate analysis of tissue specimens, especially those that are heterogenous [17]. Light-sheet fluorescence microscopy (LSFM) + optical clearing has been demonstrated to be a promising technique for 3D histopathology. Optical clearing refers to sample preparation techniques that reduce light scattering in a tissue specimen and improve penetration [18]. LSFM achieves optical sectioning by illuminating a thin plane with a sheet of light, and orthogonally collecting the fluorescence image [19]. By mechanically translating the sample, a 3D image can be obtained. As a fluorescence-based technique, the optically-cleared sample is usually labeled with a nuclear dye like DRAQ5, and a cytoplasmic dye like eosin. LSFM was originally explored for imaging of non-clinical specimens, but recent work has demonstrated significant potential for histopathological applications [20], [21].

Specialized optical effects can be utilized as well to develop SFM technologies. These include multiphoton microscopy (MPM) and Raman scattering. MPM uses multiple photons, typically from the near-infrared spectrum, that arrive nearly simultaneously at excitable molecules to induce fluorescence, with a potential for less photodamage and deeper tissue observation than is provided by regular one-photon excitation fluorescence, and even tissue staining. Fluorescence from exogenous labels or endogenous biomarkers (autofluorescence) can be utilized. There are several MPM microscopy approaches, such as two-photon excitation fluorescence (TPEF), second harmonic generation (SHG), and third harmonic generation (THG). MPM techniques unfortunately require expensive high-power ultrafast lasers to induce the special optical effects. MPM has been explored for assessing breast pathologies [22], brain tumors [23], and more [24], [25].

In addition to optical effects, other optically related physical phenomena can be exploited. Photoacoustic microscopy (PAM) exploits the phenomenon where the tissue absorbs light and converts that energy into heat, which leads thermal expansion, resulting in the release of a wide-band acoustic wave [26], [27]. The photoacoustic system utilizes a nanosecond-pulsed laser to elicit this effect and produce an image with an ultrasonic transducer. Numerous slide-free microscopy applications have been explored, such as for imaging breast tissue [28] and bone tissue [29].

In this dissertation, I will focus on three other SFM methods which are described in more detail in later sections: microscopy with ultraviolet surface excitation, fluorescence-imitating brightfield imaging, and quantitative oblique back illumination microscopy.

1.3 - Microscopy with ultraviolet surface excitation (MUSE)

Microscopy with ultraviolet surface excitation, or MUSE, is a recent SFM technique with significant promise for applications in histology [30]. This technology relies on the observation that sub-300 nm wavelength ultraviolet (UV) light has a short penetration depth in tissue of about a few μm deep, similar to the thickness of a standard histology slide. Therefore, the excitation volume is limited to a thin layer that corresponds to the optical sectioning of brightfield microscopy, allowing MUSE to achieve high-contrast sub-cellular-scale imaging with thick tissue specimens. Luckily, common fluorescence dyes such as Hoechst, 4',6-diamidino-2-phenylindole (DAPI), and rhodamine can be excited by this sub-300 nm light and emit in the visible range. The emission can then be captured using simple-to-operate and inexpensive conventional glass-based microscope optics and a standard color camera.

The optical system is comprised of a UV light-emitting diode (LED) and UV-compatible sample stage (Figure 1.2A). As the glass microscope lens is opaque to the sub-300nm light, the specimen is illuminated in an oblique manner. The opaqueness of the lens serves as an intrinsic excitation filter. Additionally, the oblique illumination can also generate shading across the face of a specimen that highlights tissue surface topography.

Note that the UV excitation used by MUSE also introduced several design challenges and concerns. Since standard glass microscope lenses are opaque in that spectral range, MUSE uses obliquely angled illumination that bypasses the objective. This general configuration makes it difficult to use high-NA, high-magnification lenses with typical short working distances, as it is difficult to get such objectives close enough to the tissue without physically blocking excitation. This also requires the sample support or viewing window to be composed of quartz or sapphire, rather than less expensive glass. In addition, UV excitation intensities that can be generated using the comparatively low-power LEDs currently available result in exposure times in the 100's of milliseconds per image, which can lengthen scan times for larger specimens.

MUSE imaging is non-destructive: it does not interfere with subsequent standard FFPE histology or any sort of molecular analyses like immunohistochemistry, fluorescence in situ hybridization, DNA/RNA expression measurements, etc.

MUSE images can resemble the contrasts seen in conventional histology, but also differ in various ways. For example, the three-dimensional nature of the tissue surface can be appreciated (sometimes referred to at 2.5D imaging) in Figure 1.2B. Additionally, there is a greater diversity in staining contrasts and colors (Figure 1.2C). These unique contrasts may be useful for diagnostic applications and scientific discovery, but the differences from conventional histology may also be a hindrance for clinical applications.

In order to assess its clinical potential, Fereidouni et al. [30] conducted a preliminary validation study where 42 cases comprising of both benign and malignant specimens were imaged by MUSE. The diagnoses made by one pathologist viewing the MUSE images were compared to the diagnoses made by another viewing the H&E images, and a concordance rate of 93% was observed. A similar validation study was conducted specifically for dermatopathology by Qorbani et al. [31].

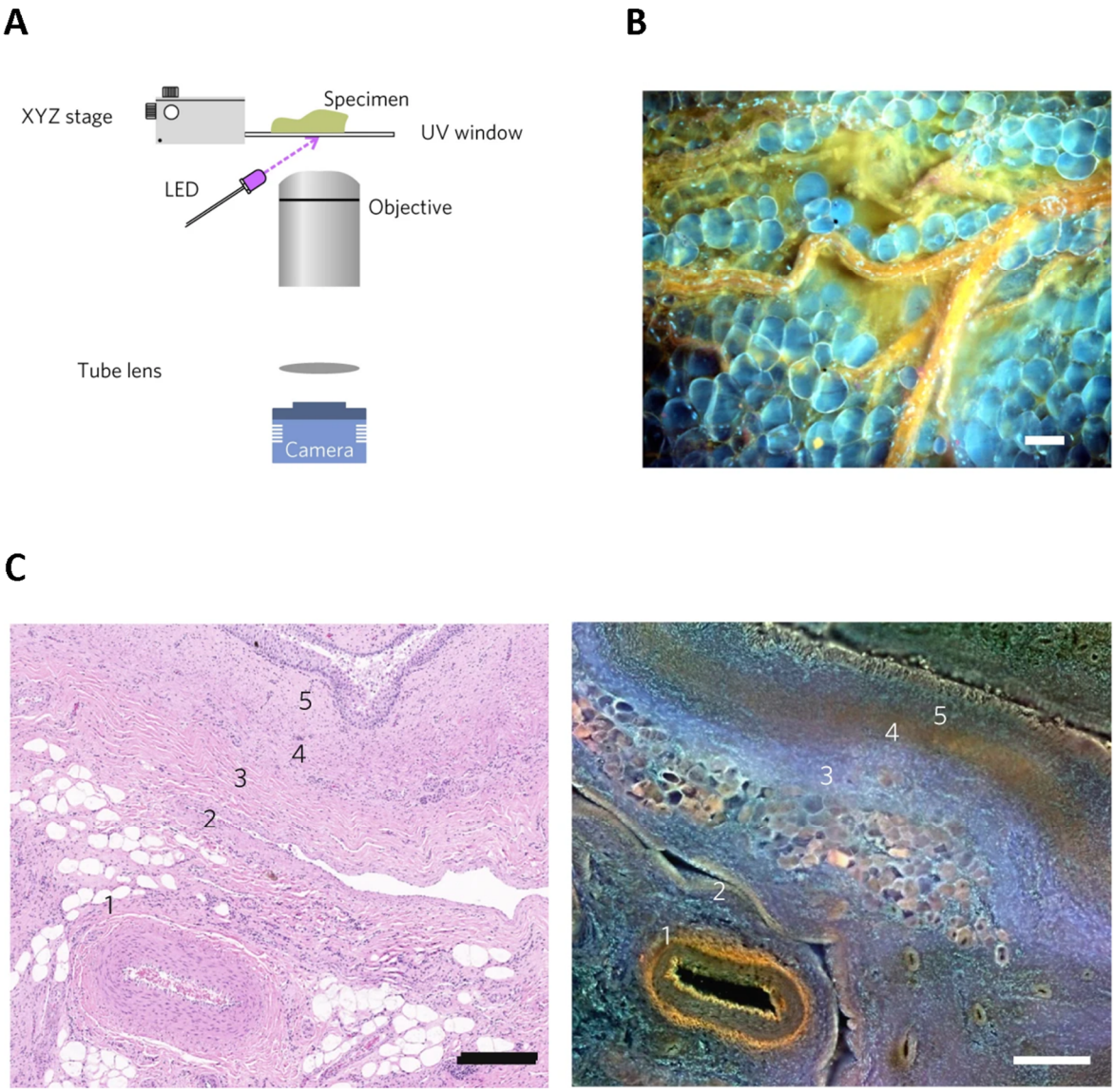

Figure 1.2 – A) A schematic diagram of the MUSE optical design. **B)** Fresh breast tissue with nerve coursing over and through a layer of intact adipocytes (rhodamine and Hoechst). **C)** Side-by-side comparison of fixed porcine renal tissue imaged by H&E and MUSE. Stromal features, some identified by number, are easier to distinguish in the MUSE image. Scale bars, 100 μm.

Numerous extensions variants of MUSE have been developed in recent years, all relying on the basic mechanism of limited UV tissue penetration for optical sectioning. For example, Liu et al.

implemented a compact and inexpensive version of MUSE [32], while Yoshitake et al. explored the use of water immersion to improve MUSE's optical sectioning [33].

1.4 - Fluorescence-imitating brightfield imaging (FIBI)

Another slide-free microscopy method, known as fluorescence-imitating brightfield imaging (FIBI), has been developed recently to allow for cost-effective and rapid imaging of thick tissue specimens (Fereidouni et al., manuscript in preparation, described further in Chapter 3). FIBI relies on applying a thin layer of absorbing dyes to the surface of the tissue to limit the penetration of illumination light and imaging volume to the surface. This allows imaging the tissue using a very simple yet efficient and reliable approach by implementing standard epi-fluorescence illumination and imaging the fluorescence and absorption contrast to create the image.

Conveniently, stains extremely familiar to histopathologists, that is, hematoxylin and eosin, perform very well in this application (although FIBI is not limited to these stains). Hematoxylin is a strongly absorbing, and non-fluorescing dye that binds predominantly to nuclei, but depending on the formulation, will also stain other tissue elements to a lesser extent. It usefully signals the presence of RNA species in cytoplasm, a phenomenon that often reflects the presence of translationally active cells. Experiments indicate that after 30s staining of human kidney with hematoxylin, it only penetrates 10 μm inside the tissue. Eosin penetrates deeper and it provides a nice complement, generating a pink tint to the overall tissue surface elements, just as it does in conventional slide-based histology. The combination of tissue autofluorescence and eosin fluorescence generates a diffuse backlight arising mostly from below the surface of the specimen. A portion of this backlighting returns through the surface of the specimen to be collected by a conventional microscope objective and transmitted to a standard color camera.

Like MUSE, FIBI is able to provide subcellular contrast with remarkable clarity. It is also non-destructive and does not interfere with subsequent standard FFPE histology or molecular analyses. FIBI differs from MUSE in that FIBI images more immediately resemble those encountered using standard brightfield rather than fluorescence-based microscopy (especially due to its use of similar stains).

Moreover, MUSE needs UV-compatible viewing windows but because FIBI operates in the visible spectrum, it can be used with regular glass and a standard through-the-objective epifluorescence optical path. Bright, visible-range excitation LEDs allow exposure times as short as 5 ms per field, and thanks to the epi-illumination design, it is straightforward to deploy a variety of low- and high-magnification objectives. The short exposure times required allows for rapid XY scanning and also the acquisition of multiple Z-axis images that can be used to achieve extended depth of focus (EDOF) captures necessary to accommodate specimens with somewhat irregular (i.e., not completely flat) surfaces.

Borowsky et al [34] conducted a clinical validation study where 100 surgical specimens were imaged with FIBI, then processed by the standard histopathology workflow. The resulting digital images from both FIBI and H&E scans were viewed in random order and modality by four reading pathologists. After a 30-day washout, the same 100 cases, in random order, were presented in the alternate modality to what was first shown, to the same four reading pathologists. The agreement rate, compared the reference diagnosis, was 97.0% for the 400 FIBI reads and 98.8% for the 400 H&E reads.

Chapter 3 provides a more in-depth description of FIBI, its mechanism, demonstration of image capabilities, etc.

1.5 - Quantitative oblique back illumination microscopy (qOBM)

One disadvantage of many existing SFM techniques is that they often require labeling of the tissue in some way. Some SFM technologies may be label-free, such as PAM, MPM, and RCM. However, they often rely on expensive and sophisticated optical setups or do not provide adequate resolution and contrasts.

Quantitative oblique back illumination microscopy (qOBM) is a label-free, wide-field, low-cost microscopy technique capable of obtaining cellular and sub-cellular resolution quantitative phase images of thick, scattering tissue samples via epi-illumination [35], [36]. As a label-free imaging technique, qOBM does not require any exogenous stains, and can thus provide images that are free of any staining

and processing artifacts. Further, qOBM achieves a level of cellular and subcellular detail in 3D that is only rivaled by label-free nonlinear microcopy methods, but with an embodiment that is simple and orders of magnitude cheaper (e.g., uses LEDs instead of femto-/pico-second lasers), is faster (wide-field vs point scanning), is gentle on tissues and cells, and can be easily modified and miniaturized for in-vivo applications.

The qOBM system consists of a conventional inverted microscope with a modified epi-illumination scheme. The illumination consists of four LED light sources (720nm) coupled into 1mm multimode fiber optics with a 0.5 numerical aperture (NA). The fibers are evenly distributed around the microscope objective at a 45-degree angle. LEDs are illuminated sequentially, and for each illumination, a raw capture is collected. When light from an LED source is introduced through one of the fibers into a thick scattering sample, the light in the specimen undergoes multiple scattering events, causing some photons to change trajectory and serve as a virtual light source within the specimen. This is known as oblique back-illumination and it allows for the capture of a phase contrast image of the sample. If two captures obtained from illuminating with diametrically opposed LEDs are subtracted, we can obtain a differential phase contrast (DPC) image. Because out-of-focus contributions from either illumination side are essentially the same, the subtraction process rejects out-of-focus content, allowing for tomographic sectioning. To reconstruct a qOBM quantitative phase image, two DPC images from orthogonal angles are processed and deconvoluted with the system's optical transfer function which is determined through numerical photon transport simulations (see [35], [36] for more details).

qOBM has been miniaturized into a handheld probe setup, which will enable novel in vivo applications of the technology [37]–[39]. Instead of needing to resect a tissue specimen in order to image it, the tissue can be directly imaged in vivo during surgery.

qOBM imaging and related technologies have been explored for several applications, including intraoperative guidance for brain glioma resections [37], sickle cell disease progression [40], and organoid development [41].

Note that while MUSE, FIBI, and qOBM may appear to be SFM technologies with distinct mechanisms, they share similarities. For example, both FIBI and qOBM rely on a backlight to illuminate the surface of the specimen. FIBI obtains that backlight from tissue autofluorescence and eosin fluorescence, while qOBM obtains it from scattering. Additionally, both MUSE and qOBM utilize oblique illumination. Finally, MUSE, FIBI, and qOBM all are quite easy to implement and inexpensive.

1.6 - An overview of deep learning for pathology

This dissertation focuses on the application of deep learning to enhance slide-free microscopies for histopathological applications. Therefore, it is worth introducing how deep learning is used in histopathology and microscopy.

1.6.1 What is deep learning?

Deep learning is a subset of machine learning, which itself is a subset of artificial intelligence. Machine learning refers to the training of programs developed by allowing computer to learn from its experience and data [42], [43]. This differs from the classical approach to algorithm development that requires manual coding of the exact steps to solve a task. There are many tasks where doing so is difficult (what are the exact steps for recognizing a cat in an image, accounting for all possible variations?), and this is where machine learning shines. Deep learning refers to the use of artificial neural networks to perform this learning.

Deep learning has been applied to virtually every field, from natural language processing (answering textual questions, building chatbots, classifying documents, etc.) to computer vision (face recognition, image captioning, etc.), image generation (super-resolution, colorization, text-to-image, etc.), recommendation systems (product recommendations, social network algorithms, etc.), and so much more [43]. Most applications in pathology fall under the class of computer vision, as the data being processed are usually whole slide images.

Artificial neural networks, at its core, is very simple. A neural network is comprised of multiple layers. Each layer takes some input, performs some mathematical operation on it, and then passes the result to the next layer. The final layer produces the prediction of the neural network. The mathematical operations performed by the layer can be quite simple, usually some sort of linear transformation:

$$y = Wx + b$$

where x is the input of the layer, y is the output of the layer, and W,b are parameters (also called weights) of the layer. Note that a neural network some sort of nonlinearities as well, which makes the neural network highly flexible:

$$y = \sigma(x)$$

where x is the input (comes from the previous layer), $\sigma(\cdot)$ is the nonlinearity function (example include sigmoid, tanh, ReLU, etc.), and y is the output. It can be mathematically proven that the incorporation of these nonlinearities enable a neural network to approximate any function (universal approximation theorem) [42], [43].

A neural network can learn from data by adjusting the parameters of each layer based on the feedback it receives from a loss function, which measures how well the model is performing. The process of adjusting the parameters is called optimization, and many optimization algorithms exist, like stochastic gradient descent, Adam, etc. [44]

1.6.2 Common deep learning tasks in histopathology

In histopathology, there are several tasks that can be assisted through the application of deep learning technologies. Most of these problems fall into four classes: classification, segmentation, image translation, and image style transfer. Here, we will briefly define these tasks and explain how problems in histopathology can be formulated as common machine learning tasks. In all cases, we focus on image tasks, as this is most relevant to histopathology.

Image classification refers to the task of assigning a label to an image. Much of the field of histopathology is comprised of various classification tasks. This is since histopathology is mainly focused on assigning a diagnosis based on review of slide-based microscopy. Automatic classification of tissue structures and subtypes can also be extremely useful to augment and improve the histopathology workflow. As a central problem in computer vision and machine learning, the methodologies for solving classification problems have been broadly explored in both academic and well-funded commercial enterprises and considerable progress has been made. The leading algorithms for image classification are convolutional neural networks (CNNs), which have demonstrated better-than-human performance on various benchmark datasets for both general image classification tasks [45]–[50] and pathology-specific tasks [51]–[53], although their real-world performance across novel institutions and differently curated collections remains to be determined.

Image segmentation refers to the task of assigning labels to specific regions of an image. It can also be seen as a pixel-level classification task. Segmentation of subcellular structures, such as nuclei and cytoplasm and membrane compartments, can be useful for automating common tasks such as cell enumeration (via nuclei counting), determination of intracellular locations of molecular markers, and is important for analysis of subcellular morphological features such as nuclear size, eccentricity and chromatin texture [54]. Automatic segmentation can also be used to help pathologists recognize tissue components by delineating different tissue types. Some image microscopy problems can be reformulated as segmentation problems. More importantly, the most common deep learning architecture for segmentation, U-nets, is often utilized for image enhancement tasks, as we will see later.

Image-to-image translation refers to the conversion of one image representation to another image representation. The goal is to learn the transformation between the input and output images. This can be applied to a wide variety of applications, such as converting between night and day images, winter and summer images, or more useful tasks like converting satellite images to maps. In computational pathology, image-to-image translation has been explored for stain color normalization and for converting

between different image modalities (which is the focus of this dissertation). The most common models used for image translation tasks are generative adversarial networks or their variants (Section Generative adversarial networks and their variants).

1.6.3 Commonly used deep learning methodologies

A convolutional neural network (CNN) belongs to a class of deep learning algorithms most commonly used for image tasks such as image classification. The building blocks of a CNN are learned convolutional kernels [42]. These convolutional kernels are applied to the image and their subsequent representations in the neural network in order to extract learned features. The convolutional kernels are developed during the training process. A key advantage of convolutional layers is their shift invariance [42]. As the convolutional kernel is applied over the entire image, shifts in the input shift the output in an equivalent manner. This is an especially useful property for microscopy. The stacking of convolutional layers and other layers such as fully connected layers and pooling layers are used to build CNNs. A variety of CNN architectures have been developed, but some network architectures are more commonly used due to their generalizability and effectiveness over a wide variety of tasks. Some of the most common architectures include VGG nets [48], ResNets [49], and Inception nets [50]. For many computer vision tasks, there is little data available for successful training of CNNs from scratch. However, the knowledge of models trained on larger datasets can be transferred for application to learning cycles applied to a smaller, focused dataset [55]. This takes advantage of the fact that many of the convolutional layers derived from large-dataset-derived models serve to extract general, low-level features. Therefore, only some of the layers of models that were pretrained on larger datasets are subsequently retrained on the smaller dataset. This process is known as transfer learning.

A wide variety of algorithms and deep learning architectures [56], [57] are used for image segmentation, but undoubtedly the most common neural network architecture for image segmentation is the U-net [58]. Ronneberger et al. originally introduced U-nets specifically for biomedical segmentation, but this approach has now been used across a variety of segmentation problems. While U-nets were

originally developed for segmentation, they have been used for a variety of image-to-image translation tasks such as achieving computational super-resolution [59]. With some 10,000 citations already reported in Google Scholar, the U-net architecture is clearly one of the most influential deep learning architectures developed to date.

A generative adversarial network (GAN) is a deep learning method that was pioneered by Goodfellow et al. [60] and leverages multiple neural networks working "against" each other to transform images of different classes. The basic premise is that one neural network (the "generator") is trained generated synthetic images, for example, generating images of cats. The second neural network (the "discriminator") is trained to discriminate real images of cats from fake images generated by the first network. This is done cyclically until the images generated cannot be classified accurately as generated or real by the discriminator. The potential for this method has been continually explored and expanded since its original description in 2014; it has found many applications, such as in super-resolution [61] and artistic endeavors [62].

1.7 - An overview of microscopy modality conversion

Slide-free and label-free microscopies often provide contrasts and visualizations that are unlike standard histology and may therefore be harder to interpret, making these techniques more difficult for histopathologists to adopt. Therefore, converting novel modalities to resemble H&E-stained slides (or vice-versa) may allow for a wider adoption of these modalities. This general process of converting one microscopy modality into another (usually brightfield microscopy with H&E stain) is referred to as microscopy modality conversion or virtual staining. Virtual staining isn't limited to slide-free microscopy, and slide-based microscopy techniques have also been virtually stained.

1.7.1 - Physics-based approaches to microscopy modality conversion

Various techniques have been explored for converting images produced by alternative microscopy modalities into H&E-like images to improve visualization. Before the introduction of machine learning

algorithms, algorithms based on relevant physical models were developed. For example, Gareau et al. assumed that there are separate fluorescence/reflectance channels for nuclear and cytoplasmic signals and uses them to weight hematoxylin and eosin colors to form a pseudo-colored image [63]. Similar methods, where separate nuclear and cytoplasmic signals were used to re-weight predetermined H&E colors, have been used for MPM [22] and stimulated Raman spectroscopy [64]. Giacomelli et al. aimed to develop a more physically accurate model in which it is assumed that separate fluorescence signals are weighting hematoxylin and eosin colors based on the Beer-Lambert law for rendering final color mixtures [65]. A similar model was used in Fereidouni et al. for pseudo-H&E coloring of MUSE images [30]. Here, it is assumed that nuclei may not be labeled by a single fluorophore, and the detected nuclear RGB "spectrum" can be corrected using available unmixing methods before remixing them into a pseudo-H&E image.

Note that these simple models for microscopy modality conversion only render the color of the underlying image to match the stains, and do not affect the morphology in any way.

1.7.2 - Deep learning for virtual staining – working with pixel-paired data

Recently, deep learning has been used to develop novel microscopy modality conversion algorithms, with often superior results [66]. Here, we describe a subset of the recent developments.

A pioneering work in virtual staining research is Rivenson et al. [67], which investigated the use of deep learning to virtually stain unlabeled tissue-autofluorescence images. They trained neural networks on salivary gland tissue stained with H&E, kidney tissue stained with Jones stain, and liver and lung stained with Masson's trichrome. The neural networks were convolutional neural networks (CNNs) of the U-net architecture (a standard architecture for any image-to-image task). The networks were trained via the generative adversarial network (GAN) framework, an approach that has been quite successful in a variety of image synthesis tasks. The GAN-trained neural network performed very well converting the images, with considerable detail generated, and accurate histopathological features captured in the virtual images. The virtually stained images were also evaluated by pathologists, and no significant difference

between the virtually stained and regular brightfield images was observed. This indicates the virtually stained images can provide similar diagnostic utility. The variation in the colorization of the virtually stained images is lower than that of the histologically stained images. Therefore, intrinsic staining standardization is an interesting positive by-product of this approach.

Quantitative phase imaging (QPI) is a relatively recent class of label-free imaging technique (very closely related to qOBM) with lower phototoxicity that can be deployed on various platforms (including portable platforms). In order to bridge the gap between QPI and standard histopathology, Rivenson et al. [68] again used a GAN-based approach to convert phase-based microscopy images to histological images. Three models were trained for H&E for skin tissue, Jones' stain for kidney tissue, and Masson's trichrome for liver tissue. The models were then applied to similar images that were not present in the training set. They utilize a custom global co-registration method and elastic image registration for local feature registration. Similar to [67], U-net architecture is used for the generator, with H&E images converted to YCbCr color space passed as the input. With fast inference time, and by removing the need for staining, this technology has the potential to reduce labor and time costs. While lens-free holographic microscopy was used, this algorithmic approach could be applied to other QPI techniques.

In certain settings, staining procedures can result in irreversible modifications or damage; this is usually regarded as disadvantageous as it can preclude further analysis of the tissue. However, this is particularly true in the special case of sperm cell selection for in-vitro fertilization (IVF) due to the potential cytotoxicity of staining. Interferometric phase microscopy (IPM) is currently used for sperm evaluation, as it is compatible with available medical microscopes which are modified with an additional wavefront sensor to allow for holographic microscopy. This combination provides quantitative topological maps of the cells without the need for stains. However, morphological evaluation of cells is most effectively accomplished using chemical staining of cell organelles. A method, “HoloStain,” was therefore developed to convert quantitative phase images and phase gradient images, which are extracted from the digital holograms, to virtually stain brightfield images using GANs [69]. For each cell, an

ensemble of four images was used to train the model: stain-free quantitative phase image, two stain-free phase gradient images, and the target-stained brightfield image. An advantage of HoloStain is that cells that were out of focus could be virtually stained and refocused. This is possible since digital reconstruction of the holograms can be done such that unfocused cells can be brought into focus. In order to demonstrate the usefulness of the algorithm, sperm cells were classified by an embryologist using data from brightfield images (no staining), stain-free quantitative phase images, one of the stain-free gradient images, and HoloStain images. The HoloStain method had the best performance compared with the alternative three methods.

One important note about the previously described deep learning-based virtual staining methods is that they are usually still imaging (often unstained) thin tissue sections. Therefore, the target image can be easily obtained by staining the thin tissue section and imaging it (followed by image registration). To emphasize, these deep learning-based methods rely on the availability of stained images that are paired and pixel-registered to original modality images to use as ground truth. With this level of supervision, the neural network is able to be trained easily with an objective that minimizes the difference between the neural network-predicted virtually stained image and the ground truth stained image. Tasks that require pixel-matched (input ground truth) pairs are referred to as paired image-to-image translation in computer vision. This is therefore the paradigm that most virtual staining approaches follow.

1.7.3 - Deep learning for virtual staining – working with pixel-unpaired data

Note that in many cases, this level of pixel-wise supervision can be challenging or even impossible to obtain for SFM virtual staining applications. For instance, if we take a tissue specimen and image with MUSE or FIBI or qOBM, followed by FFPE processing and obtaining an H&E slide, the general features are very similar, but the exact structures will not be matched. This is a major challenge that has hindered the application of virtual staining to SFM applications.

In order to address this issue, an unpaired image-to-image translation framework can be utilized. This computer vision framework enables the learning of a transformation from images in some input

domain A to images in some input domain B from a collection of domain A images and domain B images that are not necessarily paired/registered. For SFM virtual staining, domain A would be the SFM images and domain B would be the stained images. There are several approaches that have been explored in the computer vision and deep learning literature, but the most commonly used unpaired image-to-image translation algorithm is the CycleGAN model.

Combalia et al. converted confocal microscopy images utilizing CycleGANs [70]. The RCM and FCM images are linearly combined to form an RGB image, by assigning RCM images an eosin-like color, and FCM images a hematoxylin-like color. This naively converted image is then passed into the CycleGAN. Importantly, it was demonstrated that deep learning-based despeckling is important for successful virtual staining. Without it, the CycleGAN generated unwanted artifacts.

Similar to [70], Cao et al. explored the use of CycleGANs for photoacoustic microscopy of bone tissue [29]. Significant agreement was observed between the virtually stained images and the standard H&E images, as determined by statistical analysis of nuclear features and review by three pathologists and one orthopedic surgeon.

1.7.4 - Evaluation of virtual staining methods

In order to assess the virtual staining methods, various qualitative and quantitative analyses have been utilized. When paired input and ground truth images are available, standard image similarity metrics like SSIM, PSNR, MS-SSIM, and MSE can be utilized.

Evaluation is significantly more challenging for unpaired datasets due to the lack of a pixel-matched ground truth for a given image. Evaluation in these scenarios can be divided into two classes: style transfer evaluation and content preservation evaluation.

Style-transfer metrics will provide information about how well the stain “style” is transferred to the SFM images during the conversion process. Reference-free metrics like Frechet Inception Distance (FID) or Inception Score (IS) can be used for this purpose. These metrics compare the distribution of

image features (provided by a pretrained neural network) extracted from the generated images to the real images. Since this metric measure the distribution-level differences, individual ground-truth images are not needed. However, these metrics simply measure if the generated images look like a real image (i.e. if the staining style is present) and does not appropriately measure if the content of the original image is maintained. For example, a model could take SFM images but output random H&E-like images with no correspondence to the input and still achieve high performance according to FID and IS.

Another quantitative evaluation method utilized for virtual staining is to extract (either with simple and well-tuned computer vision algorithms or specialized neural networks) histological features from the virtually stained images and the actually stained images. Some commonly used features include segmented nuclei, glands, tumor vs stroma regions, etc. Distributions of quantities like average nuclear count, area, etc. can be then compared between the virtually stained images and ground truth images. Once again, these metrics would not indicate if the content of the original image is maintained. A model could generate random H&E-like images with similar nuclear size and number of nuclei to the actual H&E images, with no regard to the content of the input SFM images.

While these style transfer metrics are useful, it must also be complemented by an evaluation of content preservation. Histological features from the original image must be preserved: it would be disastrous if a virtual staining method took features in the SFM image that represent tumor and convert them to stroma in the virtually stained image. Additional neural networks can assist in the quantification of this content preservation. For example, Ozyoruk et al. evaluated virtual FFPE H&E staining of frozen sections by applying FFPE H&E-trained diagnostic subtyping neural networks to the virtual FFPE H&E images and evaluating its accuracy [71]. However, there is overall limited use of content preservation metrics in the literature.

While quantitative metrics can provide some insights into the performance and utility of the virtual staining model, pathologists and clinicians serve as the end users of any such technology, and results from case studies with pathologists likely serve as the best indicator of clinical utility. Several

virtual staining studies do indeed utilize pathologist validation studies to demonstrate their potential clinical utility [67], [68], [71], [72].

1.8 - Summary and Objectives

In this chapter, I discussed what is histopathology and its important use-cases, like intraoperative consultation during surgery. I also discussed alternative approaches to histopathology with SFM. Then, an overview of deep learning for histopathology is briefly discussed. Finally, the specific task of virtual staining is described.

In this dissertation, the development of deep learning-based virtual staining methods for three SFM methods (MUSE, FIBI and qOBM) is detailed. Chapter 2 focuses on the exploration of MUSE-to-H&E modality conversion. Chapter 3 describes the FIBI technology in further detail, while exploring the virtual staining methods. Chapter 4 focuses on FIBI virtual staining for dermatology applications, with a dermatopathologist case study. Chapter 5 describes the use of virtual staining of qOBM to potentially enable novel clinical applications, as demonstrated by a neuropathologist case study. Finally, Chapter 6 outlines some potential future directions for this work.

2. Slide-free MUSE Microscopy to H&E Histology Modality Conversion

2.1 - Introduction

Microscopy with ultraviolet surface excitation (MUSE) is a novel non-destructive, slide-free tissue imaging modality for histology [73]. Using MUSE instead of conventional histology processing eliminates the need for fixing and thin-sectioning the tissue. While MUSE has been evaluated for many purposes, the current gold standard in medicine and biological research for tissue sample analysis is still based mainly on brightfield imaging of H\&E-stained tissue slides; these dyes color cell nuclei blue and cytoplasm pink, respectively. MUSE dyes, on the other hand, typically involve DAPI or Hoechst dyes for nuclei, and rhodamine for the other tissue components [73]. The resulting images thematically resemble H&E, but the colors generated by the UV excitation light impinging on these dyes are dramatically different from the traditional brightfield hues.

In order to bridge the gap between MUSE imaging and traditional histological examination, it is possible to digitally modify the MUSE images to match H&E images. In [73], a spectral unmixing color mapping model was used, but it required user input of expected colors and is limited to conversion of nuclear and cytoplasm colors, failing to handle cases in which a larger gamut of colors are generated. Therefore, we aim to utilize deep learning methodologies in order to learn the appropriate transformation for generating visually convincing virtual H&E images that works well on a variety of tissue and cell types.

Deep learning has been used successfully in microscopy modality conversion tasks like the one we present here, [74]–[76]. These modality conversion algorithms often use a generative adversarial network (GAN) framework [77]. In this case, the generator needs to be trained with the input modality image and a corresponding output modality image. Therefore, paired image datasets are required for modality-converting GANs. Unfortunately, it is not possible to obtain exact pixel-aligned H&E and

MUSE images. Therefore, we investigated unpaired image-to-image translation methods that eliminate the need for precisely paired datasets.

We propose a framework for training and applying an image-to-image translation GAN-based algorithm for successful conversion of MUSE images to virtual H\&E images. We evaluated CycleGAN [78], DualGAN [79], and GANILLA [80] for MUSE-to-H&E conversion. We hope that our framework will help catalyze the adoption of MUSE and improve the efficiency of the pathologist's workflow.

2.2 - Methodology

We define two image domains, one for MUSE images (X), and one for H&E images (Y). We attempt to determine the transformation $G: X \rightarrow Y$. In our framework, we have two tasks. One task is to learn a generator $G_X: X \rightarrow Y$ that maps $x \in X$ to $y \in Y$. The auxiliary task is to learn a generator $G_Y: Y \rightarrow X$. Additionally, we have the adversarial discriminators D_X and D_Y. D_X discriminates between the fake outputs of G_X and real images from domain Y. Conversely, D_Y discriminates between the fake outputs of G_Y and real images from domain X. These two GANs form the training framework for MUSE-to-H&E conversion. CycleGAN, DualGAN, and GANILLA all follow this framework and only differ slightly in model architectures, loss functions, and training procedures.

2.2.1 - CycleGAN

CycleGAN exploits the cycle-consistency property that $G_Y\big(G_X(x)\big) \approx x$ and $G_X\big(G_Y(y)\big) \approx y$. This constraint can be expressed as the following loss:

$$\mathcal{L}_{cycle}\,(G_X, G_Y) = \mathbb{E}_{x\sim p_{data}(x)}\left[\left\|G_Y\big(G_X(x)\big) - x\right\|_1\right] + \mathbb{E}_{y\sim p_{data}(y)}\left[\left\|G_X\big(G_Y(y)\big) - y\right\|_1\right]$$

where $\|\cdot\|_1$ is the L_1 norm.

Additionally, the GANs are trained with the traditional adversarial losses [78]. Finally, for regularization, we impose an "identity" constraint:

$$\mathcal{L}_{identity}(G_X, G_Y) = \mathbb{E}_{y \sim p_{data}(y)}[\|G_X(y) - y\|_1] + \mathbb{E}_{x \sim p_{data}(x)}[\|G_Y(x) - x\|_1]$$

The generator architecture is a ResNet-based fully convolutional network described in [78]. A 70x70 PatchGAN [81] is used for the discriminator. The same loss function and optimizer as described in the original paper [78] was used. The learning rate was fixed at 2e-4 the first 100 epochs and linearly decayed to zero in the next 100 epochs, like [78].

2.2.2 - DualGAN

DualGAN [79] also solves the same task as CycleGAN, while using Wasserstein GANs [82]. DualGAN also uses a reconstruction loss, which is similar to CycleGAN's cycle-consistency loss. The generator architecture is a U-net [58], and the discriminator is a 70x70 PatchGAN [81]. The model was trained with the Adam optimizer for 200 epochs similar to the CycleGAN.

2.2.3 - GANILLA

GANILLA [80] is a variant architecture for the CycleGAN model designed to appropriately transfer the content to the stylized image. See [80] for generator architecture details. The discriminator is a 70x70 PatchGAN. The model was trained for 200 epochs in an identical manner as the CycleGAN.

2.2.4 - Color mapping tool

As a baseline, we used a color mapping tool using spectral unmixing algorithms, as previously described in [73].

2.2.5 - Tiled inference

We performed GAN model inference on overlapping tiles with stride 256. The generator was applied to each patch, yielding a 19x19 array of overlapping predicted H&E patches. A 5120x5120 generated H&E montage was then constructed, with each pixel intensity value in the montage being a weighted average of intensity values from the H&E patches which overlapped at the given pixel location. The pixel intensity values from each contributing patch were weighted proportionally to $exp(-d^2/2\sigma^2)$ where d is

the distance from the given pixel location to the center of the contributing patch. The weights in the weighted average were normalized to sum to 1. The parameter σ was set to 128 pixels.

2.2.6 - Quantitative evaluation of the models

An external critic model (70x70 PatchGAN with a fully connected layer) was trained to quantitatively evaluate how "real" the outputs of the various models look. We used accuracy and a binary cross-entropy loss from the critic as quantitative measures to compare the quality of the generative models. We trained a separate critic on the predictions for each model to keep results independent. Each critic were trained for 20 epochs with a 0.001 learning rate (one-cycle learning rate schedule). Each dataset consisted of "fake" H&E images generated from the test set and real H&E images from the train set. It was a balanced dataset with an 80/20 dataset split.

2.2.7 - Datasets and implementation

The H&E data came from a region in a single whole-slide image of human kidney with urothelial cell carcinoma. The MUSE data came from a single surface image of similar tissue. We obtained 512x512 tiles from the images, resulting in 344 H&E tiles and 136 MUSE tiles. The tiles were randomly cropped into 256x256 images when loaded into the model. Code was implemented with PyTorch 1.4.0 [83], and fastai [84].

2.3 - Results

2.3.1 - Training on unprocessed MUSE images

In Figure 2.1, results on the test dataset after training a CycleGAN on MUSE and H&E images are shown. With close inspection, it is evident that the generated H&E images do not appropriately transfer the content of the original MUSE image. Bright in-focus nuclei are converted to white spaces in the virtual H&E image (boxed in red). On the other hand, the darker regions are converted to nuclei in the H&E image (boxed in yellow). The overall trend that the CycleGAN followed was converting brighter regions to background white spaces, and darker regions to nuclei. We have observed that using color- and

intensity-inverted MUSE images greatly improves training and subsequent models were trained on inverted MUSE images.

2.3.2 - MUSE-to-H&E translation

We trained a CycleGAN, DualGAN, and GANILLA model on the MUSE and H&E image dataset (Section 2.2.7), and performed inference on the test dataset, which is a 5120x5120 image. Individual 512x512 tiles were inputted into the model.

In Figure 2.2, we can see that the CycleGAN and GANILLA models provided visually compelling results that appropriately transfer style and content. The model successfully converted MUSE representations of cancer cells, inflammatory cells, and connective tissue to the corresponding H&E representations. However, DualGANs performed poorly, with weak transfer of style, and many artifacts. Finally, CycleGAN and GANILLA performed better than the traditional color-mapping baseline.

2.3.3 - Inference

We have tested inference with a single 5120x5120 image. As the generators are fully convolutional networks, variable sizes are allowed for these models (though the scale must remain same). However, the full region cannot be inputted into the model due to memory constraints. While the models performed well on individual 512x512 patches, we observed (Figure 2.3) that the montage had artifacts near the edges of the individual patches (tiling artifacts), and the predictions are inconsistent in color and style between tiles.

In order to resolve these problems, we performed model inference on overlapping tiles with stride 256 as explained in Section 2.5. Figure 2.3 demonstrates how this blending approach suppressed the emergence of tiling artifacts. Figure 2.4 shows that the final generated montages were much more consistent in style and color throughout the montage.

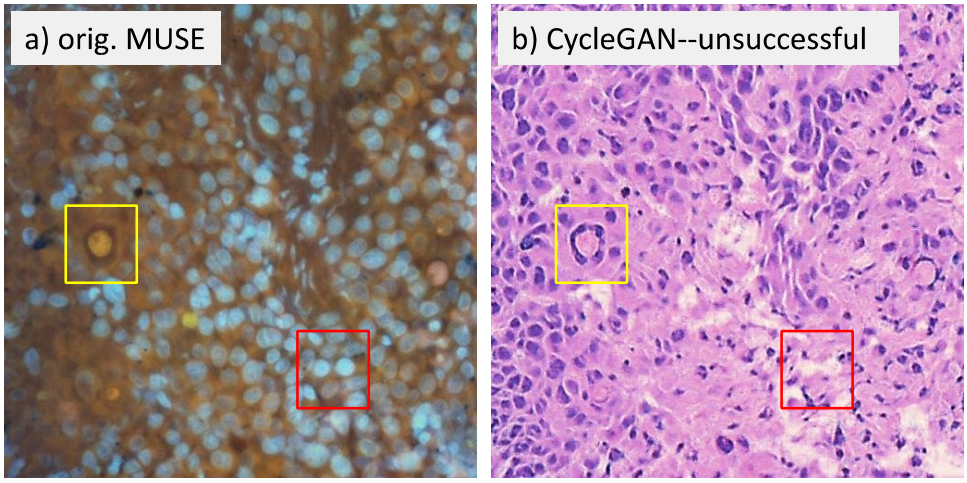

Figure 2.1. Training CycleGAN on unprocessed MUSE images.

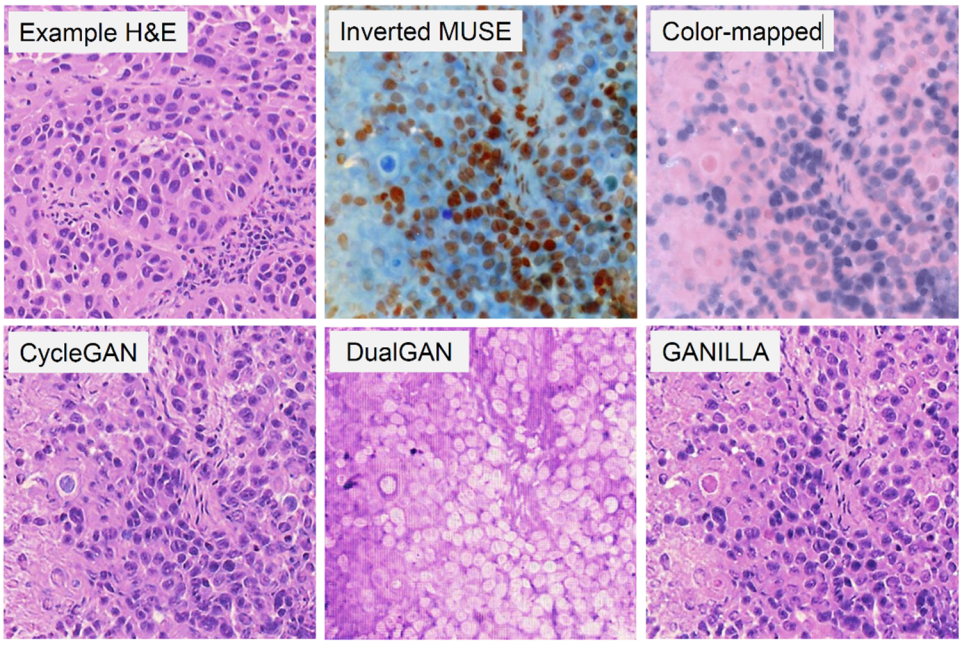

Figure 2.2. Comparison of MUSE-to-H&E translation models.

2.3.4 - Critic training

Using the H&E generated results of the CycleGAN, GANILLA and DualGAN models, we trained three separate external critics to objectively measure the quality of the generated images. A fourth critic was trained on images from the color mapping tool as a baseline comparison. In this experiment, we would expect the critic model to fail more often if the model outputs are higher quality, that is, resemble H&E images more closely.

Figure 2.5 shows the graphs of the validation loss and accuracy while Table 2.1 presents the accuracy from critic training. They show that the critic performed more poorly on CycleGAN and GANILLA images. The DualGAN was not able to fool the critic because of its poor performance in producing a convincing color conversion. Interestingly, DualGAN performed worse than the color mapper baseline. Overall, the critic had the hardest time identifying the CycleGAN model as "fake", which seems to suggest this model produced the most realistic images. These results support the conclusions from qualitative analysis in Section 2.3.2.

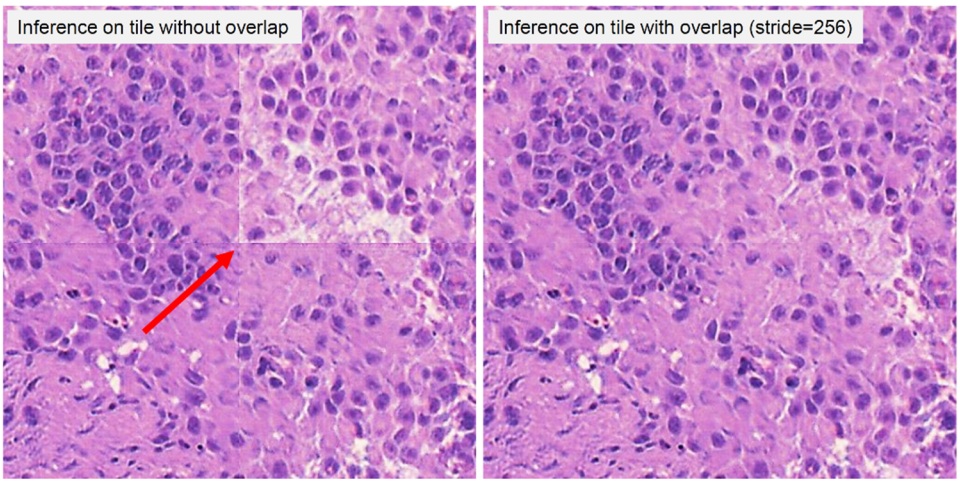

Figure 2.3. Demonstration of tiling artifacts

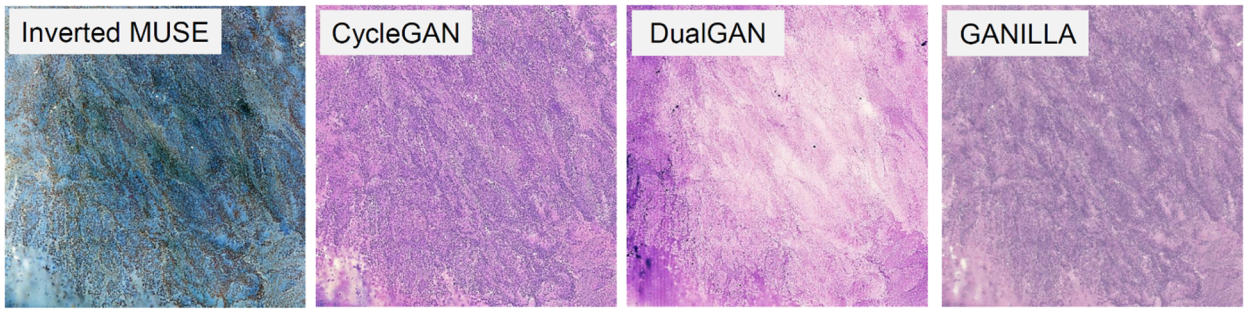

Figure 2.4. Montages generated from predictions on overlapping 512x512 tiles with stride 256.

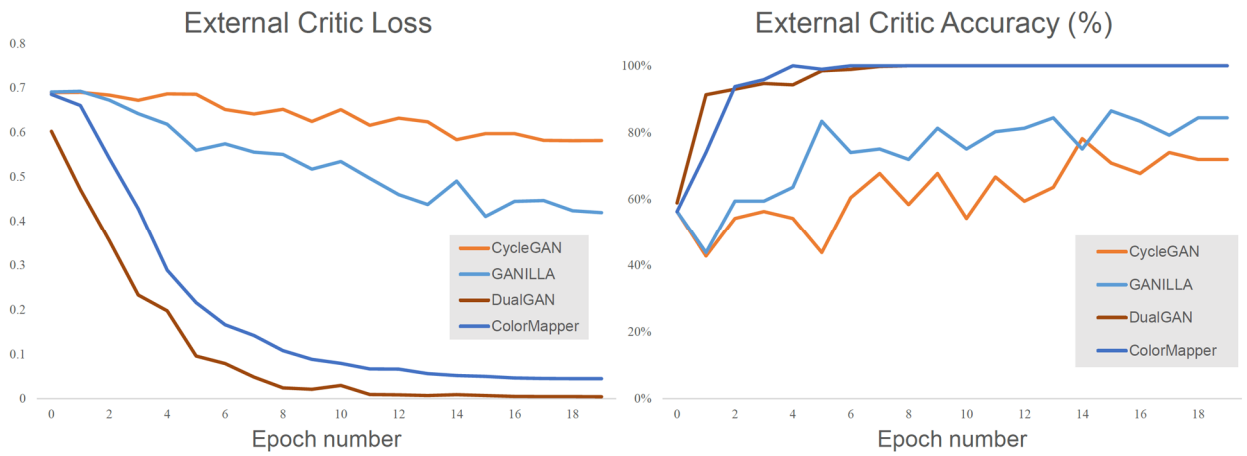

Figure 2.5. Quantitative evaluation of the models via real/fake H&E critic training

Table 2.1. Negative Critic Accuracy (%)

	Epoch #			
GAN Loss	1	5	10	20
CycleGAN	56.3	54.1	67.7	71.9
GANILLA	56.3	63.5	81.2	84.4
DualGAN	58.1	94.2	100	100
Color Mapper	56.3	100	100	100

2.4 - Discussion

In this study, MUSE modality conversion using unpaired image-to-image translation techniques was performed in order to generate virtual H&E images. We qualitatively observed that the GAN-based models studied here produce visually compelling results, with CycleGAN providing the best results.

For proper training and inference of the models tested here, inverting the MUSE images was required. This is likely because the CycleGAN cannot learn the association between brighter nuclei in MUSE to darker nuclei in H&E. It assumed all bright objects in MUSE must be background in H&E, while dark background objects in MUSE must be tissue in H&E. We found this content preservation problem especially prevalent in DualGANs. In future work, additional constraints, such as the saliency constraint introduced in [85], may be tested in order to directly convert unprocessed MUSE images to virtual H&E images.

A major challenge with training unpaired image-to-image translation models is the lack of quantitative metrics. Most approaches for quantifying model performance relied on crowdsourcing approaches (e.g. Amazon Mechanical Turk) to rate quality of the produced images. However, with difficult-to-interpret histological images, this is not an option. Most microscopy modality conversion studies [74]–[76] had paired data and therefore quantitatively evaluated via structural and perceptual similarity metrics like SSIM and PSNR [86]. However, there are some key structural differences between MUSE and H&E images. This would mean that visually compelling virtual H&E images that also preserve structural content may not have high perceptual similarity scores. Instead, we relied on an independently trained critic model to estimate image quality and perceptual similarity. While we found the results to be very consistent with our visual inspection, it is important to note that it is not a perfect metric and does not account for GAN "hallucinations" or preservation of content. The best metric is still visual inspection by human beings. Future work will quantitatively evaluate image-to-image translation models with pathologist ratings and interpretation.

Another key consideration during the development of these models is model inference. We expect users to be able to select regions of interest from a whole image to convert to virtual H&E almost instantly. Currently, this is still a challenge that needs to be addressed (CycleGAN on 5120x5120 with stride 512 took 12.7 s on NVIDIA TITAN RTX). Future work will analyze how model inference can be sped up while minimizing the trade-off regarding montage consistency.

2.5 Conclusion

In conclusion, we have tested three unpaired image-to-image translation models for MUSE-to-H&E conversion. We observed that color- and intensity-inversion is an essential preprocessing step when training with MUSE images. Additionally, we used a semi-quantitative method of evaluating the models and determined CycleGANs obtain the best results. We hope our framework can help improve the efficiency of the pathologist workflow by bridging the gap between MUSE and traditional histology.

3. Fluorescence imitating brightfield imaging (FIBI) for rapid slide-free histology

3.1 - Introduction

Light microscopy of tissue biopsies remains central to the diagnosis and management of solid tissue disorders, notably cancers but also other diseases. The brightfield (transmission) optical design of today's clinical microscopes, which reached near-contemporary performance as far back as the 18th century, requires optically thin (4-5 micron) slices of tissue mounted onto glass slides. These tissue sections, typically stained with hematoxylin and eosin (H&E) are usually prepared following formalin fixation and paraffin embedding (FFPE), a technique developed in the 19th century and not essentially changed in the interim. FFPE-based histology is a labor- and time-intensive process, on the order of several hours to overnight, or even much longer if the specimen is acquired at one site and the processing facility is located elsewhere. Moreover, FFPE and subsequent sectioning steps can consume most or all of small samples, after which there may be little, or nothing left for downstream analyses. This is an important consideration when molecular profiling tools such as immunohistochemistry, DNA/RNA expression or epigenetics studies, metabolomics, etc. are becoming standard-of-care for diagnostics and therapy guidance. Cryotomy (frozen sectioning) is an alternative to FFPE-based methods and can generate H&E-stained slides within 20-30 minutes. While often used for rapid interpretation or intraoperative surgical guidance, this technique is artifact-prone and demands considerable expertise. Furthermore, and as is the case with standard FFPE histology, it is destructive of tissue and can adversely affect the amount of sample available for downstream analyses.

Ideally, a tissue histology approach could generate interpretable cellular-scale images of specimens directly from the samples themselves, without requiring the intermediate step of preparation of thin sections mounted onto glass slides. A side-benefit of such an approach would be the fact that cellular histology features would be directly captured digitally, rather than, as is the case with contemporary

digital pathology methods, requiring a whole-slide scan after the slides themselves are first generated—which currently represents an extra, laborious, time-consuming and costly additional step.

Indeed, such alternative microscopy techniques are under development for pathology applications. These can directly acquire microscope-scale images from thick, fresh (or fixed) tissue specimens. Such approaches include structured illumination [87], conventional reflectance and fluorescence confocal microscopy [88], multi-photon microscopy [22], [23], photoacoustic approaches [89], among others [2]. While these other techniques have distinct advantages and disadvantages, typically they are optically more complex than standard histology microscopes, with commensurate costs that would exceed those of instruments conventionally deployed in pathology settings. MUSE (microscopy with UV surface excitation) is an alternative approach previously developed in our laboratory [73] that addressed many of these issues by providing a potentially lower-cost, less complicated solution for tissue imaging.

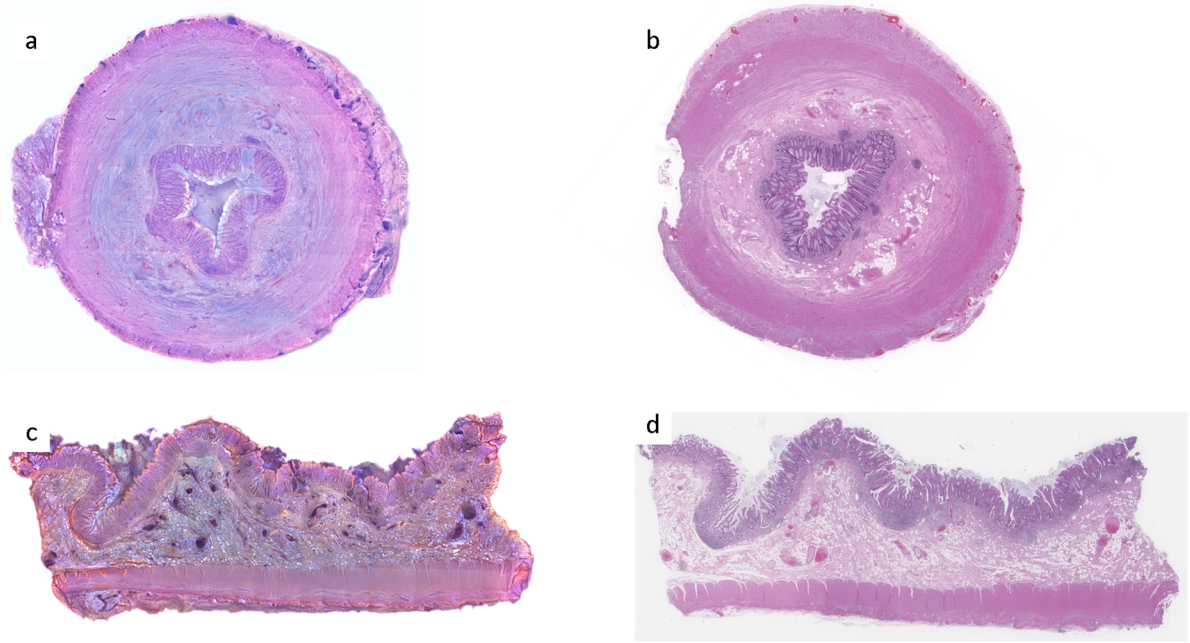

Figure 1. FIBI is an optically simple, cost-effective, rapid, non-destructive, slide-free microscopy technology. a) FIBI image of a thick, fixed, human appendix specimen. b) H&E whole slide image of the same human appendix specimen. c) FIBI image of a thick, fixed, human colon specimen. d) H&E whole slide image of the same human colon specimen.

We now present a novel method for slide-free imaging, fluorescence imitating brightfield imaging (FIBI), an optically simple, cost-effective, rapid, non-destructive, slide-free microscopy technology (Figure 3.1). It employs an epifluorescence-based optical light path to capture images of rapidly-stained, thick (unsectioned) specimens. A variety of stains can be employed, but most of the work presented here represents the use of hematoxylin and eosin, a combination that can generate images that not surprisingly, can closely resemble those from standard brightfield-based histology. The method depends on excitation of tissue autofluorescence, supplemented by eosin fluorescence, to generate a diffuse backlight arising mostly from below the surface of the specimen. A portion of this backlighting returns back through the surface of the specimen to be collected by a conventional microscope objective and transmitted to a standard color camera, as described more fully below. While similar in many respects, FIBI differs from MUSE in that FIBI images immediately resemble those encountered using standard brightfield rather than fluorescence-based microscopy. Moreover, MUSE needs UV-compatible viewing windows while FIBI can be used with regular glass and a standard through-the-objective epifluorescence optical path because FIBI operates in the visible spectrum. Bright, visible-range excitation LEDs allow exposure times as short as 5 ms per field, and thanks to the epi-illumination design, it is straightforward to deploy a variety of low- and high-magnification objectives. The short exposure times required allows for rapid XY scanning and also the acquisition of multiple Z-axis images that can be used to achieve extended depth of focus (EDOF) captures necessary to accommodate specimens with somewhat irregular (i.e., not completely flat) surfaces.

There are a number of important applications for FIBI (as well as other slide-free techniques). Current pathology practice can be extended with FIBI to deliver high-quality diagnosis or resection adequacy determinations in intraoperative settings for major surgical resection procedures, improving on technically challenging and sometimes inadequate frozen section-based methods. Other uses can include improved near-real time core needle biopsy evaluation as an alternative to cytology-based rapid on-site evaluation (ROSE) methods. Beyond that, it is possible that FIBI could be used for preclinical research in

pharmaceutical and biotechnology settings, for which standard histology procedures may be both money and time-sinks. The simplicity and affordability of FIBI also makes it suitable for deployment in global and low-resource and/or remote settings, with potentially great impact on health care.

A recent report described promising results from a validation study comparing FIBI to standard H&E slides across 100 specimens, using 4 pathology readers [34]. In addition, we previously described the potential utility of FIBI specifically for dermatology specimens [90].

Here, we provide a more detailed description of the staining and imaging methodologies, and along with technical underpinning of the optics and other image processing steps, including AI tools, and show results of FIBI imaging applied to diverse set of tissue specimens.

3.2 - Materials and Methods

3.2.1 - Typical processes for sample staining and positioning

In this study, a variety of specimen types were used, including fresh and formalin-fixed tissue, as well as material derived from FFPE tissue blocks. Anonymized excess tissue (obtained via IRB exemption) were obtained from the UC Davis Pathology Biorepository and included a number of common specimen types typically encountered in anatomic pathology. Specimens were usually medium-to-large sized (up to 2.0 cm^2 x 2.5 cm^2), and oriented and hand-cut with a razor blade if necessary to achieve a tissue surface as flat as possible but did include some specimens with dimensions typical of core needle biopsies.

The most common staining procedures involved the use of hematoxylin and eosin, although other stains and stain combinations have also shown promise. A typical procedure involves rinsing the surface of specimens with PBS (for fresh samples) or diH_2O (for fixed samples), prior to staining the surface of the tissue with 0.5 mg/ml Mayer's hematoxylin in diH_2O (H3136, MilliporeSigma) by either submerging the tissue into the hematoxylin solution or adding the hematoxylin dropwise to the surface of the specimen for 30 seconds. The tissue is then briefly rinsed in diH_2O and then stained with 0.25% eosin Y (E4382, MilliporeSigma) in 79% ethanol for 30 seconds following by another brief rinse with diH_2O.

After staining, each sample is placed in a custom-designed holder equipped with a front window opening that held a glass coverslip. A piece of white filter paper is situated behind each specimen to provide a light image background around the sample borders. A thin layer of foam is then placed behind the filter paper, and a back panel is screwed into place by hand to gently compress the sample against the flat imaging cover slip. The imaging holder was then positioned on an XYZ stage for immediate viewing. Time required for sample preparation, staining, positioning and placement onto the microscope can be as little as 3 minutes after receipt of the specimen.

A block-face-imaging variation allows for capture of histology views directly from the face of paraffin blocks—use case includes visualization of tissue still in the block in case it is important to verify the content or quality of the remaining specimen. Briefly, the face of a previously sectioned block is superficially deparaffinized with sequential application via pipette of xylene, followed by 100%, 70% and 50% ethanol. When wax is removed from about 100 microns of the block surface, the exposed tissue can be stained as above, and imaged via standard FIBI techniques.

After imaging, described below, the specimens can be submitted for standard FFPE processing (for long-term storage) with or without preparation of standard H&E-stained slides, if desired.

3.2.2 - Optical design and components

An exemplary instrument implementation is described here—other optomechanical components can be substituted. Epifluorescence excitation is generated by a 405nm LED (LZ1-00UB00-LED Engin), although other wavelengths are also usable, and is directed to the sample via a broadband dichroic (Di03-R405-t1-25x36, Semrock) and focused on the sample using a 10X objective (Nikon, Plan Apo, 0.3 NA). A long-pass emission filter (FF01-430/LP-25, Semrock) is present in front of the camera sensor to reject scattered and reflected excitation light when imaging in fluorescence mode. The tissue is positioned on a movable stage with a travel range of 25 mm by 50 mm, and a Z positioner is also included to provide automated focusing capabilities (Zaber Technologies X-LSM025B, X-LSM025A and XVSR20A). The camera used to capture the images shown here was a 9-megapixel scientific-grade CCD color camera

(Ximea, MD091CU-SY) accompanied by a 200mm tube lens (Thorlabs ILT 200). Overall gain and color balance (specific red, green, and blue channel gains) of the camera can be adjusted as desired for optimal visualization. The specimen is scanned field by field using the XYZ stage; the Z axis is used for manual focus and for implementing extended depth of field (EDOF) image capture via acquisition of multiple z-axis images [91]. This EDOF methodology involves synthesis of an in-focus image by selecting best focus regions from images taken at multiple depths. Compared to PSF-based approaches, the quality of the resulting image does not display computationally introduced noise. Moreover, the range that these extended depth of field approaches can cover is limited [92]. If multiple z-stacks are not required, imaging can be performed at about 1 cm^2/min—higher speeds are possible with upgraded components such as brighter LEDs, more rapid stages and cameras with faster capture and download performance.

3.2.3 - Image acquisition and pre-processing

Image acquisition, stage movement and focusing was performed using control software developed in the .NET environment. Individual frames were taken with exposures that usually ranged from 5 ms to 50 ms and saved in TIFF or JPEG format. Image processing was performed with open-source ImageJ software (http://imagej.nih.gov/ij/) along with open-source GNU Image Manipulation Program image processing software (https://www.gimp.org) and was in most cases confined to flat-fielding, adjusting the brightness and contrast, color balance and sharpening with an unsharp mask tool, along with occasional use of dehazing algorithms. A useful viewing tool was GIMP's auto white balance command, which automatically adjusts the colors by separately stretching the red, green and blue channels. While the results are quick and often represent a significant improvement in image appearance, the command can generate different results depending on the intensity distribution of the brightest and darkest pixels. More explicit manipulations can be used to standardize the display adjustments used across different fields. Such processing could include changes in brightness, contrast and gamma applied either to overall value (so color-neutral) or separately to individual color channels to achieve desired color balance. Unsharp

masking, another tool provided in GIMP, is used to improve sharpness, but has to be applied gently to avoid introduction of visible artifacts. Other tools were included in custom FIBI software, such as non-linear histogram matching, designed to generate color histograms in FIBI images that closely resembled the histograms seen in H&E images of similar specimens.

Either before or after image processing or AI-based conversion (see below), multiple fields of view are assembled into a montage by mosaicking either with ImageJ (using the Make Montage function after loading the multiple fields of view as an image sequence) or Microsoft Image Composite Editor (http://research.microsoft.com/en-us/um/redmond/projects/ice/) with 10% spatial overlap to perform subpixel registration and image stitching, or with Microvisioneer. Large image montages can be saved in pyramidal TIFF format compatible with third-party whole-slide imaging viewers, such as Aperio Slide Scan, Sedeen, QuPath [93], etc.

3.2.4 - AI-based color mapping from FIBI to virtual H&E

In addition to the traditional image processing steps described above, CNN-based tools were also applied to generate virtual H&E images. As it is not possible to obtain pixel-matched FIBI and H&E images of the same specimen—since the surface being imaged by FIBI will always be derived from a different surface or section of the specimen , it was necessary to deploy unpaired image-to-image translation algorithms [94]. Two typical examples, involving canine jejunum and human breast, of training and conversion was performed as follows. For the canine specimen, a total of 475 512 x 512-pixel patches were taken from a 10X FIBI image along with 600 512 x 512-pixel patches from the corresponding H&E whole slide image (WSI, originally acquired at 20X using an Aperio/Leica AT2 scanner). After adjustments to normalize pixel dimensions generated by these two different magnifications and capture systems, a CycleGAN model was trained and then applied to a separate 5120 x 5120-pixel patch (of which a small crop is shown in Figure 3.4) extracted from the same FIBI whole specimen image. For the human benign breast, 900 512 x 512-pixel patches were selected from a FIBI image of the whole

specimen, and 832 512 x 512-pixel patches from the corresponding H&E WSI for training. The trained CycleGAN was then applied to a separate 10,752 x 13,824-pixel patch (of which a small crop is shown in Figure 3.4) The two CycleGAN models were trained with the Adam optimizer for a total of 200 epochs. The learning rate remained at 3e-4 for the first 100 epochs before linearly decaying to zero for the second 100 epochs. In both cases, the inference was performed with overlapping patches as described in Abraham et al. [94] A custom code pipeline utilizing fastai [84] and PyTorch [83] was used for training and inference of the CycleGAN model.

3.2.5 - Effect of FIBI on downstream conventional histology and immunohistochemistry

In addition to examining downstream slide preparation on fixed tissues that have undergone FIBI imaging, a series of tests were performed on fresh specimens. Fresh tissue specimens underwent FIBI imaging before fixation, and subsequently were serial sectioned for H&E slide preparation and immunohistochemistry staining and fluorescent in-situ hybridization. For these analyses, two freshly resected kidney specimens, both afflicted with renal cell carcinomas, were obtained from the UC Davis Pathology Biorepository. The specimens were kept on ice upon retrieval and throughout the duration of the experiment. Samples that underwent FIBI staining were done using standard protocol described earlier with the exception of using 1x phosphate buffered saline (PBS) in place of deionized water for all rinsing steps. Control samples were removed from ice and left dry at room temperature while corresponding experimental specimens underwent the FIBI process. Upon conclusion of FIBI imaging, fresh specimens were placed in 10% neutral buffered formalin for overnight fixation, followed by placement in 70% ethanol for submission to the UC Davis Center for Genomic Pathology (CGPL). Each submitted specimen was sectioned and stained by the CGPL to yield one H&E slide, two slides for immunohistochemistry, two unstained slides and one section for fluorescent in-situ hybridization (FISH).

3.3 - Results

3.3.1 - Imaging and virtual sectioning

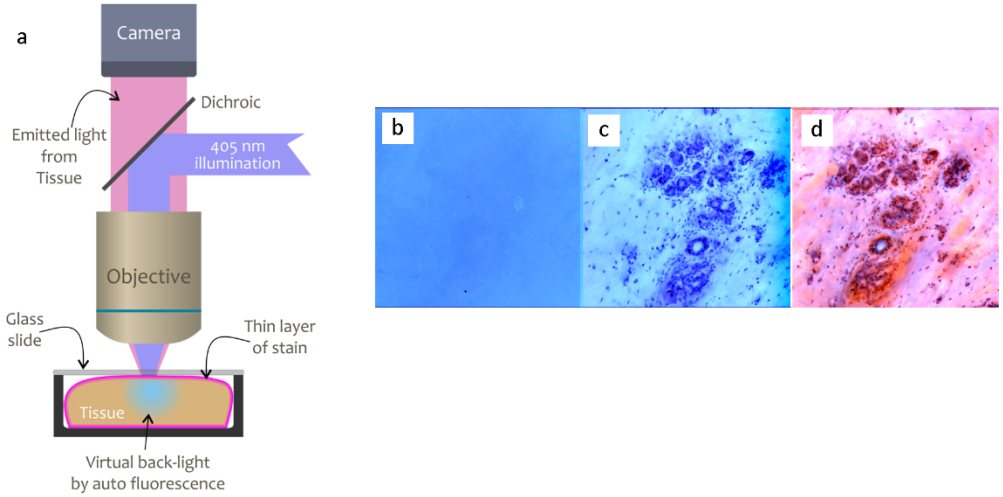

Figure 3.2. The imaging mechanism of FIBI. a) Optical setup for FIBI imaging. b) Image of human breast, no stain. c) The same region stained with hematoxylin. d) The same region is then subsequently stained with eosin.

FIBI relies on applying a thin layer of absorbing dyes to the surface of the tissue to limit the penetration of illumination light and imaging volume to the surface. This allows imaging the tissue using a very simple yet efficient and reliable approach by implementing standard epi-fluorescence illumination and imaging the fluorescence and absorption contrast to create the image.

Conveniently, stains extremely familiar to histopathologists, that is, hematoxylin and eosin, perform very well in this application. Hematoxylin is a strongly absorbing, and non-fluorescing dye that binds predominantly to nuclei, but depending on the formulation, will also stain other tissue elements to a lesser extent. It usefully signals the presence of RNA species in cytoplasm, a phenomenon that often reflects the presence of translationally active cells. Our initial experiments indicates that after 30s staining of human kidney with hematoxylin, it only penetrates 10 µm inside the tissue. Eosin penetrates deeper and it provides a nice complement, generating a pink tint to the overall tissue surface elements, just as it does in conventional slide-based histology. Figure 3.2a shows a schematic drawing of the setup. The illumination is based on epifluorescence and 405 nm illumination. The resulting images, after basic color

correction, closely resemble standard bright light transmission histology; the FIBI illumination light creates a backlight within the bulk specimen by inducing broad-spectrum autofluorescence. The autofluorescence is scattered under the surface of the tissue to create a "virtual backlight", illuminating the stained layer where it is collected by standard objective and transmitted to a standard color camera.

Figure 3.2b demonstrates an image of human kidney sample without any stain (autofluorescence), Figure 3.2c is the same region stained with hematoxylin and Figure 3.2d eosin added afterwards. Clearly, desired image contrast is not achieved until we apply the hematoxylin.

The thickness of the dyed tissue is also a crucial factor in the mechanism of FIBI. As shown in Figure 3.3a, a 5 μm-thick tissue slices (similar to that of a traditional H&E slide) demonstrates a fluorescence behavior. This is especially exemplified in the holes of the tissue which have no signal. If we increase the thickness of the imaged tissue, we observe a tissue backlight, as demonstrated by holes in the tissue that are now bright (Figure 3.3b). This backlight (generated by eosin fluorescence) leads to hematoxylin absorbance, providing a contrast similar to that seen in traditional H&E. We imaged tissues with different optical thicknesses ranging from 5 μm to 400 μm with the same FIBI optical setup and observed the transition from standard fluorescence with no backlight (black backgrounds) to standard FIBI imaging which occurs at around 100 μm (Supplementary Figure 3.1). Additionally, we note that utilizing an eosin backlight (by keeping a paper dipped in eosin behind the tissue during imaging), a fluorescence image of a 10 μm tissue section appears more similar to FIBI image of a hand-cut 400 μm specimen, with improved subcellular level of detail and clarity (Supplementary Figure 3.2).

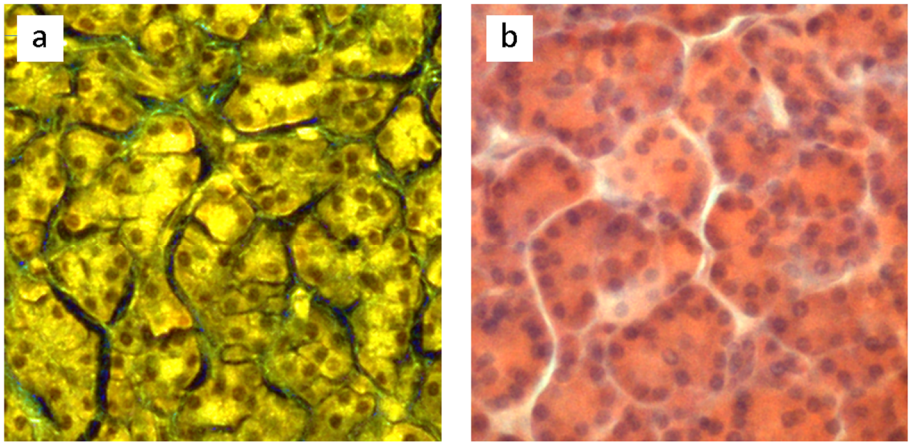

Figure 3.3 - The same specimen of pancreas was sectioned into different thicknesses and imaged with FIBI. a) A microtome was used to obtain a 5 µm thick specimen. b) Finally, hand cutting was used to obtain a 400 µm thick specimen.

3.3.2 - Conversion of FIBI images to virtual H&E appearance

In contrast to typical fluorescence-based methods, FIBI images start out exhibiting substantial resemblance to standard brightfield appearance—that is, the nuclei are dark compared to non-nuclear tissue components, and the background visible around the specimen or inside tissue holes is relatively bright; the raw images are usually quite viewable. That said, FIBI images can benefit from standard digital processing tools such as those available with photography-based methods as well as machine-learning tools to render results that are either easily interpretable or even indistinguishable from standard H&E.

MUSE, as a fluorescence-based technique, has a dark, signal-free background, whereas labeled tissue components such as nuclei fluoresce, generating essentially an opposite contrast compared to traditional brightfield microscopy. In contrast, FIBI images, more closely resemble conventional H&E-stained thin sections, allowing for a quick acclimation period. Nevertheless, since pathologists are (currently) most comfortable looking at bright-field, we demonstrate virtual H&E conversion for easier interpretation of FIBI images by pathologists.

There are several approaches for FIBI-to-H&E conversion (Figure 3.4). The current approach relies nonlinear histogram matching and provides images that are quite similar to traditional H&E (Figure 3.4c,d). However, we have recently utilized deep learning-based techniques that provide a superior imitation of H&E contrast.

This approached based on relatively recent AI tools using generative adversarial networks (GANs). An early version of GANs deployed for image mode conversion was developed by Isola et al. and termed pix2pix [81]. That name reflected the pixel-to-pixel matching between the source and target images required by the method. This approach is easily applied for virtually staining label-free slide microscopy or other imaging modalities where a ground truth H&E can be obtained. However, since the surface being imaged by FIBI will always be derived from a different surface or section of the specimen than the subsequently processed FFPE section for the H&E image, it was necessary to deploy unpaired image-to-image translation algorithms such as a CycleGAN [78].

A CycleGAN neural network was trained and applied to convert FIBI images into virtual H&E. On a modern graphics processing unit (GPU), conversions are near-real-time. As exemplified in Figure 3.4c, the conversion can generate images that are virtually indistinguishable from traditional H&E images (Figure 3.4d). When compared to nonlinear histogram matching (Figure 3.4b), which serves as a powerful baseline, we see that individual red blood cells and muscle nuclei are more apparent and well-defined. Note that this CycleGAN conversion approach can work for a variety of tissue types (Figure 3.5).

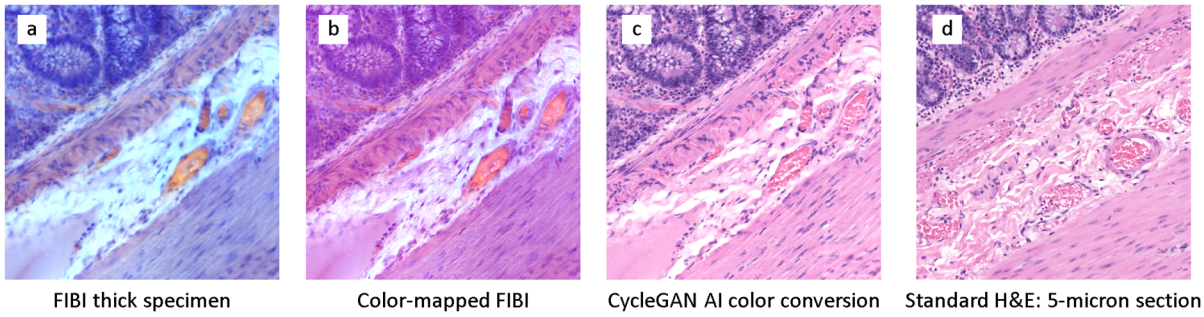

Figure 3.4. Color-mapping approaches for FIBI. For a FIBI image of dog jejunum (a) we demonstrate nonlinear histogram matching (b) and a CycleGAN (c) for FIBI-to-H&E conversion, with comparison to standard H&E (d).

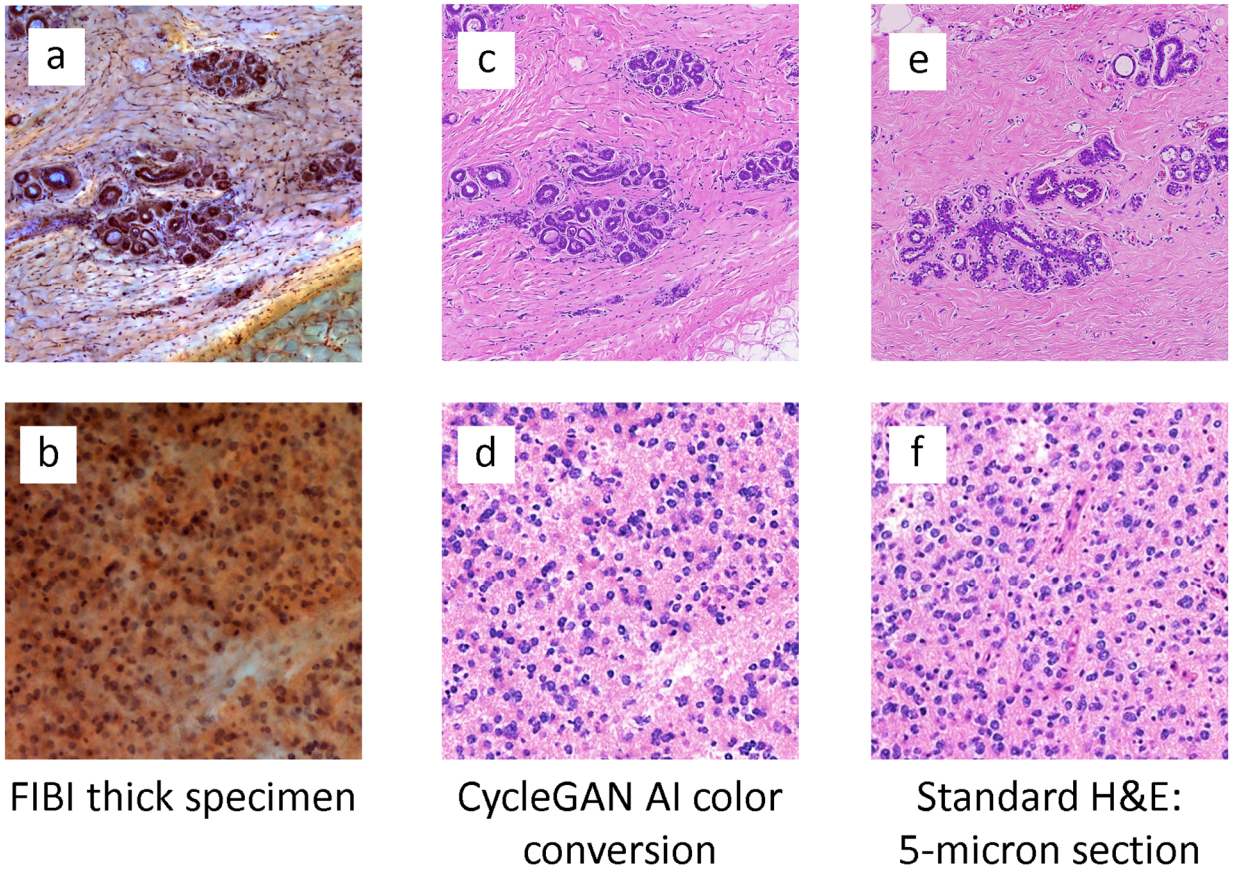

Figure 3.5: CycleGAN AI FIBI-to-H&E conversion can be applied to a variety of tissue specimens. a) FIBI image of a benign breast lobule near some adipose tissue. b) FIBI image of a glioblastoma. c-d) The corresponding virtual H&E conversion. e-f) Standard H&E for comparison.

3.3.3 - Image quality and resolution of FIBI

FIBI imaging provides subcellular resolution that allows details such as mitotic figures and chromatin textures to be appreciated at a level similar to standard FFPE H&E (Figure 3.6). It is worth noting that this is without CycleGAN conversion, and such subcellular details may become more apparent after virtual H&E conversion. Images shown here are usually acquired with a 10X objective with 0.3 and 0.45 NA, with the latter being comparable to H&E images obtained with a standard 20x objective. It is also possible to obtain improved resolution with FIBI utilizing a 20X magnification, but this comes at a cost of a smaller field of view and therefore lower imaging speed.

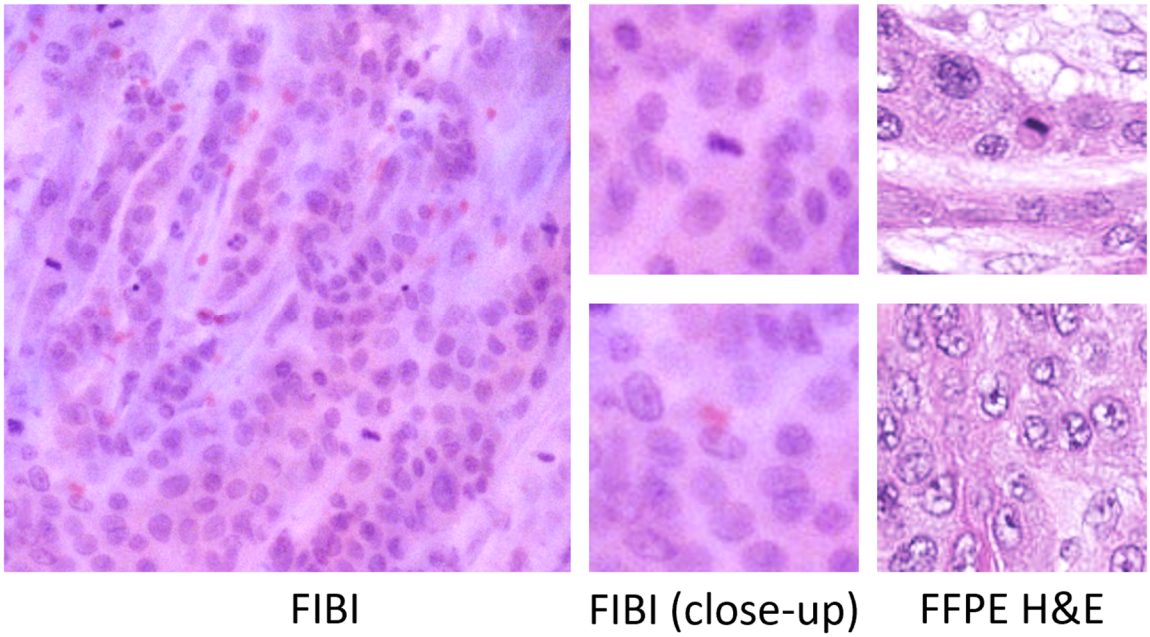

Figure 3.6 - Subcellular detail observed with FIBI imaging. Mitotic figures and chromatin texture can be observed.

3.3.4 - High-resolution extended field of view imaging

While individual fields of view have been imaged with FIBI and demonstrated here, it is also possible to image arbitrarily large specimens. However, there are a couple of challenges when imaging such large regions. For example, the surface of the specimen is not even throughout the entire region, leading to out-of-focus areas during imaging. Additionally, uneven staining throughout the specimen can leading to

significant variability in the intensity of the signal throughout the image. We collect images at multiple z-positions merge them into a single image that is in-focus throughout the entire image. Additionally, we utilize a simple intensity-leveling algorithm that results in a much more uniform image. With these enhancements, we obtain high quality multi-field FIBI and H&E stitched images, as shown in Figure 3.1.

3.3.5 - Block-face imaging

As a slide-free imaging technique, FIBI enables of fresh, unprocessed tissue specimens for rapid examination, but a technique for imaging paraffin blocks of tissue using FIBI has also been developed. Specifically, an FFPE block of tissue is superficially deparaffinized with xylene and ethanol, and the deparaffinized face of the block is stained with H&E and imaged with the optical system. These images are comparable in quality to FIBI imaging of fresh specimens (Figure 3.7).

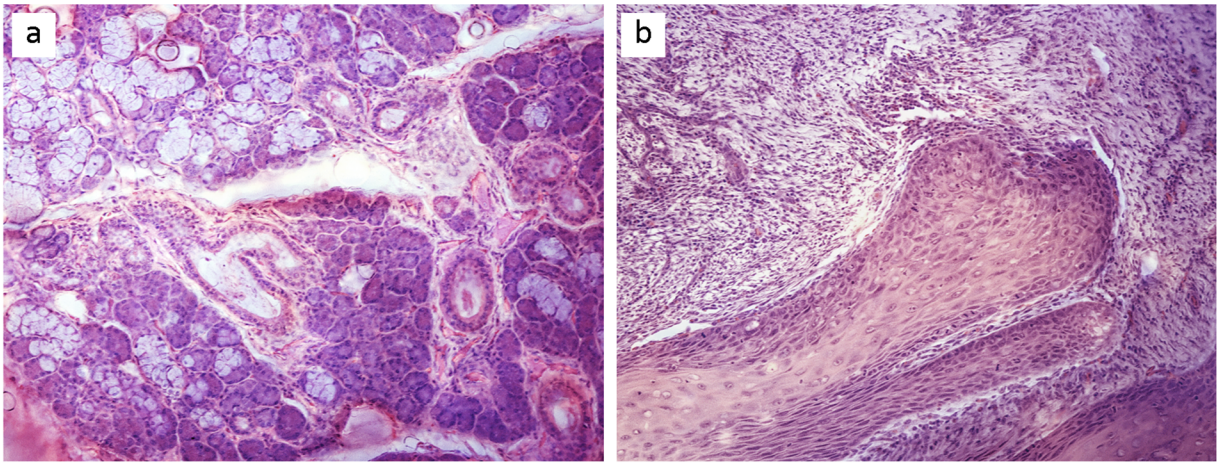

Figure 3.7. FIBI imaging of the superficially de-paraffinized surface of FFPE tissue blocks. a) FFPE tissue block of benign human submandibular gland biopsy. b) FFPE tissue block of squamous cell carcinoma in human oral cavity biopsy.

3.3.6 - Minimal impact on downstream slide preparation and molecular analysis

In most use-cases demonstrated here, FIBI imaging of a tissue specimen is followed by FFPE processing and H&E slide preparation, and the quality of the H&E slides are comparable to standard H&E slides.

Molecular characterization of tissue specimens has become essential for diagnoses and therapy guidance. Such analyses include protein and DNA profiling, RNA expression measurements, IHC, etc. It

is important that FIBI does not interfere with subsequent molecular analyses. Preliminary experiments suggest that prior FIBI does not affect subsequent IHC (Supplementary Figure 3.3). HER2 FISH interpretation indicated no discernible differences compared to tissue not imaged with FIBI, unless imaging time was significantly high (250 seconds of LED exposure per field of view). Further work will be performed to explore any possible effects of FIBI on subsequent molecular analyses.

3.3.7 - 2.5-dimensional surface profiling and novel contrasts

As a slide-free microscopy technique, FIBI often provides additional information or information that differs from traditional H&E (Figure 3.8). As it is a surface-weighted microscopy technique, the three-dimensional surface profile information is often apparent in images taken FIBI. Additionally, the 405-nm excitation leads to autofluorescence of tissue components that lead to different contrasts. For example, collagen is presented as a fluorescent white signal, often with more prominent morphological features. Finally, it is important to note that the use of fresh, thick specimens means that many common FFPE-derived artifacts are not observed with FIBI image.

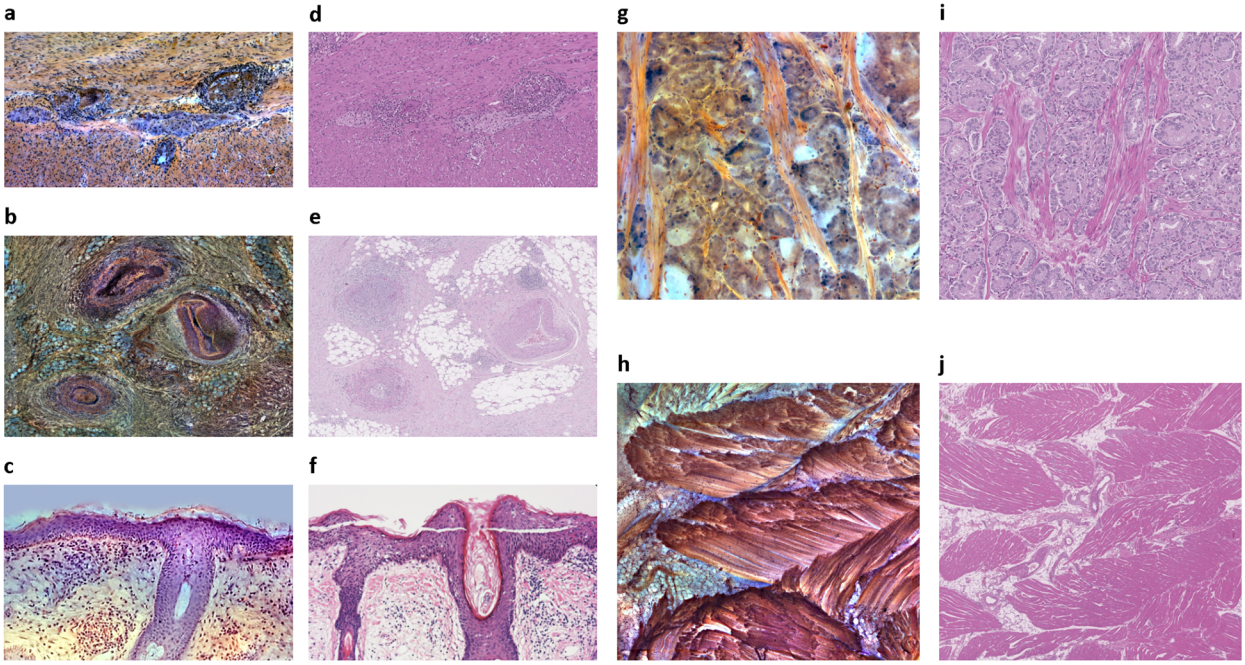

Figure 3.8 – Unique contrasts provided by FIBI. a) A ganglion within this large intestine is more apparent in dark blue in the FIBI image compared to its H&E (d). b) FIBI imaging of bladder biopsy (diagnosed with urothelial cell carcinoma). FIBI images show significant detail in blood vessels not usually present in H&E (e), such as a layer of elastin that is fluorescing. c) FIBI image of ear skin, and its corresponding H&E (f). g) Collagen fibers and surrounding cancer is quite delineated in this FIBI image of prostatic adenocarcinoma compared to its H&E (i). h) FIBI image of a benign tongue specimen. The three-dimensional directionality of the muscle fibers can be appreciated here, and not easily perceived in the 5 µm H&E slice (j).

3.4 - Discussion

Conventional histopathology has been the gold standard for cancer diagnosis since the foundational work of Rudolf Virchow (c. 1855). Not much has changed: formalin-fixation and paraffin-embedding (FFPE) tissue processing with microtome sectioning and staining have proven to be the most practical and logistically feasible method for handling, preserving, and evaluating tumors. However, as a process that takes hours or even days, it postpones diagnoses and contributes to overall health system inefficiencies and substantial, avoidable patient anxiety. Additionally, because of fixative-, heat- and solvent- induced nucleic acid fragmentation and degradation, FFPE-based processing is sub-optimal for downstream molecular assays.

In this study, we demonstrate that by exploiting both the fluorescent and absorptive properties of specific stains (hematoxylin and eosin studied here), we can observe surface weighting that allows for high-resolution imaging of specimens. The overall tissue microarchitecture can be observed, but also subcellular features like nuclear chromatin texture and mitotic figures.

In contrast to the standard histopathology workflow, which can take several hours and requires highly-skilled technicians, the FIBI workflow instead takes just a few minutes from specimen to image for pathologist review. Specifically, it involves tissue orientation and possible surface preparation via manual cutting using a sharp blade, staining the tissue for 30 s, (rinsing for 20 s), placement into the cassette, and imaging directly with a simple epifluorescence microscope with 405-nm excitation and a standard color camera to acquire the FIBI image. While we use hematoxylin and eosin for staining tissue in FIBI imaging, the methodology is not limited to those stains. Other stain combinations will be further investigated in subsequent work. The standard clinical pathology workflow is minimally affected for two reasons: (1) the H&E staining used by FIBI is also used for standard histology, (2) FIBI can non-destructively image specimens from any stage of the standard clinical pathology workflow, including fresh, fixed, and paraffin-embedded specimens.

A preliminary validation study was conducted to evaluate the diagnostic suitability of FIBI images [34]. In this study, pathologist diagnoses determined from histogram-matched FIBI images and diagnoses determined from corresponding H&E images were compared. The study set was comprised of 100 surgical pathology specimens imaged with FIBI and subsequently processed, H&E-stained, and digitally imaged. The digital FIBI and H&E images were reviewed by 4 board-certified pathologists. Aggregated over all readers, the diagnoses made with FIBI reads and H&E reads were essentially identical (no major discordance) 98.2% of the time (393 reads). These results indicate FIBI's potential as a tool for primary pathology diagnosis. For widespread clinical adoption, FIBI will require detailed, multi-tissue, multi-pathology, multi-center validation.

As a slide-free microscopy technology that relies on surface weighting, FIBI is quite similar to MUSE [73]. There are two underlying mechanisms that enable MUSE: 1) UV light around 280 nm penetrates thick tissue specimens to a depth of no more than about 10 microns; and 2) such UV light can induce emissions, in the visible range, from a large variety of inexpensive fluorescent stains that can mimic the tissue specificity of H&E. With color conversion algorithms, the resulting fluorescent images can be processed to resemble those seen with conventional brightfield H&E histology. However, MUSE employs relatively short wavelength UV excitation which introduces several challenges and concerns. Since standard glass microscope lenses are opaque in that spectral range, MUSE uses obliquely angled illumination that bypasses the objective. This general configuration makes it difficult to use high-NA, high-magnification lenses with typical short working distances, as it is difficult to get such objectives close enough to the tissue without physically blocking excitation. This also requires the sample support or viewing window to be composed of quartz or sapphire, rather than less expensive glass. In addition, UV excitation intensities that can be generated using the comparatively low-power LEDs currently available result in exposure times in the 100's of milliseconds per image, which can lengthen scan times for larger specimens.

In contrast, FIBI uses convenient LED sources in the visible range that are both brighter and cheaper which results in faster imaging. Multiple excitation wavelengths can also be deployed with FIBI and provide additional spectral contrast. As noted above, it is not necessary to include potentially expensive UV-transparent viewing windows or sample stages, which will be helpful when large-sample-format (15 x 15 cm or larger) FIBI instruments are implemented, or alternatively, disposable imaging cassettes are deployed.

As with MUSE, there are some differences between the contrasts of FIBI and that of traditional histology. We highlighted several examples where FIBI provides additional contrast not typically seen in H&E. This includes improved contrast of collagen and elastin, fluorescence of Paneth cells. Additionally, as an imaging technique that relies on surface weighting, the topography of the tissue is visualized in a

2.5D manner. We hope that the additional contrast can be useful both for scientific discovery and research and for novel diagnostic use-cases. Additionally, the additional contrast may be beneficial for machine learning algorithms to extract more meaningful information from the images.

FIBI can also be used for evaluating the quality of biopsies, intraoperative surgical guidance (as an alternative to frozen sections), Point-of-care histology for dermatology, histology in low-resource settings, and veterinary applications.

Tissues – either fresh or fixed – can be stained and imaged with FIBI within a few minutes, which is significantly faster than the hours or days associated with FFPE-based histopathology. Computational algorithms (including deep learning-based techniques) can be used to convert FIBI microscopy images to mimic traditional H&E-stained brightfield microscopy images. Finally, FIBI is non-destructive, which means biopsy specimens can be imaged and submitted for downstream molecular analyses, which is especially important in this next-generation era of molecular pathology.

3.5 - Supplementary Information

3.5.1 - Supplementary Figures

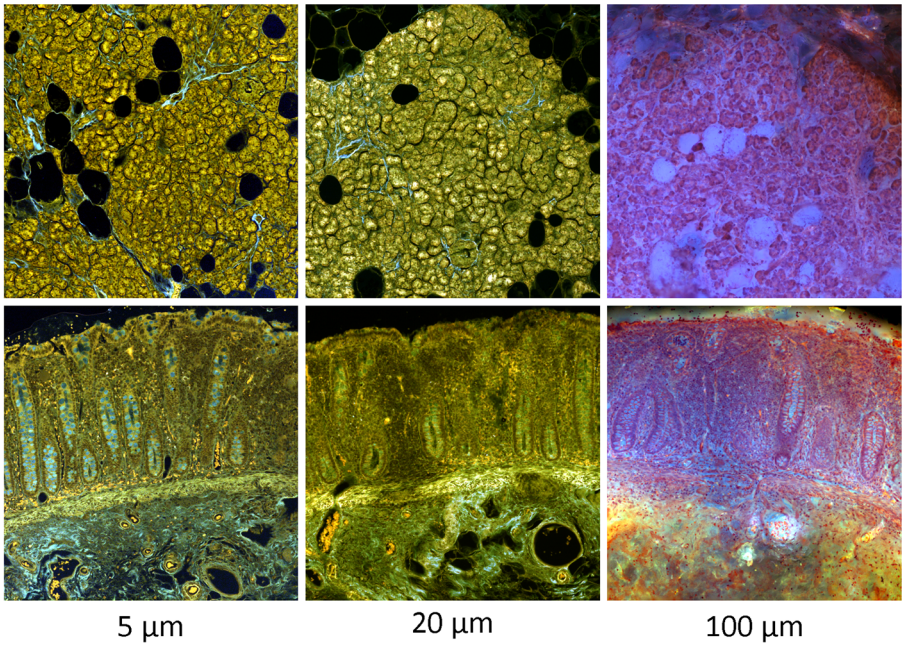

Supplementary Figure 3.1 - The effect of tissue thickness on FIBI imaging. Shown are two different specimens cut at different thicknesses (with either a vibratome or microtome) and imaged with the FIBI optical setup. The top specimen corresponds to benign rectum, and the bottom corresponds to pancreas.

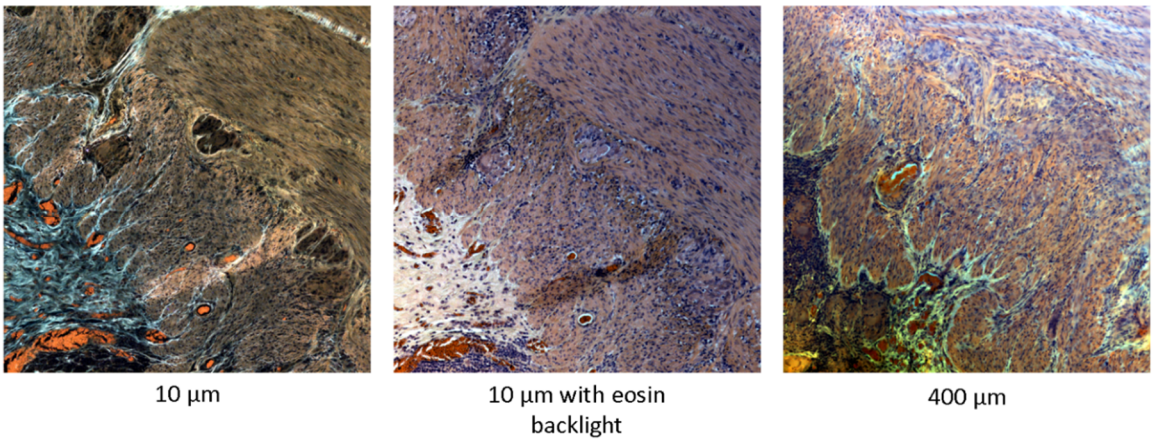

Supplementary Figure 3.2 – The effect of eosin backlight on FIBI imaging. Shown are different images of rectum tissue taken at 10 micron thickness, 10 micron with eosin backlight, and 400 micron thickness.

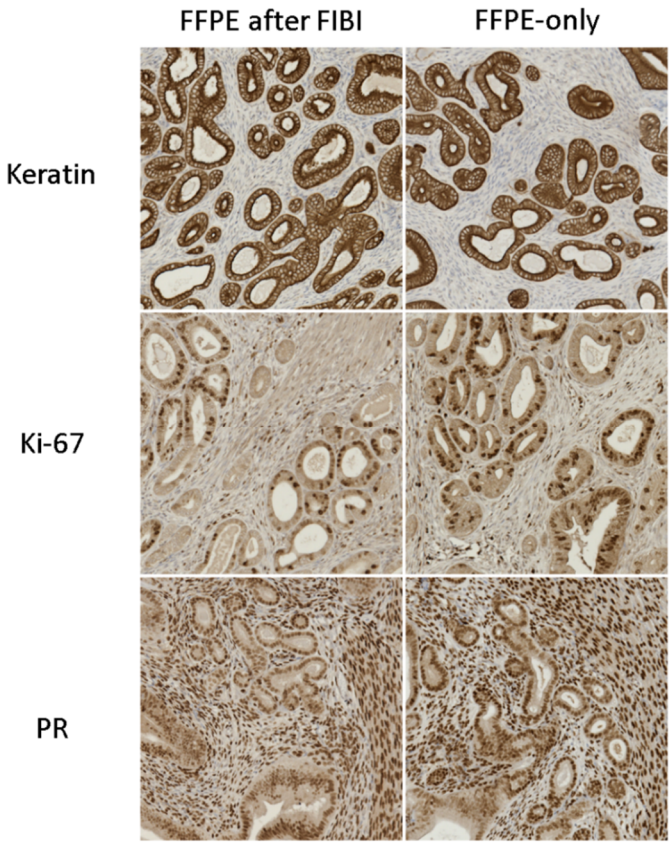

Supplementary Figure 3.3 – Prior FIBI imaging does not affect immunohistochemistry. Breast tissue was imaged with FIBI and IHC was performed afterwards. Three IHC markers were evaluated: keratin, Ki-67, and progesterone receptor (PR). There is no discernible difference in IHC quality compared to the control (right column).

4. Pilot study of FIBI (Fluorescence Imitating Brightfield Imaging) for rapid, slide-free dermatopathology

4.1 - Background

Conventional histopathologic examination involves tissue fixation with formalin and paraffin or rapid freezing, followed by thin sectioning, staining, and examination on slides using a brightfield microscope. This process requires expensive laboratory equipment and trained personnel. Novel techniques for slide-free or *ex-vivo* microscopy aim to avoid sectioning and extensive processing [11], [95]. Advantages include greatly reduced time to image, lower requirements for tissue processing, and the inherently digital nature of images that can be rapidly interpreted either on site or remotely. This digital information also lends itself well to machine learning. Current slide-free techniques include multiphoton confocal imaging [96], full-field optical coherence tomography [97], [98], light sheet microscopy [99], stimulated Raman spectroscopy [100], [101], and microscopy using ultraviolet surface excitation (MUSE) [30], [31]. However, these technologies are expensive and require complex instrumentation, which has precluded widespread adoption of slide-free microscopy in pathology. In contrast, we present a novel slide-free microscopy technique that is inexpensive and relies on simple optical instrumentation [102]. Fluorescence Imitating Brightfield Imaging (FIBI) uses standard microscope optics and a color camera to detect signals from tissue specimens stained with standard hematoxylin and eosin (H&E). Even though an epifluorescence light path is used, the resulting FIBI images already resemble traditional H&E-stained slides imaged via brightfield; and deep learning mode-matching can be used to further increase the resemblance. Our study compares FIBI microscopy with conventional H&E for dermatopathology specimens.

4.2 - Methods

FIBI is based on standard traditional epi-fluorescence microscopy equipped with a 405-nm LED for excitation, a 10X microscope objective, a long-pass emission filter and a color camera (Figure 4.1). Alternatively, imaging can be done with a 20X microscope objective with 0.75NA. FIBI exploits eosin fluorescence and tissue autofluorescence to provide a virtual backlight within a thick specimen that is

remitted to the collection lens. The stained, non-sectioned surface of the tissue absorbs the remitted light to generate histologic contrast similar to that of a conventional H&E slide. The microscope is equipped with an XY stage for positioning and visualization of larger areas of the tissue. In this study, we simulate typical FIBI by imaging the face of paraffin blocks containing skin tissue already used for diagnosis for a wider range of pathologies. While the actual use case would be to image fresh or fixed specimens, such tissues are not easily obtained from actual patient material prior to submission for standard histology processing.

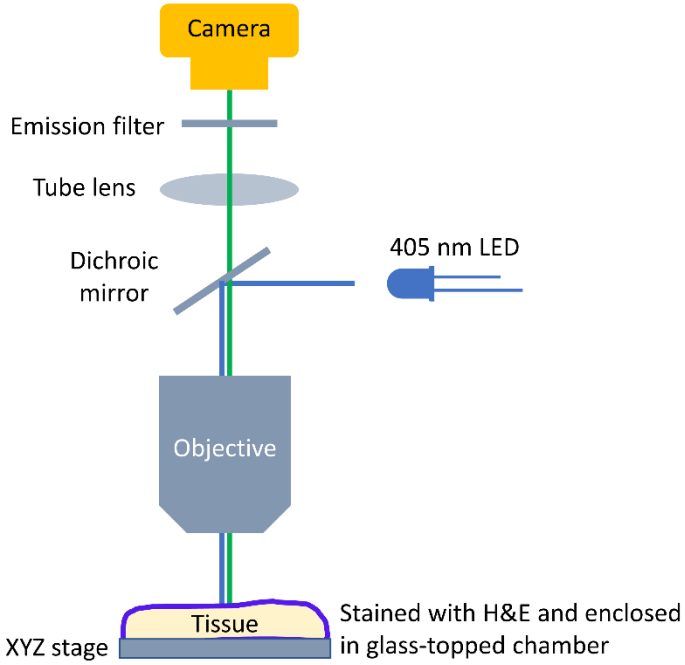

Figure 4.1 – A labeled diagram of the Fluorescence Imitating Brightfield Imaging (FIBI) setup: A light-emitting diode (LED) emits 405-nm blue light which excites the hematoxylin and eosin (H&E)-stained tissue to generate visible emissions that is collected by a 10× objective, focused through the tube lens, passed through the emission filter, and collected by a 9 MP camera.

The surfaces of paraffinized samples from the tissue bank (Institutional Review Board-exempt 743439-2) were deparaffinized using xylene and ethanol washes, then stained with hematoxylin and eosin. Eight initial cases selected by dermatopathologist M.A.F were used to refine the deparaffinization, imaging, and color conversion techniques. Cases were selected as common examples encountered in

routine practice, identified at the time they were encountered. This “convenience sampling” method was used for eleven cases intended for evaluation. Two were excluded based on difficulties with color conversion model training from small fields of view available. For comparison to FIBI images, standard hematoxylin and eosin slides were prepared from the blocks prior to surface deparaffinization and were scanned using a slide scanner (Aperio AT2, Leica Biosystems Imaging, Inc., Vista, California). Specimens were re-paraffinized and returned to storage.

The FIBI images were preprocessed before viewing by dermatopathologists. In order to have the same brightness and color density among all images, the color histograms of the FIBI images were adjusted using an open-source image editing program (GNU Image Manipulation Program [GIMP]). Additionally, the images were gamma-adjusted in GIMP to improve the appearance of otherwise too light or dark regions. To improve visual similarity to traditional H&E coloration for ease of interpretation, we developed a deep-learning CycleGAN mode-mapping model, similar to the MUSE-to-H&E conversion described in Abraham et al. [94] For each case presented, multiple specimens were obtained and imaged with FIBI. One of the images is designated as the “test set”, while the other images are used as a “training set” for training the CycleGAN to perform color mapping. Each image was divided into 512 x 512-pixel patches, and the distribution of tissue components (e.g., epidermis, stroma) was kept approximately balanced in the training set. For example, for the case-5 training set (squamous cell carcinoma), most patches of a large keratin pearl were removed so as not to overwhelm the training process and introduce incorrect biases. For the test set, the model is applied to overlapping patches stitched into a full montage as described in Abraham et al. [94] Unless otherwise described, the presented FIBI images were color-mapped using this CycleGAN model.

In total, nine FIBI images were selected for dermatopathologist review along with nine corresponding H&E images for comparison. Concordance between FIBI and H&E images was independently evaluated by two board-certified dermatopathologists (M.A.F. and M.K.). Ten selected epidermal and dermal structures (stratum corneum, stratum granulosum, stratum spinosum, stratum

basale, nerve, vasculature, collagen, sweat glands, adipose tissue and inflammatory cells) were assessed on each pair of images by the examiners. Each FIBI image was scored from 0 to 2 per structural element based on the scoring system in Table 4.1.

Table 4.1: Scoring system for FIBI comparison images

Score:
0: FIBI cannot identify the structure without correlating with standard H&E slides
1: FIBI can identify the structure without the need of standard H&E slides
2: FIBI can identify the structure with more certainty than standard H&E slides
N/A: Not applicable (the structure is not in the field to evaluate)

4.3 - Results

FIBI staining and imaging of paraffin-embedded specimens required approximately five minutes and did not adversely affect the specimens. Seventeen paraffin block-face FIBI images taken from nine cases were carefully compared to their standard H&E slide counterparts; diagnoses are provided in Table 4.2. A simple deep-learning-based color conversion step using the CycleGAN method generated re-colored FIBI images that were similar to traditional H&E (Figure 4.2). These color-converted FIBI and traditional H&E images were evaluated for identification of typical skin structures and diagnostic information. Mean scores from two board-certified dermatopathologists are reported in Table 4.3. In all specimens where present, FIBI images were equivalent to H&E slides for identifying epidermal layers, collagen, sweat glands, nerve tissue, and the presence of inflammatory cells (Figure 4.3). In the two melanocytic lesions evaluated, melanin and dermal melanocytes were evident with FIBI. While the dermatopathologist reviewers were able to identify inflammation and the presence of inflammatory cells, they described some difficulties in distinguishing between inflammatory cell subtypes such as eosinophils versus neutrophils in the 10X color-converted FIBI images. However, the subtypes are more distinguishable in 20X FIBI

images (Figure 4.4), indicating some limitations with the color conversion of 10X FIBI images. The majority of images from FIBI could be used to independently identify vasculature (Figure 4.5). Structural components like elastin are particularly prominent due to the extra contrast provided by the fluorescence excitation in FIBI. We observed that slide-free FIBI imaging avoided common artifacts that can affect quality using standard formalin-fixed paraffin-embedded processing, such as folding and tissue trauma (Figure 4.6).

Table 4.2: Diagnoses for the nine cases examined.

Specimen	Diagnosis
1	Targetoid hemosiderotic lymphovascular malformation
2	Basal cell carcinoma, nodular pattern
3	Squamous cell carcinoma, keratoacanthoma type
4	Infundibular follicular cyst
5	Squamous cell carcinoma
6	Lentiginous compound melanocytic nevus
7	Arthropod bite reaction
8	Arthropod bite reaction
9	Intradermal melanocytic nevus

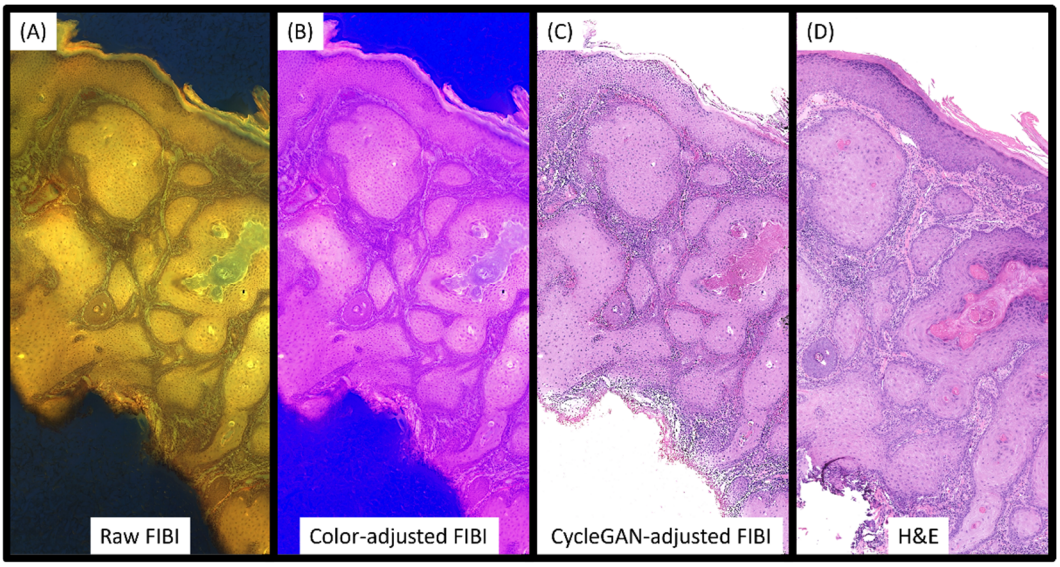

Figure 4.2 – A paraffin-embedded specimen of squamous cell carcinoma (keratoacanthoma type) imaged with FIBI and color-mapped to H&E with deep learning. The quality of the raw FIBI image (A) is improved to generate the adjusted FIBI image (B). This adjusted FIBI image is then passed into a deep learning-based FIBI-to-H&E color mapping tool to generate a version of the FIBI image with H&E contrast (C) that is virtually indistinguishable from a true, correlated H&E image (D). (FIBI - original 10× magnification, H&E – original 20× magnification)

Table 4.3: Scores for FIBI comparison images

Skin structure	**Mean Score** (N = 17)
Stratum corneum	0.96
Stratum granulosum	1
Stratum spinosum	1
Stratum basale	1
Vasculature	0.86
Collagen	1
Sweat glands	1
Nerve	1
Inflammatory cells	1

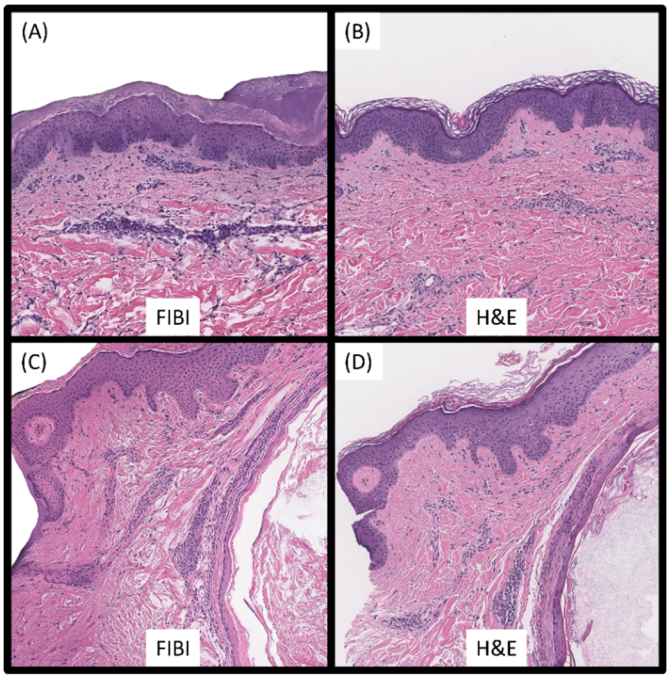

Figure 4.3 – Deparaffinized block face images from FIBI (A), (C), color-converted with CycleGAN with corresponding traditional H&E glass slides (B), (D) depicting epidermal cells and structures. The top images (A), (B) are taken of a specimen diagnosed with targetoid hemosiderotic lymphovascular malformation. The bottom images (C), (D) are taken of a specimen diagnosed with infundibular follicular cyst. (FIBI - 10× magnification, H&E - 20× magnification)

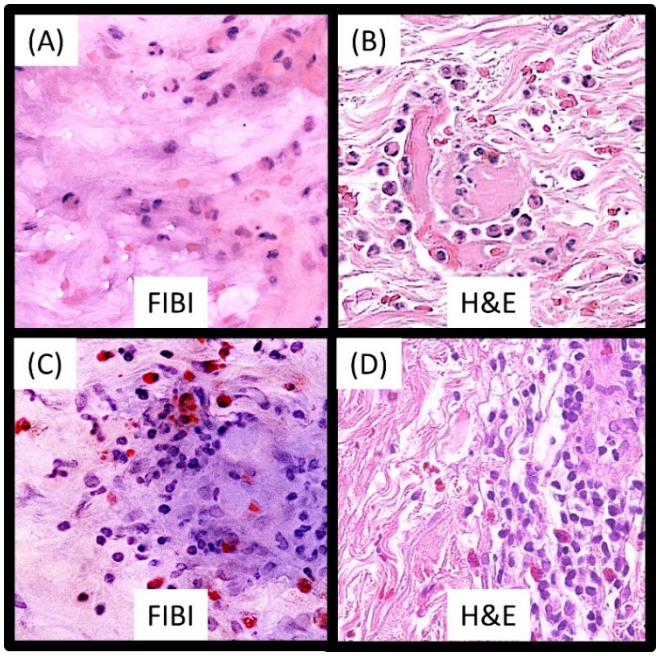

Figure 4.4 – Close-up examples of inflammatory cells in FIBI (left) and H&E (right) images. Shown here are prominent examples of neutrophils (A), (B) along with eosinophils and scattered lymphocytes (C), (D). Images were taken from a specimen with an arthropod bite. FIBI images were not converted with CycleGAN, but rather manually color adjusted. (FIBI - 20× magnification, H&E - 20× magnification)

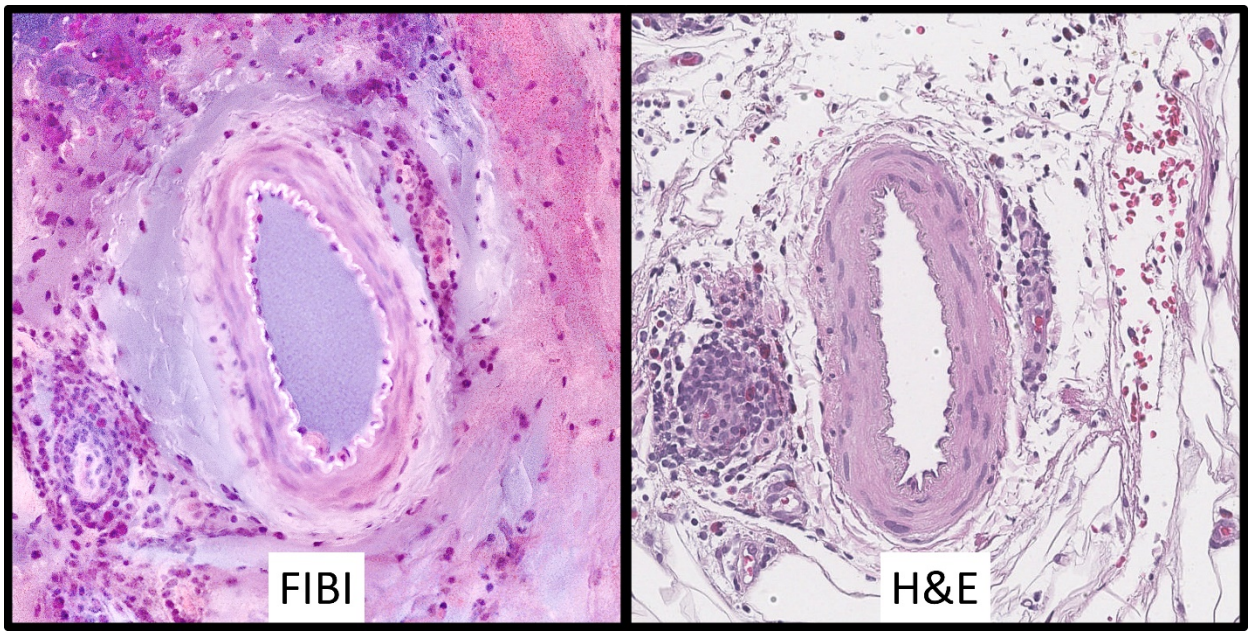

Figure 4.5 – Close-up example of a blood vessel in raw FIBI and H&E images taken from a specimen exhibiting an arthropod bite. The elastin of the internal elastic lamina is particularly prominent. FIBI images were not converted with CycleGAN, but rather manually color adjusted. (FIBI - 20× magnification, H&E - 20× magnification)

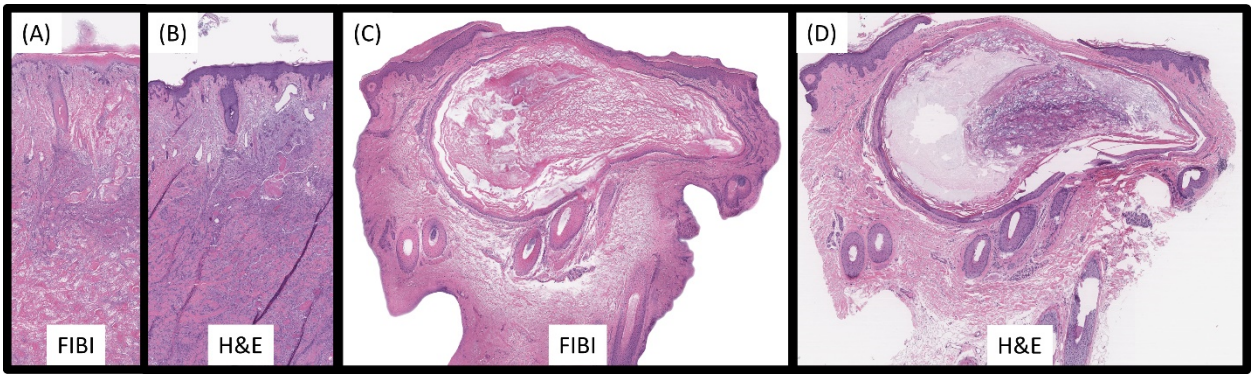

Figure 4.6 – Common sectioning artifacts in H&E-stained glass slides (right; folding, tissue trauma) avoided in tissue surface FIBI images (left). Shown here are cases of squamous cell carcinoma (A), (B) and infundibular cyst (C), (D). (FIBI - 10× magnification, H&E - 20× magnification)

4.4 - Discussion

In this study, FIBI images of cutaneous tissue specimens were comparable to their traditional H&E slide counterparts. Epidermal structures, inflammatory cells (however not always down to the subtype), and collagen were identifiable with FIBI image alone and other structures such as vasculature benefited from correlation with standard H&E slides. While these results are promising, evaluation on a greater number of cases for varied applications is needed to fully assess the suitability of FIBI as a potential alternative to conventional histology.

The ease of image capture with FIBI and the digitized nature of images are major advantages, especially in the expanding world of telepathology and machine learning [103]. FIBI uses widely available, familiar dyes (H&E), which contributes to its utility. With machine learning, real-time conversion of raw FIBI images to closely resemble authentic H&E coloration is possible. In addition, image acquisition is non-destructive, so specimens can be sectioned, re-dyed, or submitted for downstream immunohistochemistry or molecular studies. Tissue-face imaging also avoids common sectioning artifacts (Figure 4.2) such as creasing, separation of tissue components, and fat bleaching [104]. These artifacts can interfere with machine learning training as well [105]. Not thinly sectioning specimens may limit visualization of clandestine pathologies beneath the imaged surface, but specimens can be grossly sliced for additional evaluation and submitted for paraffinization or freezing after FIBI evaluation.

The FIBI microscopy device is portable and uses inexpensive components. This could expand access to histologic examination in areas with lower laboratory resources. The rapid tissue surface preparation and image capture (approximately five minutes) also lends itself well to time-sensitive procedures such as STAT sections or Mohs micrographic surgery.

A limitation of this study is that the standard H&E slides used for comparison are one section ahead of the block face captured by FIBI, thus not precisely spatially matched. This minimally restricted

direct correlation of images for dermatopathologist review. Consequently, we scored nine of eleven specimens on direct comparison. Also, the deep-learning-based models for H&E color conversion are still in the development stages and can generate local errors in the re-coloration step. This was especially evident for inflammatory cells and vasculature. However, such structures were distinguishable in 20X FIBI images, without CycleGAN color conversion, since those models were developed with 10X FIBI images. More training data, especially for 20X images, is necessary to overcome the limitations of the color conversion. As these models continue to train, their accuracy is expected to improve. As for the lower score in vasculature identification, in the six images where FIBI required referencing to standard H&E images, vessels mostly lacked the negative luminal white space seen in typical slides. This makes sense, as we are viewing the intact vessel lumen with FIBI but may benefit from better color conversion to negative space for ease of interpretation. Lastly, having only two dermatopathologist evaluators limits conclusions based on image scores. Nonetheless, this is a proof-of-concept study and depicts FIBI as a reasonable future alternative to standard histology processing, with benefits over traditional glass slides.

All specimens were paraffin-embedded, and the face of the block was de-paraffinized and imaged. This was done to obtain specimens with a diversity of pathologies, as fresh, fixed tissue especially of small or infrequently encountered lesions are not readily available. While the images obtained are similar to others derived from fresh or fixed but unembedded specimens, they are not exact analogues, so this study can only be used to suggest the future promise of FIBI in clinical settings.

A similar study examined the use of MUSE to image fresh, non-sectioned skin tissue [31]. However, FIBI overcomes some of the limitations of MUSE. The UV excitation used by MUSE requires longer exposures that lengthens scan times, whereas FIBI employs visible light for excitation, generating intrinsically brighter images requiring shorter exposure times, currently in the few tens of milliseconds per field. Additionally, while MUSE uses fluorescent dyes, FIBI uses traditional H&E stains, which may make it easier to integrate the FIBI technology into existing histology workflows.

Other advances are being made in the slide-free histology arena. For instance, a similar study by Sun et al. [106] used third-harmonic generation and three-photon fluorescence microscopy to image H&E-stained skin tissue. They converted these images to standard H&E coloration with set algorithms for color mapping. Our study uses deep-learning-based color mapping with continued improvement and dynamic applications. In addition, our color camera image capture system is likely to be among the most affordable imaging technologies under development. Many newer technologies estimate costs of $65,000 to $400,000 USD [107].

Future work may explore whether special stains like periodic acid Schiff (PAS) and Prussian Blue can be used in conjunction with FIBI, but since many special stains can require multiple reagents and hours of preparation, this may negate some of the benefits of the rapid FIBI technology. Instead, we may explore the use of machine-learning-based algorithms to color-convert FIBI images to resemble special stains similar to how de Haan et al. converted standard H&E images into "virtual" Masson's Trichrome, Jones, and PAS stains [108].

4.5 - Conclusion

We demonstrate that FIBI microscopy is a promising tool for dermatopathology. It may be applicable for rapid and easy imaging of fresh, excised skin specimens in the clinic, without the need for fixation, tissue processing, or sectioning. These digitized FIBI images can be converted to standard H&E coloration to enable rapid pathologic and inform care decisions. For instance, FIBI could be used on fresh tissue in Mohs surgery without needing to wait for freezing or requiring extensive laboratory equipment. Since FIBI is rapid and non-destructive, if results prove to be non-diagnostic, the specimen can still be submitted for routine histopathology without delaying standard workflow. Future work aims to validate FIBI microscopy for dermatopathology applications and compare it to traditional methods for a variety of skin pathologies.

5. Label- and slide-free tissue histology using 3D epi-mode quantitative phase imaging and virtual H&E staining

5.1 - Introduction

Histopathology is the gold-standard for diagnosing disease, guidance of surgical margins during lesion resection, and overall clinical evaluation of tissue[1]. To visualize tissue architecture, labor-and-time-intensive tissue processing is currently required. During the most common histopathology procedure, an excised tissue specimen is fixed in formalin and paraffin embedded (FFPE), sectioned to generate micron-thick slices, and then mounted onto microscope slides. Those slides can then undergo a number of different staining procedures with the most common being hematoxylin and eosin (H&E) staining, in which hematoxylin stains cell nuclei purple and eosin stains the extracellular matrix, stroma, and cytoplasm pink[1]. This standard widely used process typically takes eight hours or more to complete. Consequently, fast, real-time tissue assessment with H&E-like contrast would have the potential to improve a number of medical procedures, ranging from surgical margin assessment to cancer screening and more.

In an effort to gain real-time pathology-level tissue assessments for use in surgery and other clinical fields, alternate microscopy techniques have been employed to provide imaging feedback during tissue excision. Some of these techniques include rapid tissue staining followed by linear[73], [109] and nonlinear fluorescence microscopy[22]; as well as label-free approaches ranging from ultraviolet-based methods and autofluorescence [110]–[112] to more complex nonlinear techniques[64], [113]–[115]. Many of these methods have also incorporated virtual staining pipelines to obtain images that are familiar to pathologists and thus avoid the need for further training on each imaging modality[22], [64]–[66], [73], [75], [109]. While promising, these methods have certain potential downsides, as they variously rely on staining the imaged tissues, employ UV light, and/or use complex and expensive nonlinear methods to achieve virtual histology. Further, translation of these technologies to in-vivo applications is challenging

or infeasible given the need for exogenous agents, concerns regarding tissue damage, and technological hurdles. These challenges limit the applicability of virtually stained microscopy and slide-free histology and point out the advantages of a microscopy method that could provide histopathologic information quickly (real-time), non-destructively, and with high-resolution in 3D, using simple, low-cost instrumentation.

To achieve these desired capabilities, we propose the use of virtual-H&E-stained images obtained with quantitative oblique back-illumination microscopy (qOBM) as a method of real-time histopathology for excised tissue samples, and with a clear path to future in-vivo applications. qOBM is a label- and fixative-free, wide-field, low-cost microscopy technique capable of obtaining sub-cellular resolution, quantitative phase images of thick, scattering tissue samples using same-side epi-illumination[116], [117]. (Thick, scattering samples refers to, for example, excised tissues without sectioning or intact organs such as brains, which cannot be imaged with transmission microscopes.) The level of 3D cellular and subcellular structural detail provided by this technology is comparable to that provided by label-free nonlinear microcopy methods, but with an embodiment that is simple and orders of magnitude cheaper, as it uses LEDs instead of femto-/pico-second lasers, is faster (wide-field vs point scanning), gentle on tissues and cells, and can be easily modified and miniaturized for in-vivo applications[37], [39]. Here we advance qOBM and the field of slide-free histology by introducing an image translation method by which qOBM images are virtually stained to resemble H&E-stained images.

The approach leverages deep learning, specifically generative adversarial networks (GANs)[60], which have been employed to generate virtual H&E histology from alternative microscopy modalities such as quantitative phase imaging[75], reflectance confocal microscopy[118] and photoacoustic remote sensing microscopy[119], among others[66]. This approach typically requires training datasets in which the alternative microscopy images can be pixel-registered with the target domain images (e.g., H&E), and most often relies on the use of thin tissue sections. Here, such pixel-registered datasets are unobtainable as qOBM imaging is performed on fresh tissue whereas ground-truth H&E images are subject to tissue

distortions from histological processes. To work around the lack of one-to-one pixel matching, we turn to cycle-consistent GANs (CycleGANs) [78]. Recent reports (using fluorescently labeled tissue and/or UV light) have demonstrated the utility of such networks for virtual H&E staining while relaxing the pixel-matching constraint[29], [70], [94]. Here, we demonstrate the efficacy of CycleGANs for virtual H&E staining of qOBM images. This combination has the potential to reduce the time needed to acquire H&E images from hours or even days to ~1 second.

To demonstrate the clinical utility of this method, we primarily focus on imaging brain tissue and differentiating between healthy and tumor regions (this represents one of many potential applications). To date, identifying brain tumor margins intraoperatively remains a significant clinical challenge; thus, neurosurgeons are often conservative with excised margins to minimize damage to healthy brain tissue vital for neurological function. However, this approach can lead to incomplete resections and tumor recurrence. Novel intraoperative methods such as 5-aminolevulinic acid (5-ALA) in-vivo staining have shown promise for improving clinical outcomes[120]–[122], but they are not without their limitations. For example, 5-ALA exhibits variable uptake based on brain morphology[121], and has limited sensitivity for low-grade disease and infiltrative tumor cells even in high-grade tumors[123]–[125]. Real-time, label-free image guidance with H&E-like contrast has the potential to significantly improve neurosurgical outcomes, particularly if deployed in situ (that is, in the surgical site rather than on excised specimens).

In this study, we first demonstrate conversion of qOBM images to vH&E (i.e., qOBM-to-vH&E conversion) using mouse liver specimens, which have a simple and homogenous structure, to establish the feasibility and effectiveness of the approach, as well as to show its utility for imaging a variety of tissue types. Then, we demonstrate qOBM-to-vH&E conversion using tissues from a rat glioma tumor model and human glioma specimens. To validate the results, we (1) trained a classifier on real H&E images of tumor and healthy tissues and then tested on virtual H&E images, and (2) performed a user study with five board-certified neuropathologists. The proposed qOBM-to-vH&E conversion pipeline permits a

novel histopathology workflow (Fig. 5.1) that has the potential to reduce the time and costs associated with obtaining histological H&E images. Further, the level of histological detail with H&E-like contrasts achieved by the proposed simple and label-free method is exemplary and paves the way for novel capabilities in a number of medical applications.

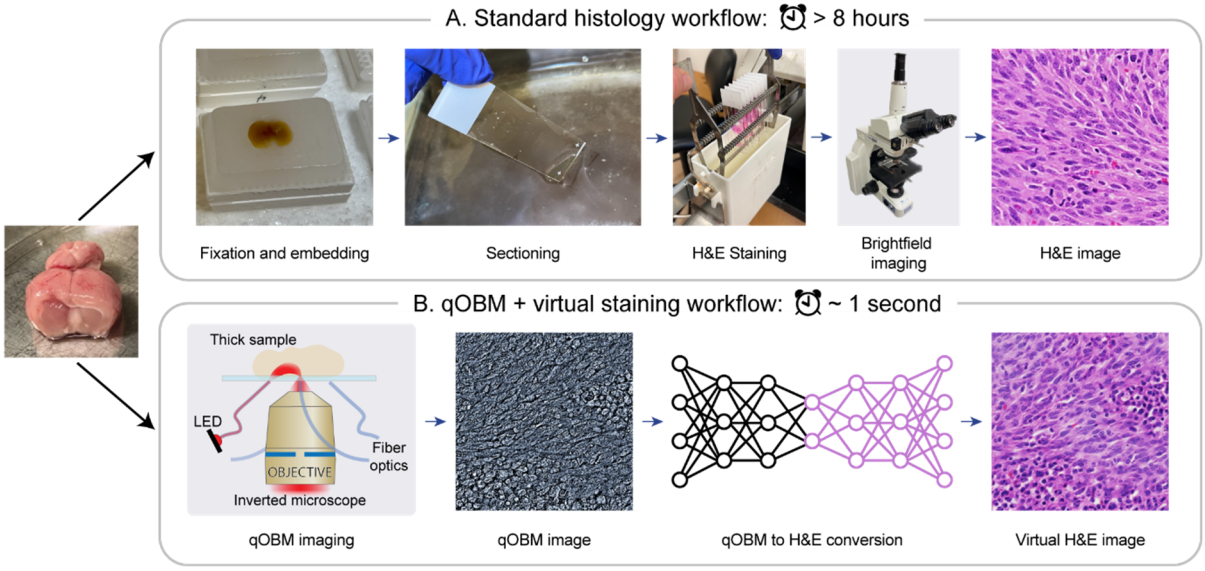

Figure 5.1 - Deep learning-enabled qOBM imaging workflow. (A) The standard histology workflow requires several sample preparation steps before viewing under a brightfield microscope and interpretation. This process can take about 8 hours or longer. **(B)** Our proposed workflow utilizes qOBM imaging to image a fresh specimen of tissue and virtual staining to obtain similarly interpretable images in about 1 second.

5.2 - Methods

5.2.1 - Label-free qOBM imaging

The qOBM system consists of a conventional inverted microscope with a modified epi-illumination scheme, as shown in Fig. 5.1B. The illumination consists of four LED light sources (720nm) coupled into 1mm multimode fiber optics with a 0.5 NA. The fibers are evenly distributed around the microscope objective (Nikon Plan Fluor ELWD, 60x, 0.7 NA) at a 45-degree angle from the optical axis. LEDs illuminate samples sequentially, and for each illumination, a raw bright field image is collected. By way of multiple scattering, this illumination configuration produces an effective oblique illumination[15], [116]. Upon subtraction of two captures with diametrically opposed illumination, we obtain a differential

phase contrast (DPC) image, I_{DPC}, which provides tomographic cross-sectioning capabilities with qualitative differential phase contrast.

To reconstruct a 3D quantitative phase image with qOBM, two DPC images from orthogonal angles (or shear directions) are processed and deconvoluted with the system's optical transfer function through a Tikhonov regularized deconvolution following,

$$\phi = \mathcal{F}^{-1}\left\{\frac{\sum_k \bar{I}_{DPC}^k \cdot C_{DPC}^*}{\sum_k |C_{DPC}|^2 + \alpha}\right\},$$

Here, ϕ represents the quantitative phase, $\bar{I}_{DPC}^k$ is each DPC image along the k^{th} shear direction, alpha is a regularization parameter, and C_{DPC} is the optical transfer function of the system, which can be obtained by characterizing the distribution of the multiple-scattered light passing through the focal plane within the sample[116], [117].

The qOBM images capture the quantitative phase of the samples, which is directly correlated to the refractive index and dry mass of the sample. Additionally, the qOBM images show outstanding detail in all directions of illumination, have diffraction limited resolution (~0.6 μm), and a sensitivity of ~2 nm.[37], [116] qOBM image acquisition is at 10Hz (limited by the frame rate of the camera) and processing of the quantitative phase images is achieved in real-time using a regular table top computer.

5.2.2 - Sample preparation and imaging

In this work, we studied the virtual staining of qOBM images from 3 types of tissues: mouse liver, rat brain 9L gliosarcoma tumor model, human brain tumors. All animal tissue excision and imaging protocols were approved by Institutional Animal Care and Use Committee of the Georgia Institute of Technology. All human samples were de-identified and obtained through the Winship Cancer Institute of Emory University using approved protocols. Tissues were imaged fresh and untreated, ex-vivo within 6 to 12 hours of removal. The imaged mouse livers from 8 healthy animals were donated by the Haider lab at Georgia Tech and Emory University, from mice sacrificed for various purposes. The livers were excised

and imaged fresh within 3 hours of the procedure. Details about the 9L gliosarcoma rat tumor model protocol and imaging may be found in Costa et al.[37] In short, 14 Fisher rats were intracranially implanted with 9L gliosarcoma cells. The animals were sacrificed 9-12 days after the implant, and brains were excised, cut coronally to expose the tumor, and imaged fresh within 12 hours of extraction. In this animal model, the tumor is confined to the side of the brain where the tumor cells were implanted, leaving the counter-lateral side of all treated brains as an additional control. This also allows for a priori knowledge of the location of the tumor. The human tissue from N = 5 patients were imaged post-surgery, within 6 hours of recession.

The qOBM imaging sessions consisted of multiple lateral and axial scans of different regions of each tissue. These scans were performed in an automated manner, enabled by the X-Y-Z automatic stages built into the microscope. Axial stacks were taken by translating the objective by 1 µm steps. The lateral scanning was performed with an overlap of 20% to facilitate stitching of mosaics and combined with axial scans.

After imaged with qOBM, all tissues were formalin-fixed for 48 hours, processed, and embedded in paraffin. Then, the samples were sliced into 5µm sections and stained with H&E. The whole H&E sample slides were then digitally scanned by an Olympus NanoZoomer whole slide scanner at either 20x or 40x magnification. Finally, the H&E slide scans were inspected to select similar regions to those acquired with qOBM for the CycleGAN training process, described below.

5.2.3 - Virtual H&E staining with CycleGAN

We define two image domains, one for qOBM images (X), and one for H&E images (Y). We attempt to determine a transformation $G: X \rightarrow Y$. In the CycleGAN framework used here[78], there are two tasks. One task is to learn $G_X: X \rightarrow Y$ that maps $x \in X$ to $y \in Y$. The auxiliary task is to learn a generator $G_Y: Y \rightarrow X$. Additionally, we have adversarial discriminators D_X and D_Y. D_X discriminates between the fake outputs of G_X and real images from the domain Y. On the other hand, D_Y discriminates between the

fake outputs of G_Y and real images from the domain X. The CycleGAN framework then exploits the cycle-consistency property that $G_Y\big(G_X(x)\big) \approx x$ and $G_X\big(G_Y(y)\big) \approx y$. This is expressed as the following loss:

$$\mathcal{L}_{cycle}(G_X, G_Y) = \mathbb{E}_{x\sim p_{data}(x)}\left[\left\|G_Y\big(G_X(x)\big) - x\right\|_1\right] + \mathbb{E}_{y\sim p_{data}(y)}\left[\left\|G_X\big(G_Y(y)\big) - y\right\|_1\right]$$

where $\|\cdot\|_1$ is the L1 norm. This is trained with traditional least-squares adversarial losses:

$$\mathcal{L}_G(D, G, X, Y) = \mathbb{E}_{x\sim p_{data}(x)}\left[\big(D\big(G(x)\big) - 1\big)^2\right]$$

$$\mathcal{L}_D(D, G, X, Y) = \frac{1}{2}\mathbb{E}_{y\sim p_{data}(y)}[(D(y) - 1)^2] + \frac{1}{2}\mathbb{E}_{x\sim p_{data}(x)}\left[\Big(D\big(G(x)\big)\Big)^2\right]$$

Finally, for regularization, an identity constraint is imposed:

$$\mathcal{L}_{idt}(G_X, G_Y) = \mathbb{E}_{x\sim p_{data}(x)}[\|G_Y(x) - x\|_1] + \mathbb{E}_{y\sim p_{data}(y)}[\|G_X(y) - y\|_1]$$

Thus, the full objective is:

$$\min_{\mathrm{G}} \mathcal{L}_{full} = \lambda_{cyc}\mathcal{L}_{cycle}(G_X, G_Y) + \mathcal{L}_G(D_Y, G_X, X, Y) + \mathcal{L}_G(D_X, G_Y, X, Y) + \lambda_{idt}\mathcal{L}_{idt}(G_X, G_Y)$$

$$\min_{\mathrm{D}} \mathcal{L}_{full} = \mathcal{L}_D(D_Y, G_X, X, Y) + \mathcal{L}_D(D_X, G_Y, X, Y)$$

where $\lambda_{cyc} = 10$ controls the importance of the cycle-consistency loss, and $\lambda_{idt} = 0.5$ controls the importance of the identity loss.

The generator architecture (G_X, G_Y) was a ResNet-based fully convolutional network described in Zhu et al.[78] Unless otherwise specified, the generator had nine residual blocks. A 70x70 PatchGAN[81] was used for the discriminator (D_X, D_Y). Unless otherwise specified, the discriminator had three layers. The same loss function and optimizer as described in the original paper[78] was used. The learning rate (LR) was fixed at 2e-4 the first 100 epochs and linearly decayed to zero in the next 100 epochs. A batch size of 4 is used.

qOBM images were center-cropped to 1536x1536 pixel images and divided into nine 512x512 tiles. Unless otherwise noted, all qOBM images were contrast-inverted. The H&E images were upscaled with bilinear interpolation by a factor of either 1.5x or 2x (depending on the dataset) such that the images had features of comparable pixel dimensions to those in the qOBM images.

To enable a scalable inference pipeline, we utilized a tiled inference procedure as described in Abraham et al.[94] Briefly summarized, the model was applied to overlapping 512x512 tiles of the original FOV and the tiles were stitched by defining a given pixel's intensity as the weighted average of intensity values from the vH&E patches which overlapped at the given pixel location. The weighting was based on a Gaussian kernel.

Since four raw captures are taken with qOBM, from which two DPC images are reconstructed, single capture- and DPC-to-vH&E conversion was also performed and compared to qOBM-to-vH&E (the images used for training come from the exact same fields of view), except the images were not inverted, since the nuclei appeared dark and therefore should be the best-case scenario for conversion efforts. Neither the raw capture nor the DPC image approaches supported good CycleGAN conversions (Supplementary Fig. 5.3).

For conversion of rat brain, the single model trained on all four observed tissue subtypes simultaneously used a larger model. As commonly noted with CycleGANs, model size played a role in conversion performance (see Supplementary Note 5.2). Our larger model had twelve residual blocks in the generator and six layers in the discriminator. Fine-tuning of the rat CycleGAN on the human specimens simply consisted of initializing the model with the rat CycleGAN model weights and training at an LR of 2e-5. When using the high-resolution H&E for fine-tuning instead, the usual LR of 2e-4 was applied. For conversion of the qOBM strip, the full stitched strip is taken and passed into our tiled inference algorithm, rather than the individual FOVs from the strip.

5.2.4 - Quantitative evaluation of virtual H&E staining results

We first trained a convolutional neural network on standard brightfield H&E images to classify between healthy (cortex or basal ganglia) regions and tumor regions. We performed five-fold cross validation. The model was trained on a total of 1744 standard H&E images, so in each fold, this leads to a train-validation split of 1395 - 349 image tiles. An ImageNet-pretrained ResNet18[49] was fine-tuned with a batch size of 128 and for 4 epochs. In the first epoch, only the linear head layer was trainable, and the remaining the model weights were frozen (not updatable). It was trained with a LR of 1e-2 with a short LR warmup followed by a cosine decay. The remaining three epochs were trained with all layers updatable, with a base LR of 5e-3, but using "discriminative LRs" [43] where early layers in the neural network have even lower LRs. These three remaining epochs were trained with a one-cycle LR schedule [126]. The mean and standard deviation of the accuracies for the classifiers trained on each of the five folds were reported.

Once accurate H&E healthy vs. tumor classifiers were trained, they were applied to vH&E images. The accuracy was calculated by comparing the labels predicted by the classifier to the ground truth labels of the original qOBM images. This was one for each of the five trained classifiers, and the mean and standard deviation of the accuracies were reported.

5.2.5 - Computational Hardware and Software

All deep learning models were trained on NVIDIA A100 80GB GPUs. The PyTorch (version 1.9.1) [83], fastai (version 2.6.3) [84], and UPIT (version 0.2.3) [127] libraries were used for training and inference of all models.

5.2.6 - Clinical validation of vH&E images of brain tissue

To evaluate the quality and usefulness of the virtually stained qOBM images compared to the gold standard H&E-stained images, we conducted a panel study with 5 board-certified neuropathologists. In this study, the neuropathologists were asked to evaluate a total of 100 180 µm x 180 µm images. The image set contained 30 real H&E rat brain images (10 tumor, 10 healthy, and 10 mixed fields of tumor

and healthy), 30 virtually stained qOBM images (10 tumor, 10 healthy, and 10 mixed fields of tumor and healthy), 20 real H&E human brain tumor images, and 20 virtually stained qOBM human brain tumor images. The order of images presented in the survey was randomized with healthy and tumor regions from both humans and rats combined. For each image, neuropathologists were asked if tumor cells were present in the image (Y/N/Cannot assess), based on the image if they would recommend continued resection of the area (Y/N), and how confident they were in giving that recommendation with numerical scores (1, unsure to 5, very confident).

5.3 - Results

5.3.1 - Virtual staining of label-free qOBM images of fresh mouse liver

To establish the feasibility and effectiveness of unpaired image-to-image translation from qOBM to H&E, we first attempted to generate vH&E images of healthy mouse liver specimens, which demonstrate a consistent, well-defined microanatomy primarily comprising of well-organized hepatic cells and blood vessels. qOBM images of freshly excised liver tissue specimens (N=8), donated from otherwise discarded tissue, were obtained with a 60X objective (0.7 N.A., 270 x 270 μm field of view, with lateral resolution of 0.6 μm and cross-sectional/axial resolution of 2.5 μm). qOBM images, including real-time processing, were acquired at 10Hz. All animal experimental protocols were approved by Institutional Animal Care and Use Committee (IACUC) of the Georgia Institute of Technology and Emory University. Tissues were subsequently submitted for histological processing to obtain H&E slides (sections were ~5 μm thick). Prior to CycleGAN training, the qOBM images were contrast-enhanced and grayscale inverted. The images were divided into 512 x 512 pixel (~ 70 x 70 μm) tiles for training. We used a standard ResNet-based generator architecture and a PatchGAN discriminator, training on 2358 qOBM and 1737 H&E tiles for 200 epochs at a batch size of 4.

Figure 5.2 shows representative results. First, the native qOBM phase images (Fig. 5.2A) show clear cellular and subcellular detail that closely parallels the structure of the traditional H&E images (Fig. 5.2C), making qualitative assessment of the translation relatively simple. For example, in qOBM, with

contrast generated by the refractive index properties of the tissue, hepatocyte nuclei appear dark and possess subtle but appreciable subnuclear structure/texture (shown in insets), while red blood cells appear bright. Figure 5.2B shows the translated vH&E image, which preserves the general structure of the qOBM image, with a high-fidelity style conversion to H&E. Specifically, nuclear and subnuclear structures of the hepatocytes are converted appropriately, with the expected purple hue and texture. The network also correctly enhances and converts nuclei that can be difficult to identify in qOBM (white arrow), although some are occasionally missed (yellow arrow). The missed nuclei occur in areas near capillaries; this is likely due to the fact that the capillary structures in the qOBM images of fresh tissues are different (better preserved and continuous) than in the target H&E images of processed tissue sections in which the capillaries appear more fragmented (blue arrows highlight vessel structures). Consequently, the network may at times not appropriately deal with such structures. Training with more data could potentially resolve these small errors; nevertheless, the overall structure of the tissue is well preserved and is consistent with the appearance of healthy mouse liver.

We also note that structures observed in qOBM that are not present in H&E, such as small bright white droplets—likely composed of lipids—are correctly ignored in the vH&E images and do not produce unwanted artifact. And red blood cells, also depicted in bright white in the phase image, are correctly translated to their characteristic bright red hue in H&E. These results confirm that CycleGANs can successfully translate qOBM quantitative phase images of thick fresh tissue to H&E-like images without needing pixel-matched paired images.

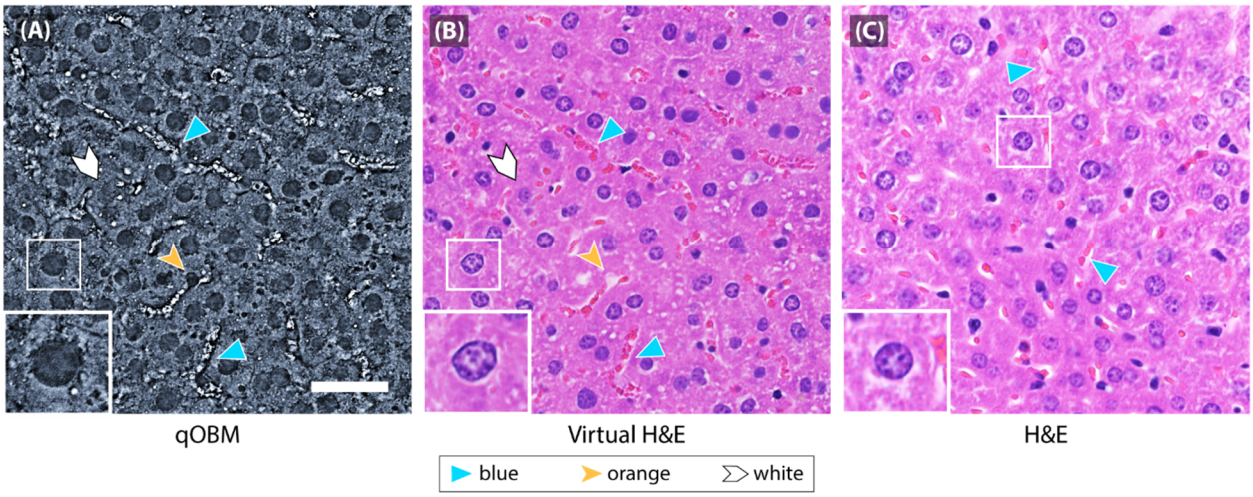

Figure 5.2 - qOBM-to-vH&E conversion of mouse liver tissue. (A) Label-free 60x qOBM image of mouse liver tissue. **(B)** Corresponding vH&E image. **(C)** Standard brightfield H&E image provided for comparison. The white boxes and insets show a representative appropriately converted hepatocyte with appreciable subnuclear detail, the yellow arrows refer to nuclei missed by the conversion, and the blue arrows refer to capillaries. Scale bar is 50 µm.

5.3.2 - Virtual staining of label-free microscopy images of rat brain tumor

Having established the qualitative ability to translate qOBM images into vH&E using a relatively simple and homogeneous sample type, we next turn to the more challenging task of virtually staining complex brain tissue (healthy and tumor) and later providing quantitative metrics of translation fidelity.

qOBM imaging of fresh tissues from a 9L gliosarcoma rat tumor model (N = 14) was performed as described in Costa et al.[37] (also see Materials and Methods); this tumor was chosen because of its similarity to high-grade human gliomas. Treated animals had tumors confined to one hemisphere, leaving the other as control. Two healthy mice were also imaged and analyzed as additional controls (thus a total of N=16 animals were analyzed). Images were acquired with a 60X, 0.7NA objective. During the imaging sessions, the brains were scanned laterally and axially (volumetrically) in an automated manner to acquire data from different regions of the brain. Following qOBM imaging, the brains were formalin fixed, embedded in paraffin wax, cut into thin (5 µm) sections, and stained with H&E.

Four general tissue subtypes were observed and characterized with qOBM in the 9L gliosarcoma model. Figures 3A, B show two densely hypercellular tumor regions, one with a malignant sarcomatous

population (Fig. 5.3A), and another with a malignant glial component (Fig. 5.3B). This biphasic tumor tissue pattern is characteristic of gliosarcomas. Additionally, Fig. 5.3C demonstrates healthy basal ganglia (with the presence of white matter bundles) and Fig. 5.3D shows healthy cortex. We trained a single CycleGAN model for qOBM-to-vH&E conversion on an image set representing all four subtypes with a total of 1377 qOBM and 1744 H&E tiles of size 512 x 512 pixels, trained for 200 epochs at a batch size of 4. Qualitatively, the CycleGAN provides qOBM-to-vH&E conversions (Fig. 5.3E, F, G, and H) that are remarkably similar to standard H&E, provided for comparison in Fig. 5.3I, J, K, and L. For instance, Fig. 5.3E (vH&E) clearly shows the same overall pleomorphic, herringbone-shaped spindle cell structure shown in Fig. 5.3I (real H&E), and Fig. 5.3F shows hyperchromatic appearance (dark purple color) of the tumor cells. In the basal ganglia, the vH&E image clearly shows the eosinophilic (deep pink color) white matter bundles, consistent with the real H&E image (Fig. 5.3K). Finally, cortex regions such as normal basal ganglia exhibit the appropriate cellularity, with blood cells (with large phase values) correctly translated to an intense red hue.

Figure 5.4 shows qOBM-to-vH&E conversion of specimens that were not shown to the network during training, consisting of an admixture of healthy brain and tumor. The conversion is successful and shows excellent agreement with the style and appearance of real H&E images. Specifically, the examples in Fig. 5.4 show clear lines of delineation between the tumor and brain tissue, and a mesenchymal transition characteristic of the 9L gliosarcoma rat model. The non-tumor brain tissue also demonstrates reactive characteristics such as high cellularity as expected of tissue adjacent to tumor. These results highlight the ability of the qOBM-to-vH&E conversion network to make correct inferences even when presented with structures outside of those explicitly provided in training. We attribute this capability, in part, to the close resemblance of the native qOBM phase images to histology, where again the style/mode difference between qOBM to H&E is relatively minor (particularly when compared to other label-free 3D scattering-based imaging technologies[118], [128]).

To quantitatively evaluate the qOBM-to-vH&E conversion, we trained a convolutional neural network classifier to discriminate between H&E images of healthy and tumor tissue and observed its performance on vH&E images. The tissue class (i.e., ground truth healthy vs. tumor) for each qOBM and H&E image was known a priori based on the anatomical location of the implanted tumor cells. The classifier was trained with 5-fold cross validation on 1395 real H&E tiles to discriminate between healthy and tumor, which yielded an accuracy of 99.4 ± 0.8% on a held-out test set of 349 512 x 512-pixel tiles. The classifier was then employed on 270 vH&E tiles generated by the CycleGAN and displayed an accuracy of 95.2 ± 2.8% (Fig. 5.5). This suggests that the translated images preserve both the style and diagnostic information content of the traditional H&E images.

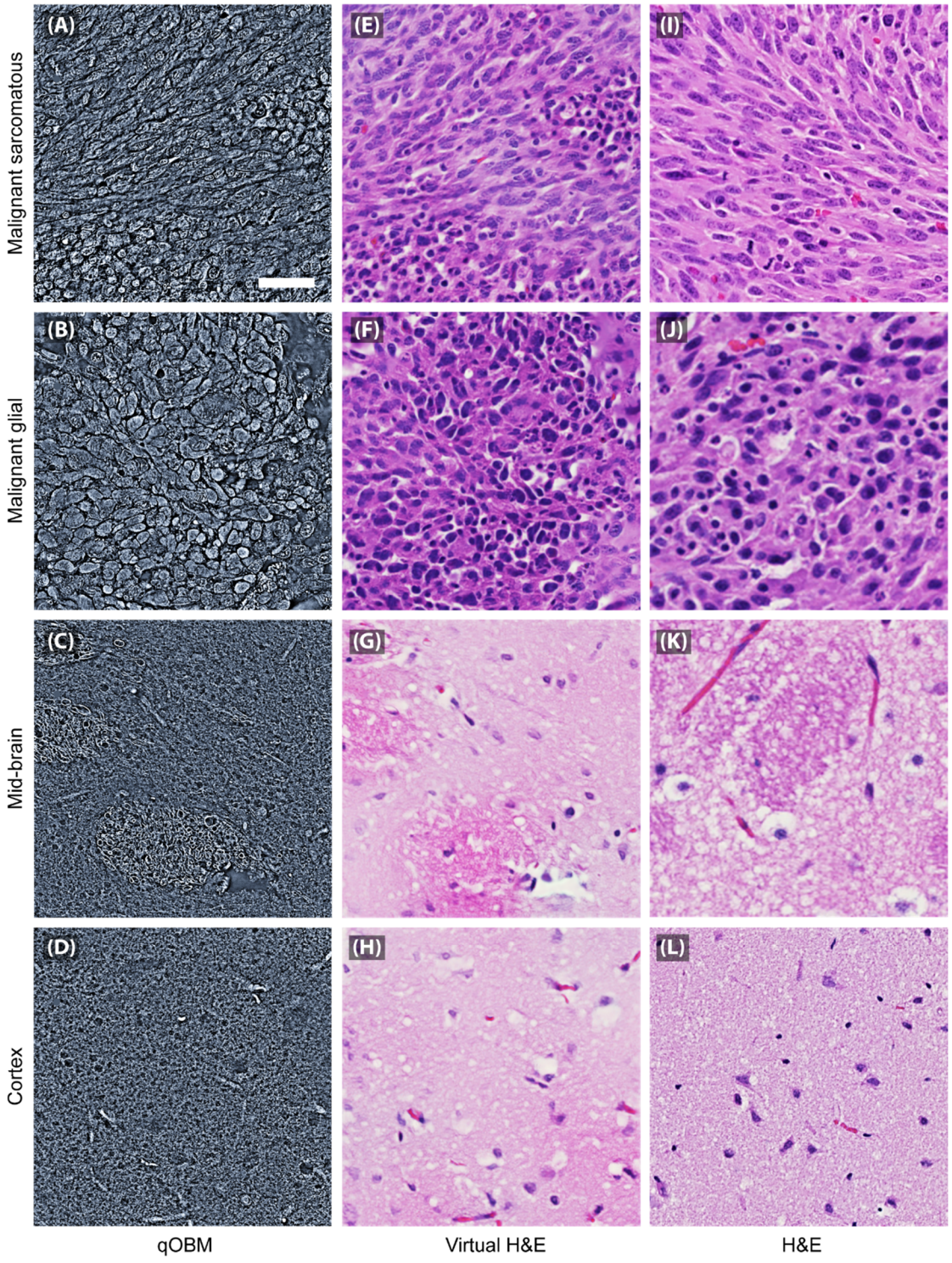

Figure 5.3 - qOBM-to-vH&E conversion of brain tissue from the 9L gliosarcoma rat tumor model. **(A)-(D)** Label-free 60x qOBM images of each of the four rat brain tissue subtypes, including two types of tumor structure (A and B), heathy basal ganglia (C) and healthy cortex (D). **(E)-(H)** Corresponding vH&E images produced by a CycleGAN trained on rat brain images. **(I)-(L)** Standard brightfield H&E images of the same tissue subtypes, provided for comparison. Scale bar is 50 µm.

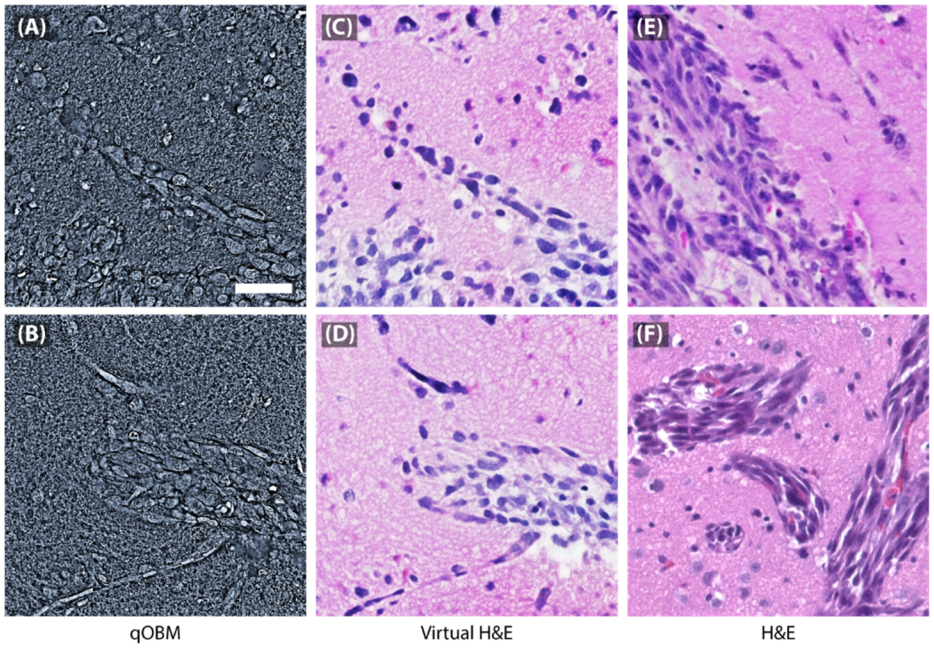

Figure 5.4 - qOBM-to-vH&E conversion for images with a mix of healthy and tumor rat brain tissue, never seen during training. (A)-(B) Label-free 60x qOBM images of mixed rat brain tissue. **(C)-(D)** The corresponding vH&E images. **(E)-(F)** Standard brightfield H&E images of the same tissue subtypes, provided for comparison. Scale bar is 50 µm.

(A)

Accuracy of a healthy vs tumor tissue classifier	
Standard H&E	99.4 ± 0.8 %
Virtual H&E	95.2 ± 2.8 %

(B)

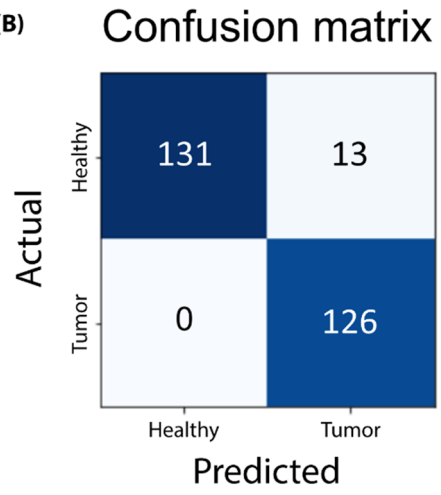

Figure 5.5 – Quantitative evaluation of qOBM-to-vH&E conversion for rat brain tissue. A classifier trained on standard H&E images to differentiate between tumor and healthy images is assessed using vH&E images. Summary of results: **(A)** accuracy of training H&E set with 5-fold cross-validation and the accuracy of the vH&E test set. **(B)** A confusion matrix of this H&E healthy/tumor classifier applied to the vH&E images.

5.3.3 - Virtual H&E staining of mosaics and tomographic volumes

The qOBM system used in these studies was equipped with lateral and axial automated stages that enable scanning tissue in all directions to create large mosaics, as well as tomographic volumetric datasets. Figure 5.6 demonstrates a virtual H&E strip mosaic (6.3 mm x 270 µm) of a rat brain, while Fig. 5.7 shows a vH&E 3D rendered volume (270 µm x 270 µm x 60 µm) of a rat brain tumor margin. In Fig. 5.6, the overall margin delineation between tumor tissue and normal tissue based on the cellularity is clearly apparent, with excellent agreement to H&E. Figure 5.7 demonstrates a transition from a glial tumor subtype surrounded by basal ganglia tissue structures into the sarcomatous tumor subtype, which is clearly apparent in the vH&E images. Here the robustness of the vH&E translation is evident and demonstrates a consistent color and structure in the reconstructed images stitched or stacked together using a standard process (see Materials and Methods), with no special consideration for the mosaic or volumetric nature of the datasets.

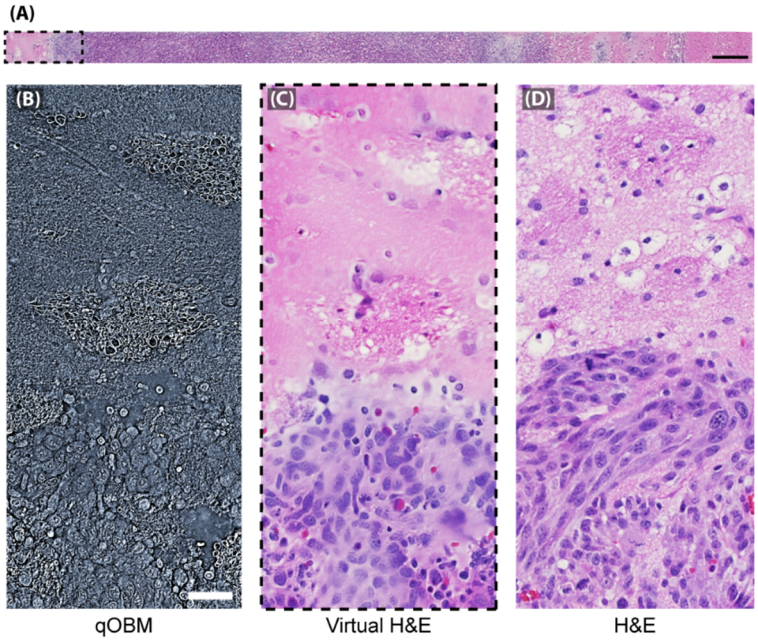

Figure 5.6 - Label-free qOBM imaging of a strip of rat brain tissue and corresponding vH&E. A virtual H&E strip mosaic of rat brain tumor obtained by applying the CycleGAN trained on rat brain to the whole mosaic at once. **(A)** Virtual-H&E mosaic (6.3mm x 270µm). Scale bar is 300 µm. **(B)** A zoomed-in region of the label-free 60x qOBM strip (600µm X 270µm). Scale bar is 50 µm. **(C)** A zoomed-in region of the corresponding vH&E strip. **(D)** A zoomed in region of a brightfield H&E strip region provided for comparison.

5.3.4 - Virtual staining of label-free microscopy images of human glioma specimens

To demonstrate the potential clinical utility of the approach, the CycleGAN deep learning pipeline was employed to virtually stain qOBM images of human astrocytoma specimens. Samples consisted of freshly excised human brain tumor and tumor-edge regions of infiltrating grade 2 and grade 3 astrocytoma specimens discarded from neurosurgery. Five patient samples were analyzed. All tissues were imaged fresh within 6 hours of removal, and no modifications were made to the tissues prior to the qOBM imaging process. It is important to note that the margins of these types of infiltrating tumors, especially grade 2 astrocytomas, are extremely difficulty to identify intraoperatively, particularly in vivo where existing assessment tools lack sensitivity. All human samples were de-identified and obtained through the Winship Cancer Institute of Emory University using approved protocols.

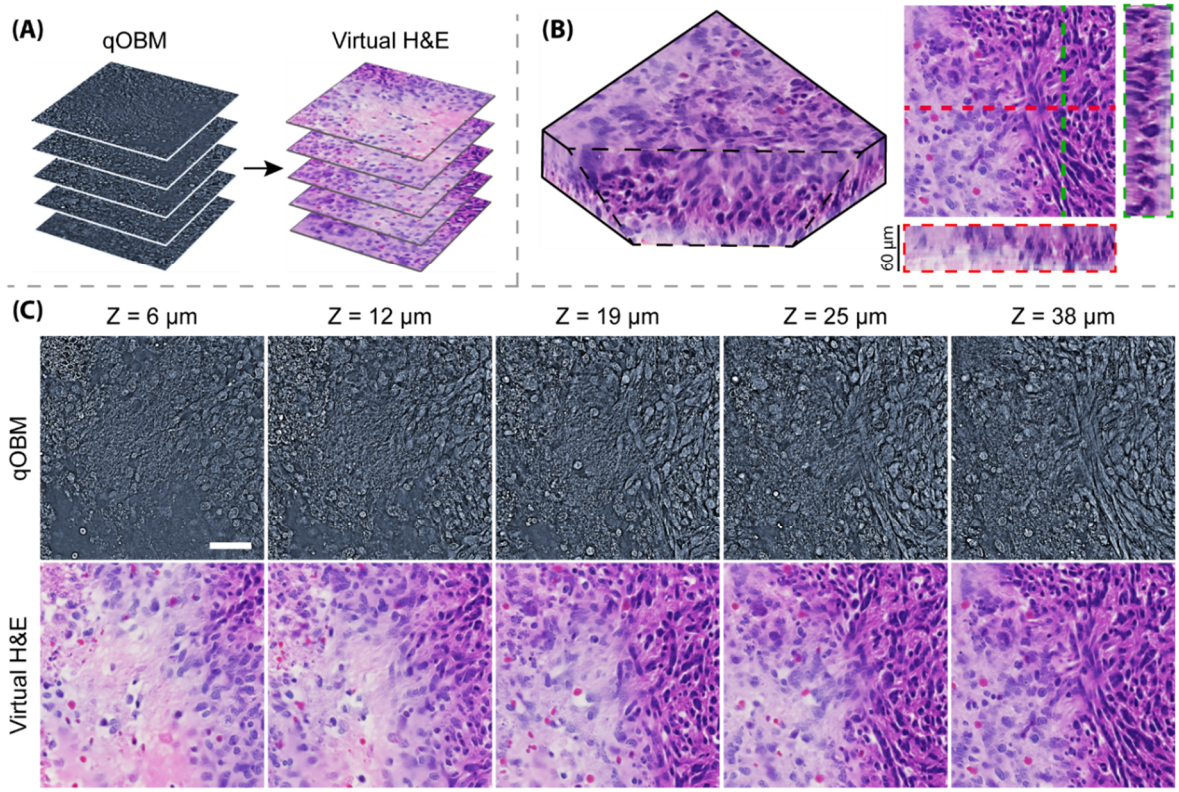

Figure 5.7 - A qOBM and corresponding vH&E 3D volumetric stack of a rat brain tumor margin. A virtual-H&E volumetric stack (270 µm x 270 µm x 60µm) obtained by applying the trained rat brain CycleGAN to each image in the stack. **(A)** qOBM-to-vH&E conversion of the volumetric stack is depicted. **(B)** vH&E volume, with X-Y, X-Z, and Y-Z cross sections shown. **(C)** qOBM image slices at various depths and the corresponding vH&E image slices. Scale bar is 50 µm.

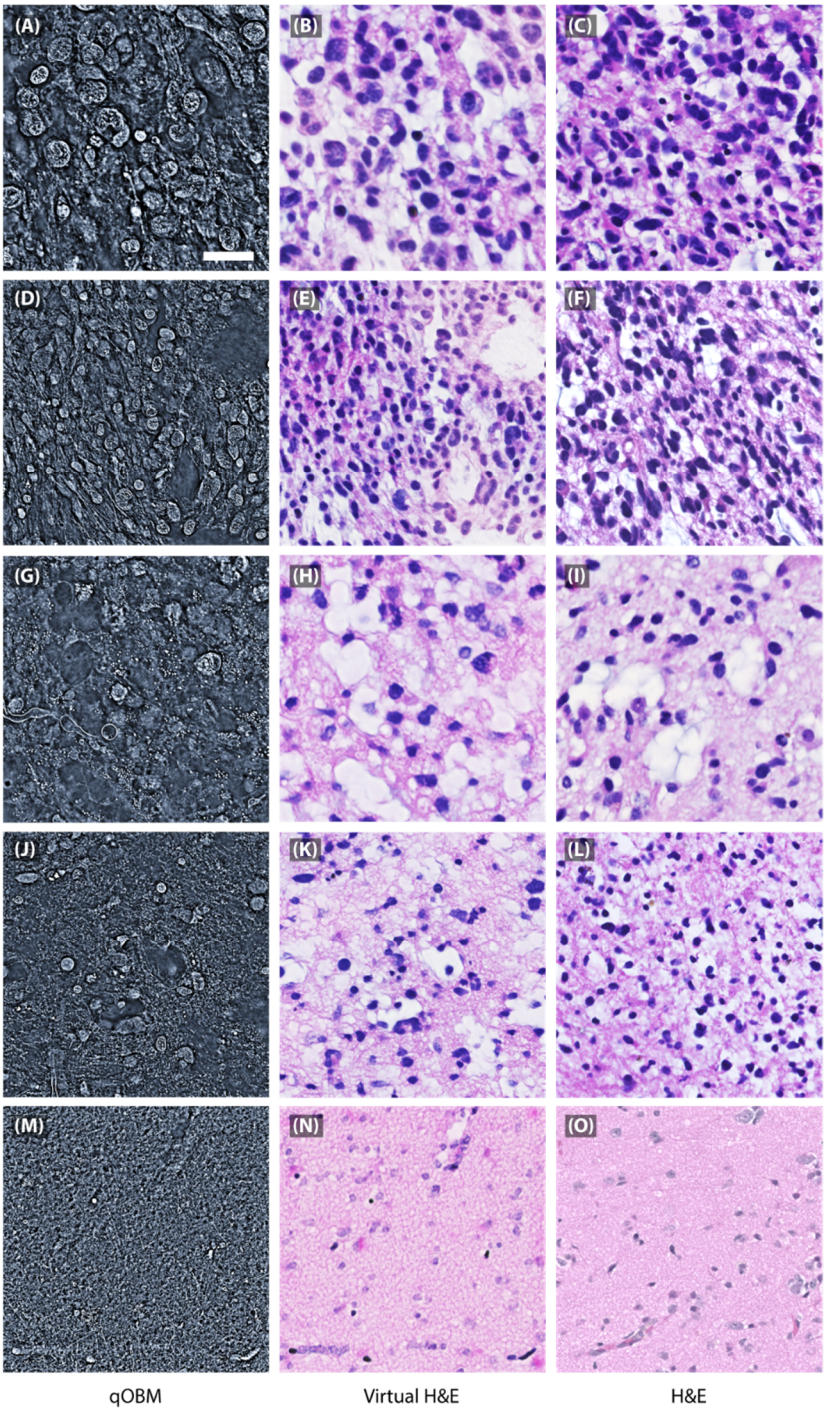

Figure 5.8 - qOBM-to-vH&E conversion of human gliomas. Each row contains a qOBM image, corresponding vH&E, and standard brightfield H&E images, provided for comparison. **(A)-(I)** Three separate human grade 3 glioma specimens (one per row). **(J)-(L)** Human grade-2 (low-grade) glioma specimen. **(M)-(O)** Healthy human tissue specimen from the edge of a grade 3 astrocytoma. Scale bar is 50 µm.

We continued training the CycleGAN developed for rat brain tissue on an additional 837 qOBM and 372 H&E tiles of human glioma tissue. This process is often referred to as transfer learning or fine-tuning[129]. Qualitatively, this fine-tuned model performed significantly better on human specimens than when we attempted to apply a neural network trained exclusively on rat specimens (Supplementary Fig. 5.5). We also compared our fine-tuned model to training from scratch on the human glioma images alone (Supplementary Fig. 5.5E, F), observing that the fine-tuned model demonstrates significantly better subnuclear detail, especially when trained with higher resolution H&E images (Fig. 5.8).

Figure 5.8A-F show two human grade 3 astrocytomas, clearly identifiable due to their hypercellular and hyperchromatic tumor cells. In the qOBM phase images, the cells are tightly packed and display rough intranuclear texture; these are appropriately translated in the vH&E image. In Fig. 5.8G-I, we see another hypercellular human grade 3 astrocytoma. Both the virtual and real H&E show atypically shaped cells and nuclei that are an important indicator of tumor presence. Note that the qOBM image (Fig. 5.8G) contains small bright white dots throughout the image which we have exclusively observed in brain samples from patients who have received prior radiation treatments (data from a parallel study[130]). These features are only visible in the qOBM images of fresh tissues and vanish after FFPE H&E processing. Interestingly, the digital conversion to vH&E also suppresses the appearance of these structures. This is similar to the results presented in Fig. 5.2, where the lipid-like structures present in the qOBM images of liver are not displayed in the corresponding vH&E image as they are absent in the target domain H&E images. Figure 5.8J-L, present a human grade 2 (low-grade) astrocytoma. Here we observe, in both the virtual and real H&E, moderate cellularity and nuclear pleomorphism. This shows the potential of the proposed method to correctly capture H&E-like histological detail indicative of low-grade disease, which again, is extremely difficult to identify intraoperatively with existing intraoperative tools. Finally, Fig. 5.8M-O, presents a healthy human tissue specimen from the edge of a grade 3 astrocytoma tumor, where the vH&E image resembles the real H&E image, with both showing regularly shaped cell nuclei without hyperchromasia and at the expected density for normal tissue.

Volumetric stacks of human gliomas specimens can also be obtained and virtually stained, allowing us to gain additional insight about the specimen. For example, Fig. 5.9 shows a volume of a human grade 3 astrocytoma where the first most shallow image exhibits a structure consistent with normal brain tissue with the exception of a single atypical cell (as indicated by the arrow in Fig. 5.9C at a depth of Z = 2 µm). These characteristics alone would not be sufficient to diagnose as tumor or warrant excision of the tissue if seen in-vivo intraoperatively. However, as we image deeper into the sample, the tissue exhibits higher cellularity with larger, hyperchromatic cells becoming evident, reflecting the presence of tumor. By being able to move axially (deeper) into the tissue, we can gain additional information, including seeing increased counts of more irregular nuclei, which indicates tumor.

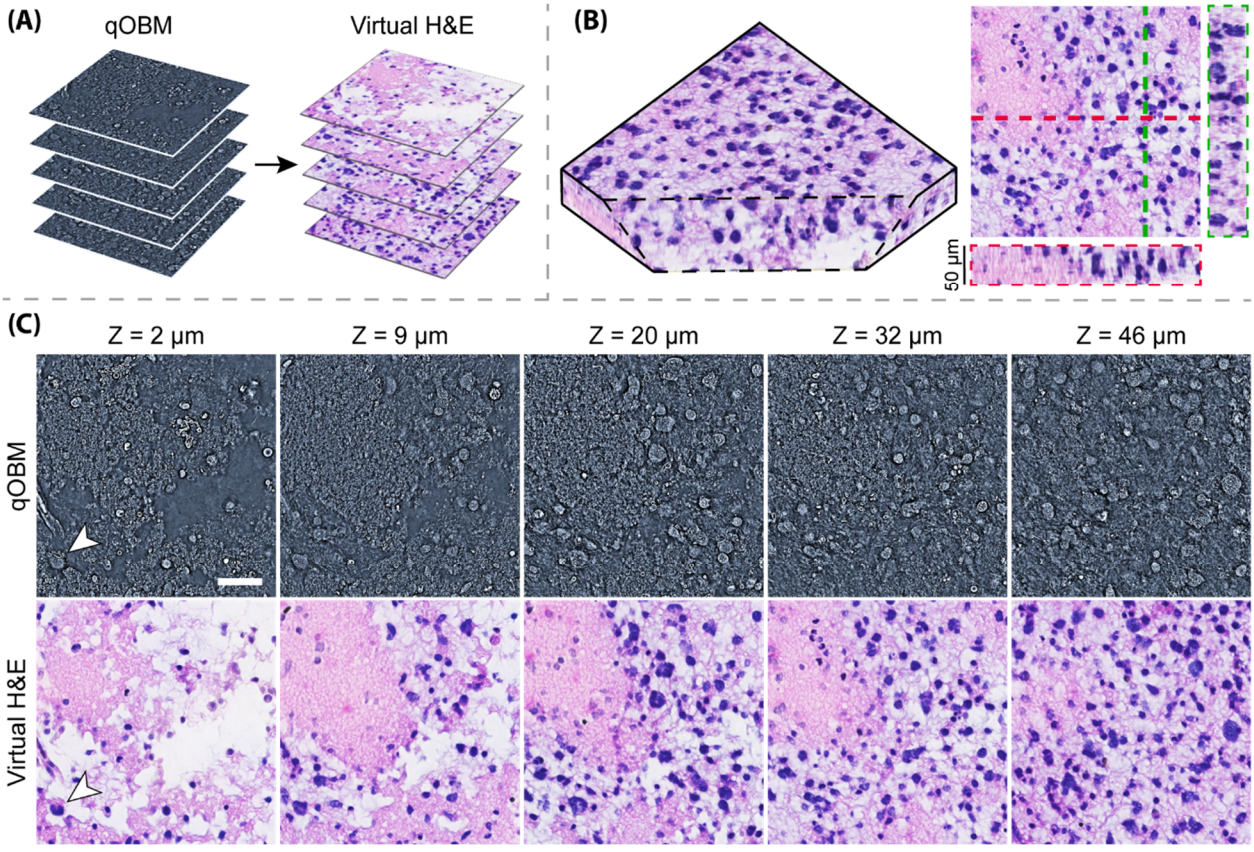

Figure 5.9 - A qOBM and corresponding vH&E 3D volumetric stack of a human glioma margin. A virtual H&E volumetric stack obtained by applying the trained human glioma CycleGAN to each image in the stack. **(A)** qOBM-to-vH&E conversion of the volumetric stack is depicted. **(B)** vH&E volume, with X-Y, X-Z, and Y-Z cross sections shown. **(C)** qOBM image slices at various depths and the corresponding vH&E image slices. The white arrow highlights an irregular nucleus. Scale bar is 50 µm.

5.3.5 - Neuropathologist validation of virtually stained qOBM images

To further validate the potential clinical utility of the virtually stained qOBM images, we performed a user study with American Board of Pathology certified neuropathologists. We collated a set of 30 vH&E images of the rat brain tumor model and 20 vH&E images of human gliomas along with corresponding real H&E images, giving a total of 100 images. These images were reviewed by five neuropathologists, who were asked to respond to 3 questions: (1) Are tumor cells present in the image? (Y/N/Cannot assess); (2) If this field of view were representative of a larger region, would you recommend continued resection? (Y/N); and (3) How confident are you in this evaluation? (1, unsure to 5, very confident).

To assess accuracy, we designated the following criteria: For the H&E and vH&E images of the animal model, ground truth was based on a-priori knowledge of the location of the tumor (see Methods and Materials). For the human H&E images, ground truth was taken to be the consensus answer from the five neuropathologists. For the vH&E images, ground truth was based on the evaluation of the same specimens after H&E processing, which in this case also agreed with consensus of the vH&E images.

Parameter	H&E	Virtual H&E	Statistical Significance
Accuracy	94%	96%	N.S.
Overall Group Concordance	0.74	0.81	-
Diagnostic Confidence	4.6	4.7	N.S.

Table 5.1 – Neuropathologist user study comparing standard H&E and virtual H&E for interpretation. Overall accuracy of assessing tumor cell presence is reported. Group concordance is reported as average pairwise Cohen's Kappa value. Diagnostic confidence is scored from 1 (unsure) to 5 (very confident) and average score is reported.

The responses of the neuropathologists (results summarized in Table 5.1) further validate that the vH&E images and the H&E-stained tissue sectioned images are of similar quality. Both the accuracy and the quality ratings between the two modalities were high, and with no statistically significant differences, suggesting that the virtual staining method produced high-quality discernible images that would be clinically useful for interpretation by neuropathologists. Specifically, the overall accuracy for assessing the presence of tumor cells on the real H&E and vH&E images was 94% and 96%, respectively. The

inter-group concordance using the average pairwise Cohen's Kappa value for recommended continued resection demonstrates a near-perfect level of concordance between the pathologists for both the H&E and virtually stained results (0.74 and 0.81 for the real and virtual H&E, respectively). Finally, the diagnostic confidence was also similar for both types of images (4.6 and 4.7 for the real and virtual H&E, respectively).

This survey supports the effectiveness of qOBM-to-vH&E conversion for clinical applications including intraoperative guidance and more.

5.4 - Discussion

Traditional biopsies require tissue excision, histological processing, and examination by a pathologist, a long process that is challenging to accomplish in a surgical environment; the logistics also affect the feasibility of many other clinical tasks such as cancer screening. For intraoperative surgical applications, rapid pathological assessments have thus far been limited because standard FFPE histology requires time-consuming (overnight or longer) tissue processing, leading to the usage of faster but technically challenging approaches such as frozen sections. Various slide-free and label-free microscopy technologies have been developed to address these problems, but those that do so successfully face significant challenges for in-vivo applications and require complex, bulky and expensive systems to achieve H&E-like images. Here we demonstrate the feasibility of qOBM imaging for rapid assessments, supplementing it with a deep-learning-based framework to obtain H&E-like results from its otherwise clinically unfamiliar grayscale phase-contrast images. To this end, we made use of an unpaired image-to-image translation algorithm known as a CycleGAN to perform a qOBM-to-virtual H&E conversion. We demonstrated this approach with both liver and brain tissue, from three species (mouse, rat and human). The converted images rendered the subcellular and cytoplasmic detail present in the original qOBM image to resemble familiar H&E contrast. The ability of qOBM to provide real-time, label-free, tomographic images of thick tissue specimens with remarkable agreement to traditional H&E histology is feasible because the style/mode difference between qOBM to H&E is relatively minor and facilitates the

use of unpaired image-to-image translation. Additionally, qOBM can be implemented as a handheld probe[37], [39], enabling in-vivo imaging for potential intraoperative, monitoring or screening, as well as other clinical and biomedical applications.

Previous studies have explored the use of CycleGANs for virtual H&E staining with confocal fluorescence[70], MUSE[94], and UV photoacoustic microscopy[29]. Two alternative methods were also compared for MUSE-to-H&E conversion but it was observed that best performance was obtained with CycleGANs[94]. This motivated the use of CycleGANs in our approach. Here we identified several steps that improved CycleGAN performance for qOBM-to-vH&E conversion: First, grayscale inverting the qOBM images was necessary for the success of conversion since nuclei (especially of tumor cells) have higher refractive index and thus show a higher brightness in qOBM images whereas the background is dark, opposite to how such structures appear in standard H&E (Supplementary Note 5.1). Second, transfer learning helped with the performance of human glioma qOBM-to-vH&E conversion (Supplementary Note 5.2). We also found that our models for transforming individual FOVs generalized well to volumetric stacks and stitching large fields of view, which had been a challenge in other image translation pipelines[118]. We evaluated our conversion efforts with a proxy deep learning classification task, observing that a classifier trained on standard H&E performs similarly on vH&E images. Additionally, we validated our model performance with a study involving 5 neuropathologists, who found the virtual H&E images functionally equivalent to the standard H&E images for potential surgical guidance.

Moreover, qOBM enables 3D sectioning with vH&E contrast, overcoming limitations of many current slide-free histology methods. Volumetric imaging can be especially important as it can provide a more comprehensive understanding of a tissue specimen and therefore enables more accurate diagnoses[17]. In fact, in this work we observed that the volumetric imaging capabilities of qOBM can provide critical insight for human specimen that could otherwise be missed with surface level (2D) technologies, even ex vivo. Note that while the deepest vH&E slices we show here is 60 μm from the cut surface, qOBM can achieve a penetration depth of ~120 μm with 720 nm LED illumination (data not

shown). The full depth range of qOBM could potentially be used for vH&E with improvements in signal-to-noise ratio. Moreover, further improvements in the penetration depth of qOBM and hence vH&E can be achieved by using longer wavelengths extending into the near-IR.

Recent work using reflectance confocal microscopy (RCM) and deep learning also showed an ability to provide pseudo-H&E virtual staining[118]. While extremely promising, this approach is not without limitations. In contrast to the case with qOBM, RCM is generally unable to capture the same level of cellular and subcellular details, resulting from inherent differences in the object-frequency-content acquired with each method[116], [117]. Consequently, the RCM to pseudo-H&E pipeline[118] requires a two-step process with "ground truth" pseudo-H&E images constructed from tissues stained with acetic acid and an analytical pseudo-H&E algorithm. The proposed pipeline using qOBM and direct conversion to H&E overcomes these limitations and enables improved histological detail with simpler instrumentation (wide field vs. point scanning, and LED lights sources vs. lasers), while achieving the same penetration depth.

In terms of computational speed, the CycleGAN takes <1 second to acquire and virtually stain a FOV using an NVIDIA A100 GPU. For eventual clinical applications, we expect such a model to be run on more modest computer units where inference time could be longer. However, we believe there are many opportunities for further optimization of the speed of model inference, either through the use of deep learning compilers that speed up the existing model, or compression/distillation approaches[131] that train a smaller, faster model that matches the performance of the original model.

While the qOBM-to-vH&E conversion algorithm serves as a useful visualization tool for clinicians to interpret qOBM images, we envision the usage of qOBM-to-vH&E conversion as part of an AI-based diagnostic and decision support pipeline. Various diagnostic AI systems have been developed for H&E-stained images with high accuracy[132], [133]. In contrast, due to the limited data available for a novel technology like qOBM, it would be challenging to develop diagnostic AI systems from scratch. Instead, the qOBM images can be converted to vH&E and diagnostic pipelines developed for H&E can

then be applied. A proof-of-concept example was demonstrated here by the use of a simple CNN trained on H&E images subsequently applied to the vH&E images (Fig. 5.5). The utilization of qOBM-to-vH&E conversion may allow us to leverage recent advances in computational pathology in new settings, widening the potential of qOBM imaging and slide-free histology.

While our virtual staining results are promising and vH&E images retain diagnostically relevant features, conversion is not pixel-wise perfect. As shown in Supplementary Fig. 5.4, the CycleGAN occasionally has the tendency to hallucinate nuclei, or omit them (Fig. 5.2), primarily around blood vessels. We believe this is due to inherent differences between fresh tissues imaged in qOBM and processed tissues imaged in standard brightfield H&E images, which make the unpaired image-to-image translation difficult in certain scenarios. We note that the main difficulties appear when artifacts are present in the target domain (H&E of fixed tissues) that are not observed in the original domain (qOBM of fresh tissues). However, the model does well when additional features are present in the original domain but missing in the target domain. Future work can examine unpaired image-to-image translation techniques that better ensure the content of the original image is preserved appropriately. However, the underlying challenge limiting conversion efforts is the lack of paired pixel-matched ground truth data. Specifically, the exact same cells and structures cannot be captured by both qOBM and standard brightfield H&E due to the additional tissue processing and sectioning steps involved in the latter. This challenge is what necessitated the use of unpaired image-to-image translation. Therefore, for further improvements and pixel-wise agreement, an alternative approach could be to incorporate a secondary slide-free microscopy technology that provides images similar to H&E in a multimodal system.

Given the lack of pixel-wise ground truth, we validated the virtual H&E brain images by conducting a neuropathologist study, which indicated no significant difference between how board-certified neuropathologists interpret standard brightfield H&E and vH&E images. Future work will focus on imaging in vivo and in real-time, to be evaluated using a handheld probe to collect and virtually stain images.

The proposed technology has the potential to significantly save time, labor and expense, while enabling new capabilities for non-invasive, in-vivo imaging. For analysis of ex-vivo samples, as demonstrated here, an existing digital brightfield microscope can be modified to deliver 3D quantitative phase imaging and vH&E with qOBM for less than $500 USD. No reagents for staining are required, as this is a label-free technology. Further, as we have previously shown[37], [39], qOBM can be configured as a handheld probe or endoscope which could enable novel in-vivo capabilities.

In this study, we specifically focused on the application of brain tumor margin assessment, where real-time, label-free in-vivo histological analysis is gravely needed; however, the proposed workflow enabled by deep learning-based virtual staining of qOBM images could be transformative and widely used to improve cancer screening, detection, treatment guidance, and more.

5.5 - Supplementary Information

5.5.1 – Supplementary Notes

Supplementary Note 5.1: Intensity inversion required for optimal CycleGAN conversion

We found it necessary to invert the grayscale values of the native qOBM images, in order to render the nuclei to appear dark against a lighter background (as they typically appear on H&E). If this step is not taken, the nuclei in qOBM are frequently converted by the CycleGAN into white areas in vH&E (green arrows; Supp Fig. 5.1) while the darker cytoplasmic regions in qOBM are rendered erroneously as nuclei (blue arrows; Supp Fig. 5.1). A similar phenomenon was observed for virtual re-staining of MUSE, another microscopy modality, in Abraham et al.[94]

Supplementary Note 5.2: Effect of model size on CycleGAN performance

We note that CycleGAN model size is an important property that affects conversion quality. Supplementary Figure 5.2 compares the conversions with a small model size/capacity (three layers in the discriminators, nine residual blocks in the generators) and large model size (six layers in the discriminators, twelve residual blocks in the generators) to the conversions of four separate CycleGANs

with a small model capacity trained on images of each of the four observed subtypes. These results indicate that the small model size can capture histological features of individual tissue subtypes but was unable to do so for multiple combined subtypes. Instead, as determined by visual examination, a larger model capacity was necessary to obtain conversions that capture the diversity of histological features seen in the multiple tissue subtypes.

Supplementary Note 5.3: Additional comments on the performance of the classifier developed to differentiate tumors from healthy tissue.

The classifier trained on H&E images from the 9L gliosarcoma tumor model to differentiate tumors from healthy tissue shows excellent accuracy when tested on vH&E images (95.2 ± 2.8%). Nevertheless, it is interesting to note which image types were misclassified. As the confusion matrix of the classifier applied to vH&E images shows (Fig. 5.5B), the misclassified regions are false positives, indicating that the CycleGAN conversion occasionally imparted tumor-like features to healthy images. As shown in Supplementary Figure 5.4, the misclassified regions are primarily a result of the CycleGAN hallucinating dark (hyperchromatic) tumor nuclei around blood vessels in otherwise acellular cortex region (Supp Fig. 5.4A-B) and basal ganglia (Supp Fig. 5.4C-D). Similar to the liver results presented above, this suggest that the network at times struggled to interpret structures around blood vessels which had a different appearance in the fresh tissues compared to the processed tissues. Again, it is likely that such failures can be mitigated with improved training of the qOBM-to-vH&E CycleGAN, using larger datasets or alternatively, unpaired image-to-image translation algorithms.

Supplementary Note 5.4: Generalization of CycleGAN trained on rat to human specimens

To examine the generalization of the qOBM-to-vH&E conversion, we took a neural network trained on rat images and applied it to the qOBM images of human specimens (Supp Fig. 5.5A-B). We observed that nuclear detail remained present, but the CycleGAN had a tendency to render nuclei as red blood cells, inappropriately convert whitespaces, and hallucinate other details (Supp Fig. 5.5C-D). This motivated the use of transfer learning to improve conversion efforts on the human glioma images.

5.5.2 - Supplementary Figures

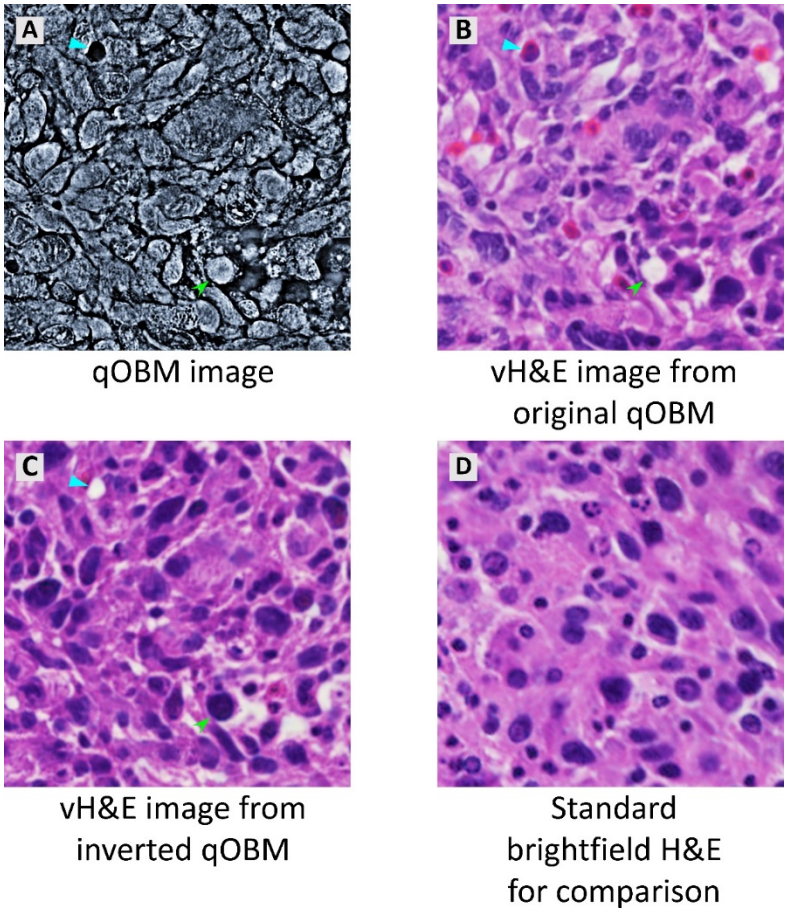

Supplementary Figure 5.1 - qOBM-to-vH&E conversion with original qOBM images. A Label-free 60x qOBM image of a rat brain tumor region with spherical epithelioid cells. **B** vH&E produced by CycleGAN trained with the original qOBM images of the rat brain tumor regions with spherical epithelioid cells. **C** vH&E produced by CycleGAN trained with the contrast-inverted qOBM images of the rat brain tumor regions with spherical epithelioid cells. **D** Standard brightfield H&E image provided for comparison. Arrows highlight specific examples of inaccuracy during conversion.

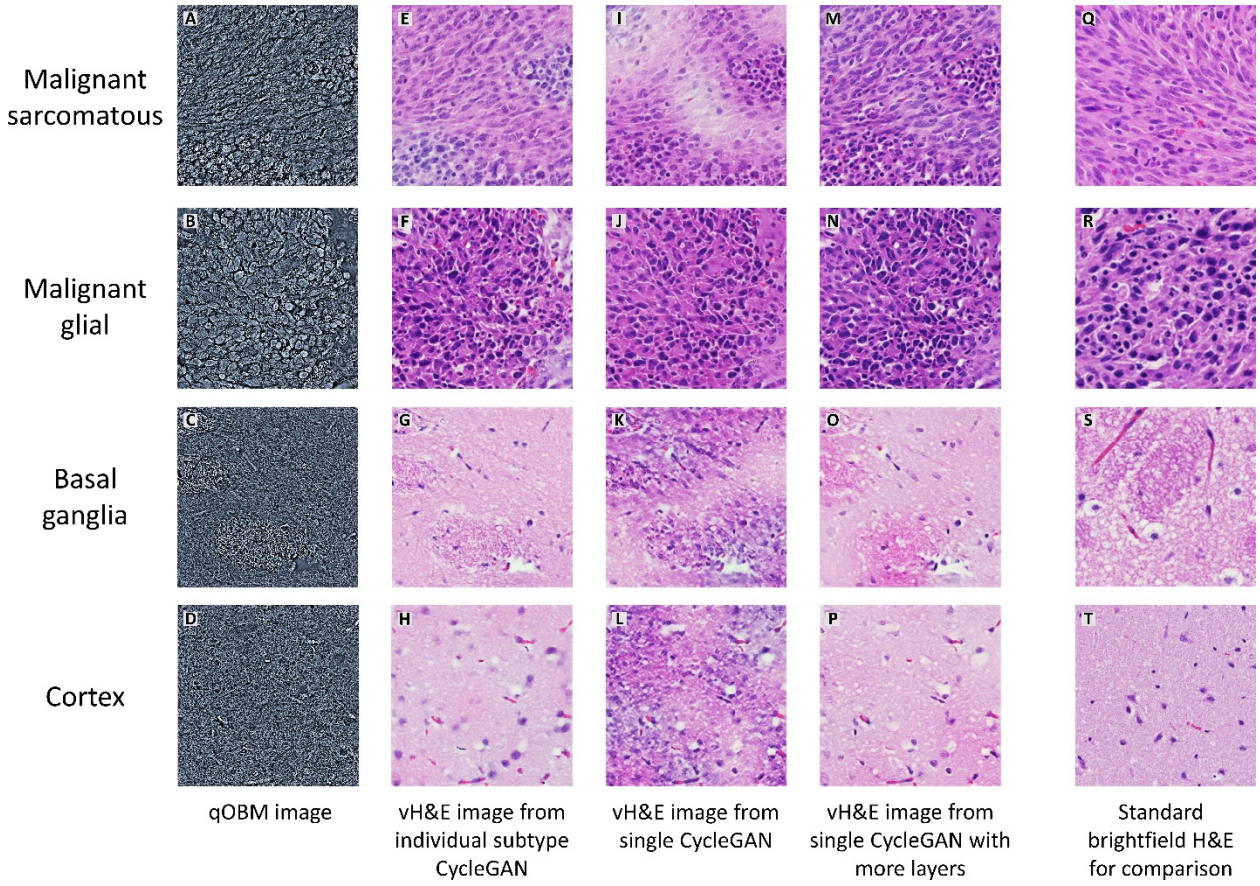

Supplementary Figure 5.2 - qOBM-to-vH&E conversion on brain tissue subtypes using CycleGANs with different training setups. A-D Label-free 60x qOBM images of each of the four rat brain tissue subtypes. **E-H** Corresponding vH&E images produced by separate CycleGANs for each of the four rat brain tissue subtypes. **I-L** Corresponding vH&E images produced by a single CycleGAN trained on all four rat brain tissue subtypes simultaneously. **M-P** Corresponding vH&E images produced by a single CycleGAN with more layers, trained on all four rat brain tissue subtypes simultaneously. **Q-T** Standard brightfield H&E images of the same tissue subtypes, provided for comparison.

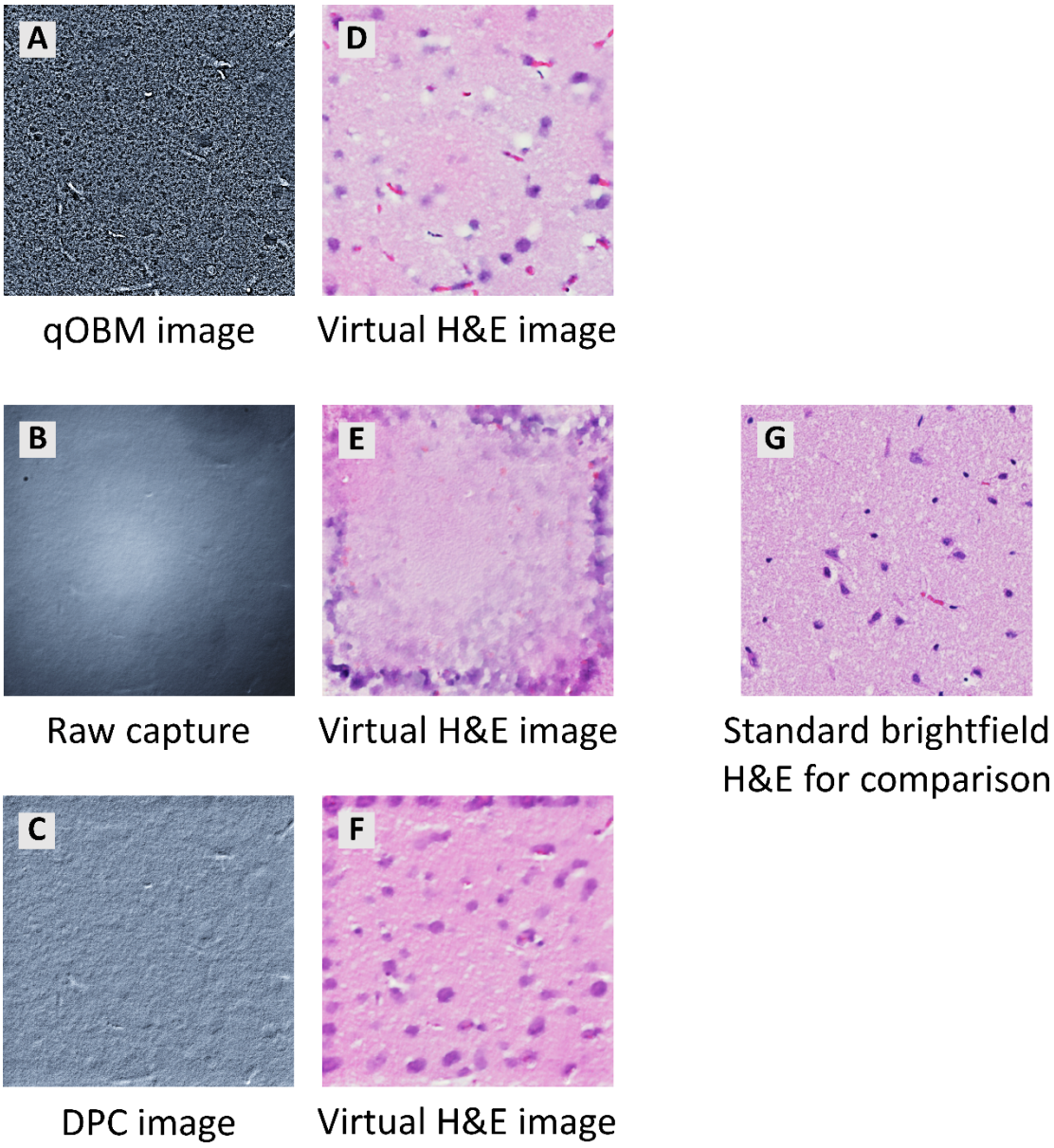

Supplementary Figure 5.3 - Example vH&E conversions by CycleGANs trained on single capture, DPC, and qOBM images. A qOBM image of rat brain cortex. **B** One of the raw captures from the same field of view used to reconstruct the qOBM image. **C** One of the DPC images from the same field of view used to reconstruct the qOBM image. **D** vH&E image produced by a CycleGAN trained on rat brain cortex qOBM and H&E images. **E** vH&E image produced by a CycleGAN trained on rat brain cortex single capture and H&E images. **F** vH&E image produced by a CycleGAN trained on a rat brain cortex DPC and H&E images. **G** Standard brightfield H&E image provided for comparison.

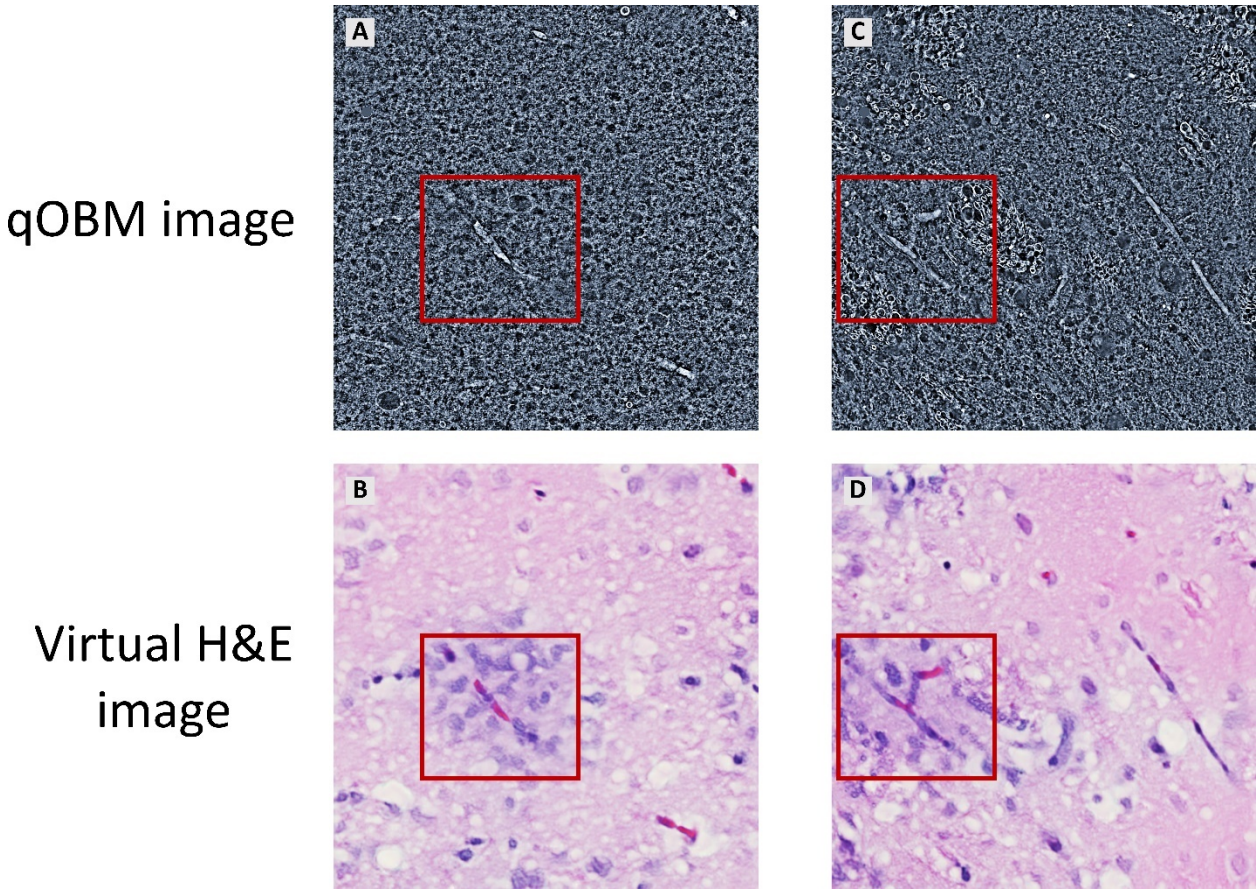

Supplementary Figure 5.4 - Examples of poor qOBM-to-H&E conversions by the CycleGAN trained on rat brain images. A 60x qOBM image of rat cortex. **B** Corresponding vH&E image. **C** 60x qOBM image from rat basal ganglia. **D** Corresponding vH&E image. Red boxes highlight location of significant conversion error. Conversion errors are primarily observed around vessels which are structures that deviate between the qOBM images of fresh tissues and H&E images of processed tissue sections. In qOBM images of fresh tissues, capillaries are better preserved and continuous; in comparison, capillaries appear fragmented in H&E images of processed tissue sections.

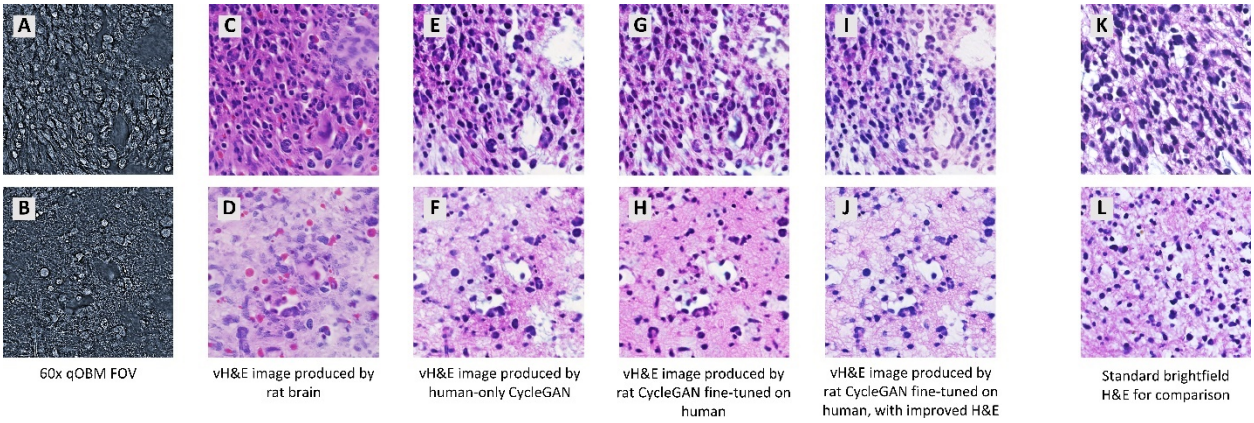

Supplementary Figure 5.5 - qOBM-to-vH&E conversion of human glioma specimens using CycleGANs with different training and dataset setups. **A-B** Label-free 60x qOBM images of human glioma specimens. **C-D** Corresponding vH&E images produced by the CycleGAN trained on only rat brain images. **E-F** Corresponding vH&E images produced by a CycleGAN trained only on human glioma images. **G-H** Corresponding vH&E images produced by a CycleGAN originally trained on rat brain images and further fine-tuned on human glioma images. **I-J** Corresponding vH&E images produced by a CycleGAN originally trained on rat brain images and further fine-tuned on human glioma images, using higher resolution H&E images. **K-L** Standard brightfield H&E images of the same tissue subtypes, provided for comparison.

6. Conclusion

6.1 - Significance

In this dissertation, I explored the use of deep-learning-based virtual H&E staining for MUSE, FIBI, and qOBM microscopy. CycleGAN proved to be a simple yet powerful approach for virtual staining, even when compared to other variants such as DualGAN and GANILLA. The virtual staining approach was evaluated via pathologist user studies, highlighting the effectiveness and potential for clinical utility of this method. The work presented here represents some of the first studies in the literature examining the use of unpaired image-to-image translation frameworks for SFM virtual staining.

6.2 - Data-centric AI and the power of simple frameworks

I show in this dissertation that CycleGANs are a powerful approach for virtual staining of SFM modalities. The CycleGAN framework is a fairly simple framework for unpaired image-to-image translation (and one of the first frameworks for this task), with numerous extensions being developed. Chapter 2 compared CycleGAN to two other similar models and observed the CycleGAN to be the best-performing model. This is in agreement with other recent studies comparing different models for virtual staining and other histopathology tasks [134]–[136].

The success of a simple framework like CycleGAN may be surprising. However, it turns out that the processing and curation of the dataset plays a very important role in the quality of the conversions, and with appropriately clean and well-processed datasets, simple models like CycleGANs can perform quite well. For example, training CycleGANs on native MUSE and qOBM images originally fails, while inverting the intensities of the image, and thereby aligning the dark/light ratios of nuclei and cytoplasm between the SFM and H&E modes, enables successful conversion. Another consideration is to ensure the size of nuclei match between the SFM images and H&E images (which is done by resizing the H&E images). If the scale of the features in the images do not match, conversion efforts fail. Additionally, significant effort was put into the curation of the qOBM training dataset, such as omitting out-of-focus

regions and ensuring that similar histologic features were well-represented in both the qOBM and H&E sets. Model development underwent an iterative process in which errors by one iteration of the qOBM-to-H&E model informed the collection and curation of the next version of the training dataset.

This importance of data preprocessing and curation aligns well with the paradigm of data-centric AI. Data-centric AI is a recent concept that emphasizes the systematic engineering of data to build AI systems, shifting the focus from model development to data engineering [137]. This dissertation indicates the importance of data-centric AI in the context of microscopy modality conversion.

6.3 - Limitations and future directions

Here, I describe some of the limitations of the current methodologies. Additionally, I discuss future directions to improve the quality of microscopy modality conversion and validate such algorithms for clinical use-cases.

6.3.1 - Hallucinations of CycleGANs

While CycleGANs have been demonstrated to be quite powerful, they are not without issues. For instance, it is frequently observed that a CycleGAN trained on biased datasets can add spurious features or remove critical features in medical images: CycleGANs can “cause” or “cure” cancer [138]. This is since the model is replicating the distribution of the target domain (as incentivized by the discriminator), and if the datasets are biased, then the CycleGAN will convert in a biased manner. We observe occasional hallucinations as well, but by ensuring the datasets are preprocessed appropriately and curated well, the likelihood of disastrous hallucinations decreases. That said, certain minor hallucinations are acceptable or even desirable. As highlighted in Figure 3.4, certain features in the vH&E images generated from FIBI are not explicitly present in the original FIBI image. However, it nevertheless improves the clarity of the image due to the improved similarity to standard H&E. Another example is demonstrated in Figure 5.8D-F, where the vH&E images do not contain the radiation artifacts seen in qOBM. Therefore, it is important to be cautious of overly focusing on content preservation and removing all hallucinations.

6.3.2 - Alternative unpaired image-to-image translation approaches

While CycleGANs served as a very promising algorithm for unpaired virtual staining, there are several alternative algorithms for unpaired image-to-image translation that could be explored. Some alternative frameworks include: UNIT [139], U-GAT-IT [140], DistanceGAN [141], HarmonicGAN [142], L-CycleGAN [143], and SPA-GAN [144]. All of these models are based on a GAN framework but have different model architectures or loss functions to either improve style transfer or the content preservation of the model.

Another particularly promising method for unpaired image-to-image translation is contrastive unpaired translation (CUT) [145]. It utilizes a "contrastive objective" that looks at patches in the input and output image and tries to keep the features of nearby patches similar while features of more distant patches are incentivized to be dissimilar. MUSE-to-H&E conversion on a dataset of skeletal muscle tissue images with CUT was attempted, but results were disappointing (Figure 6.1). CycleGAN managed to maintain the structure of the skeletal muscle and the location of the nuclei, while CUT did not (the muscle bundles in the CUT version align poorly with actual structure in the MUSE original and replicated well in the CycleGAN version. One potential explanation is because muscle tissue is fairly homogenous, distant patches do indeed resemble local features, and thus the CUT algorithm approach is poorly suited to this specimen.

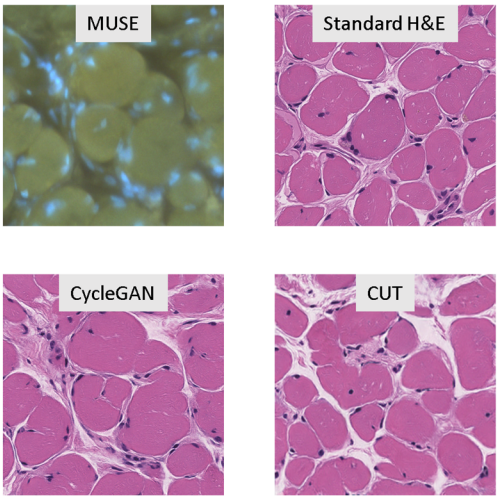

Figure 6.1 - Comparison of CycleGAN and CUT for MUSE-to-H&E conversion. Shown is a MUSE image of skeletal muscle, a corresponding standard H&E, and conversions by the CycleGAN and CUT models trained on a dataset of similar images.

Ozyoruk et al. developed a variant of CUT for converting images of frozen-section slides into FFPE-like images [71]. It is likely that utilizing such variants specifically designed for histopathological applications may achieve better results and should be investigated further.

Recently, a variety of loss-function regularization terms have been described that may be able to help ensure content preservation, especially in the context of medical imaging and microscopy. In Li et al. [85], the authors demonstrated the addition of a saliency constraint to CycleGANs for various microscopy image transformation tasks, such as immunofluorescence-to-H&E conversion. The saliency loss term is defined by minimizing the difference between the threshold-based segmentation masks of the original SFM and virtual H&E image:

$$\mathcal{L}_{saliency}(G_X, G_Y) = \mathbb{E}_{x\sim p_{data}(x)}\left[\left\|T_\alpha(x) - T_\beta\left(G_X(x)\right)\right\|_1\right] + \mathbb{E}_{y\sim p_{data}(y)}\left[\left\|T_\beta(y) - T_\alpha\left(G_Y(y)\right)\right\|_1\right]$$

where x is the SFM image, $G_X(x)$ is conversion to vH&E, y is the real H&E image, $G_Y(y)$ is conversion to fake SFM, T_α and T_β are segmentation functions parameterized by thresholds α and β, and $\|\cdot\|_1$ represent an L_1-norm. It requires manual tuning of separate threshold values for images from the separate domains. Additionally, the paper demonstrates successful results mainly with images that are fairly sparse

in content, with a clear background and foreground, which is not necessarily true for many SFM images. Nevertheless, it is a worthwhile future direction.

A recent approach is to use self-regularization, where the input and output of a generator network are constrained to be the same. For example, [146] utilized self-regularization for training a network to convert medical endoscopy images into synthetic endoscopy data for domain adaptation applications. Additionally, self-regularization has been applied to unpaired image-to-image translation with promising results [147]. It may be beneficial to incorporate self-regulation into the CycleGAN training objective by directly minimizing the difference between the input SFM image and the output virtual H&E image:

$$\mathcal{L}_{self}(G_X, G_Y) = \mathbb{E}_{x\sim p_{data}(x)}[\|G_X(x) - x\|_1] + \mathbb{E}_{y\sim p_{data}(y)}[\|G_Y(y) - y\|_1]$$

In the field of image generation, diffusion models have become extremely successful and popular, beating GANs at several tasks [148], [149]. Despite their popularity, there has been limited exploration of diffusion models for unpaired image-to-image translation.

Dual Diffusion Implicit Bridge (DDIB) [150] exploits the shared latent representation of any diffusion model. This means that separate diffusion models are trained to generate images for the two domains (SFM and H&E, for example), and an unpaired image-to-image translation model is obtained for free. Preliminary results for MUSE-to-H&E conversion with DDIB based on a latent diffusion model [151] indicated that the H&E style is produced well in the converted images, but content is not always appropriately maintained, resulting in missing or inaccurately-shaped nuclei (Figure 6.2). Future work should more thoroughly examine the use of DDIB for virtual staining, including the incorporation of additional constraints to improve content preservation.

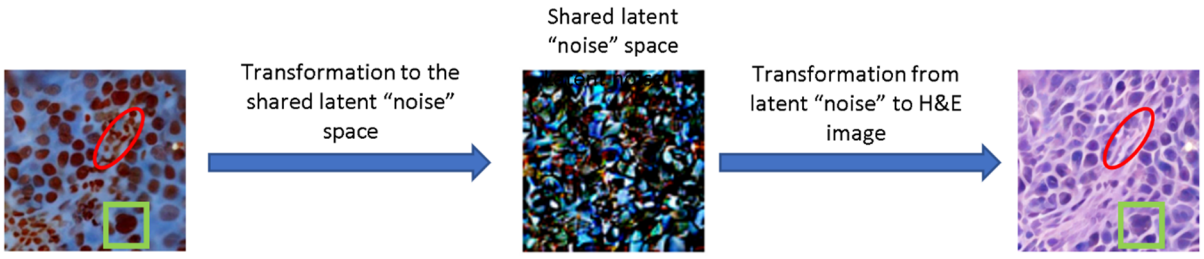

Figure 6.2- Preliminary results exploring the use of DDIB for MUSE-to-H&E conversion (urothelial cell carcinoma dataset as explored in Chapter 2). The MUSE image is transformed into a shared latent "noise" space before being transformed into an H&E image with a latent diffusion model. Overall H&E style is replicated, and some aspects of content is maintained (green box), while other aspects of the original image are not preserved (red oval). Inverted MUSE image shown for improved clarity of nuclei.

6.3.3 - Alternative imaging strategies to collect paired datasets

While this dissertation explored the use of unpaired image-to-image translation for virtual staining of SFM to overcome an absence of accessible paired data, in some cases it may be possible to collect paired data for SFM via alternative imaging approaches.

For example, Borhani et al. [38] demonstrates techniques for deploying deep learning for mapping label-free MPM to H&E-stained brightfield images. In this study, paired image data can be collected, as MPM can be used to image stained slides. This study was unusual as it did not use GANs for virtual H&E staining.

Another paper investigated virtual staining of RCM by generating paired image datasets to aid their efforts [118]. Specifically, skin tissue was stained with acetic acid to enhance nuclear contrast in the RCM images. Then, pseudo-H&E ground truth images were constructed via an analytical approach based on Beer-Lambert Law. Their pipeline therefore requires two steps: conversion with a GAN-based framework to acetic acid-stained images, followed by conversion to pseudo-H&E with another GAN. Additionally, Li et al. utilized a specialized neural network architecture that took in a stack of 7 images and output a pseudo-H&E conversion for the central plane. Note that true H&E images are not used at all to train the virtual staining network, since obtaining the paired H&E image was not possible.

In the context of the SFMs studied in this dissertation, Niemeier et al. explored the development of sequential staining techniques in order to acquire MUSE-H&E pairs [152]. Further research in this direction could result in better virtual staining of MUSE images.

There are several potential approaches for improving qOBM-to-H&E conversion quality. Note that both qOBM and QPI both provide quantitative phase information, with the former being applied for thick samples, and the latter for thin slides. It therefore may be possible to utilize QPI virtual staining models that are trained with pixel-matched data [68]. However, differences between QPI of FFPE thin sections and qOBM of fresh unprocessed thick samples may hinder the transfer of QPI-to-H&E models to qOBM-to-H&E. An alternative approach is to utilize an additional slide-free microscopy system that provides H&E-like images to serve as ground truth. FIBI images already closely resemble H&E. It can be envisaged that a single microscope system images a thick specimen simultaneously with qOBM and FIBI. This would allow for the development of a qOBM-to-FIBI algorithm using more robust paired approaches. Again, while the contrasts associated with FIBI images are similar to H&E, unpaired translation into virtual H&E may provide additional benefit. Then, the FIBI vH&E images can be used to train a qOBM-to-vH&E model using paired methods. As described in Chapter 3, we have seen very promising results with FIBI-to-H&E conversion, more so than with unpaired qOBM-to-H&E conversion since the FIBI and H&E domains are much more similar, resulting in a much easier translation task that can be solved satisfactorily with unpaired translation techniques.

Finally, it is worth pointing out that generated vH&E images form a pair with the original image SFM image, albeit a semi-accurate pair. It may be possible that training a standard image-to-image translation method (like with pix2pix) on a carefully filtered and curated subset of (SFM, CycleGAN-generated vH&E) pairs may result in a better-performing, more robust neural network for virtual staining.

6.3.4 - Virtual staining evaluation

As described in the Chapter 1.7.4, evaluation of SFM virtual staining is challenging due to the lack of pixel-matched ground truth. Style transfer metrics and content preservation metrics, along with

pathologist case studies are all complementary forms of evaluation. Most reports utilize style transfer metrics, and some use pathologist user studies, while very few utilize content preservation metrics. This dissertation was similar: MUSE-to-H&E was evaluated with a two-sample classifier test, FIBI-to-H&E was evaluated with a pathologist user study, and qOBM-to-H&E was evaluated with both a neural network classifier and a pathologist user study. Future work should therefore focus on more comprehensively evaluating content preservation (without overstating the importance of this, as discussed in Chapter 6.3.1).

An alternative approach for measuring content preservation rarely seen in the literature is to generate nuclear instance segmentation masks and tissue class masks for the SFM images and virtually stained image that can subsequently be compared. Hand-labeling of nuclei will likely be needed for SFM images, but this can be accelerated by computer vision methodologies such as using a thresholding algorithm or training pixel classifiers to label the nuclei. A pretrained nuclear segmentation model can be applied to the virtually stained images to extract the nuclei segmentation mask, which can be further refined after manual inspection. After generating nuclear segmentation masks for SFM images and the conversions, we can directly compare using common segmentation metrics such as Dice coefficient [153]. A similar analysis can be done with tissue components. For example, for skin images, we can label the epithelium, connective tissue, and muscle layers in both the SFM and converted images and also compare with Dice coefficient. The labels in the SFM and virtually stained images can be generated with pixel-level classifiers that are trained on annotations and subsequently reviewed and refined manually.

A major concern regarding the application of deep learning models for medical purposes is the generalizability and robustness of the models. Chapter 3 studied this in the context of qOBM-to-H&E conversion, where it was observed that the CycleGAN trained on rat brain tissue images generalized to previously unseen mixed tumor/healthy examples. Additionally, it was observed that the CycleGAN trained on human glioma tissue generalized to an image of healthy human brain tissue. However, these experiments are by no means comprehensive. In future work, the generalizability and robustness of SFM

virtual staining methods could be more systematically analyzed. For example, models could be trained on normal skin, colon, breast, and brain specimens and apply the trained model to samples with basal cell carcinoma, squamous cell carcinoma, invasive ductal carcinoma, glioblastoma, and low-grade gliomas. The opposite route could be tested as well. Then, training could be performed with mixed datasets such as training normal skin+basal cell carcinoma and testing on normal skin images. Doing so will allow us to analyze how the balance between normal and cancerous images in the training set affects the final conversion. Additionally, it would be desirable to train models with data from multiple cancer types or even organs. Such experiments will help us better understand the strengths and limitations of unpaired image-to-image translation frameworks when applied to SFM-to-H&E conversion.

Finally, the pathologist studies described throughout this dissertation, while promising, were comprised of a limited number of specimens and pathologists. To definitively establish clinical utility, a more comprehensive pathologist evaluation will be needed.

6.3.5 - Incorporating the unique details provided by SFM

Some SFM methods provide additional information about the tissue (Section 3.3.7 describes some examples of extra detail provided by FIBI) that may be lost in the microscopy modality conversion process. This loss of information is acceptable since it allows for better replication of the stain style that may be more familiar to pathologists, but it would be desirable if there were also approaches that can selectively maintain some of the additional information from the original SFM image. Certain unique features in the SFM images could be segmented and masked out during conversion in order to remain unchanged in the final image. Another approach could be to convert the SFM images to alternative stains that pathologists may be familiar with, such as Masson's Trichome. All the studies in this dissertation focus on virtual H&E staining, but the same approach should function well for other stains. Alternatively, a simple overlay of a vH&E and original FIBI image may also suffice (Figure 6.3) and could serve as a target for another neural network to learn directly from. There are many potential directions for

developing novel approaches that take the best features of both the SFM images and virtually stained images for superior histological visualization.

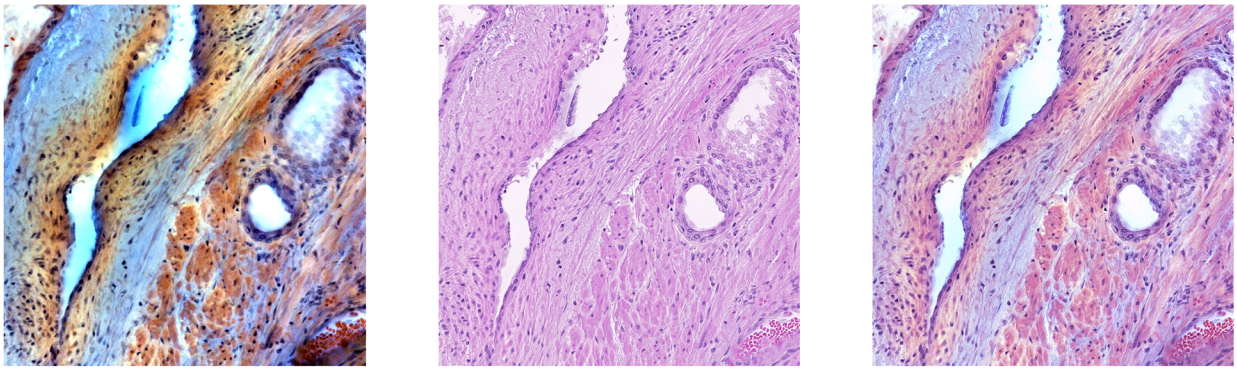

Figure 6.3 - A simple overlay of the FIBI image on top of its virtual H&E conversion may provide improved contrasts and visualization. This is a FIBI image of fixed human prostatic adenocarcinoma tissue, and it's overlayed on top of the virtual H&E image with 40% opacity.

6.3.6 - Diagnostic AI with slide-free microscopy, enabled by virtual staining

In this dissertation, virtual staining was developed with the goal of improving the ease of interpretation of SFM methods by pathologists. However, the availability of trained expert pathologists to provide diagnoses in some scenarios such as intraoperative consultation can be especially difficult in fields with growing shortages in pathology expertise, such as neuropathology [154]. Therefore, another research direction for improving the interpretation of SFM images is to automatically provide diagnoses via AI. As briefly discussed in Chapter 1, various diagnostic AI systems have been developed for stained brightfield images (especially H&E-stained) with high accuracy [132], [133]. In contrast, due to the limited data available for a novel SFM technology, it would be challenging to develop diagnostic AI systems from scratch. However, SFM virtual staining could be utilized to provide virtually stained images that can be entered into previously developed diagnostic pipelines. A preliminary proof-of-concept example was given in Chapter 5 using a simple CNN trained on H&E images subsequently applied to the vH&E images generated from qOBM. Furthermore, obtaining accurate predictions from diagnostic pipelines applied to virtually stained images should be treated as a desirable goal and this can be utilized as a metric

for virtual staining performance (Section 1.7.4). To emphasize, the output of virtual staining algorithms is not just viewed by pathologists, but other AI systems for computational pathology. This approach to developing and applying SFM virtual staining methods could enable novel applications of computational pathology in previously unexplored settings.

References

[1] J. D. Bancroft and M. Gamble, *Theory and Practice of Histological Techniques*, Sixth Edition. Edinburgh: Churchill Livingstone, 2008. doi: https://doi.org/10.1016/B978-0-443-10279-0.50001-4.

[2] Y. Liu, R. M. Levenson, and M. W. Jenkins, "Slide Over: Advances in Slide-Free Optical Microscopy as Drivers of Diagnostic Pathology," *The American Journal of Pathology*, vol. 192, no. 2, pp. 180–194, Feb. 2022, doi: 10.1016/j.ajpath.2021.10.010.

[3] N. Sanai, M.-Y. Polley, M. W. McDermott, A. T. Parsa, and M. S. Berger, "An extent of resection threshold for newly diagnosed glioblastomas," *J Neurosurg*, vol. 115, no. 1, pp. 3–8, Jul. 2011, doi: 10.3171/2011.2.jns10998.

[4] N. Sanai and M. S. Berger, "Glioma extent of resection and its impact on patient outcome," *Neurosurgery*, vol. 62, no. 4, pp. 753–764; discussion 264-266, Apr. 2008, doi: 10.1227/01.neu.0000318159.21731.cf.

[5] V. Rastogi, N. Puri, S. Arora, G. Kaur, L. Yadav, and R. Sharma, "Artefacts: a diagnostic dilemma - a review," *J Clin Diagn Res*, vol. 7, no. 10, pp. 2408–2413, Oct. 2013, doi: 10.7860/JCDR/2013/6170.3541.

[6] C. Schulz, S. Waldeck, and U. M. Mauer, "Intraoperative Image Guidance in Neurosurgery: Development, Current Indications, and Future Trends," *Radiology Research and Practice*, vol. 2012, p. e197364, May 2012, doi: 10.1155/2012/197364.

[7] A. Moiyadi, P. Syed, S. Srivastava, P. Syed, and S. Srivastava, "Fluorescence-guided surgery of malignant gliomas based on 5-aminolevulinic acid: paradigm shifts but not a panacea," *Nature Reviews Cancer*, vol. 14, no. 2, Art. no. 2, Feb. 2014, doi: 10.1038/nrc3566-c1.

[8] B. E. Schaafsma *et al.*, "The clinical use of indocyanine green as a near-infrared fluorescent contrast agent for image-guided oncologic surgery," *J Surg Oncol*, vol. 104, no. 3, pp. 323–332, Sep. 2011, doi: 10.1002/jso.21943.

[9] C. Wu *et al.*, "In-vivo optical imaging in head and neck oncology: basic principles, clinical applications and future directions," *International Journal of Oral Science*, vol. 10, no. 2, Art. no. 2, Mar. 2018, doi: 10.1038/s41368-018-0011-4.

[10] D. A. Orringer and S. Camelo-Piragua, "Fast and slide-free imaging," *Nat Biomed Eng*, vol. 1, no. 12, Art. no. 12, Dec. 2017, doi: 10.1038/s41551-017-0172-z.

[11] S. Krishnamurthy, J. Q. Brown, N. Iftimia, R. M. Levenson, and M. Rajadhyaksha, "Ex Vivo Microscopy," *Arch Pathol Lab Med*, vol. 143, no. 9, pp. 1058–1068, Sep. 2019, doi: 10.5858/arpa.2019-0058-RA.

[12] M. Rajadhyaksha, G. Menaker, T. Flotte, P. J. Dwyer, and S. González, "Confocal Examination of Nonmelanoma Cancers in Thick Skin Excisions to Potentially Guide Mohs Micrographic Surgery Without Frozen Histopathology," *Journal of Investigative Dermatology*, vol. 117, no. 5, pp. 1137–1143, Nov. 2001, doi: 10.1046/j.0022-202x.2001.01524.x.

[13] M. Rajadhyaksha, A. Marghoob, A. Rossi, A. C. Halpern, and K. S. Nehal, "Reflectance confocal microscopy of skin in vivo: From bench to bedside," *Lasers Surg Med*, vol. 49, no. 1, pp. 7–19, Jan. 2017, doi: 10.1002/lsm.22600.

[14] M. Ragazzi *et al.*, "Fluorescence confocal microscopy for pathologists," *Mod Pathol*, vol. 27, no. 3, pp. 460–471, Mar. 2014, doi: 10.1038/modpathol.2013.158.

[15] J. Mertz, "Optical sectioning microscopy with planar or structured illumination," *Nat Methods*, vol. 8, no. 10, Art. no. 10, Oct. 2011, doi: 10.1038/nmeth.1709.

[16] M. Wang *et al.*, "High-Resolution Rapid Diagnostic Imaging of Whole Prostate Biopsies Using Video-Rate Fluorescence Structured Illumination Microscopy," *Cancer Res*, vol. 75, no. 19, pp. 4032–4041, Oct. 2015, doi: 10.1158/0008-5472.CAN-14-3806.

[17] J. T. C. Liu *et al.*, "Harnessing non-destructive 3D pathology," *Nat Biomed Eng*, vol. 5, no. 3, Art. no. 3, Mar. 2021, doi: 10.1038/s41551-020-00681-x.

[18] I. Costantini, R. Cicchi, L. Silvestri, F. Vanzi, and F. S. Pavone, “In-vivo and ex-vivo optical clearing methods for biological tissues: review,” *Biomed. Opt. Express, BOE*, vol. 10, no. 10, pp. 5251–5267, Oct. 2019, doi: 10.1364/BOE.10.005251.
[19] J. Huisken, J. Swoger, F. Del Bene, J. Wittbrodt, and E. H. K. Stelzer, “Optical Sectioning Deep Inside Live Embryos by Selective Plane Illumination Microscopy,” *Science*, vol. 305, no. 5686, pp. 1007–1009, Aug. 2004, doi: 10.1126/science.1100035.
[20] A. K. Glaser *et al.*, “Light-sheet microscopy for slide-free non-destructive pathology of large clinical specimens,” *Nature Biomedical Engineering*, vol. 1, no. 7, Art. no. 7, Jun. 2017, doi: 10.1038/s41551-017-0084.
[21] A. K. Glaser *et al.*, “Multi-immersion open-top light-sheet microscope for high-throughput imaging of cleared tissues,” *Nature Communications*, vol. 10, no. 1, Art. no. 1, Jul. 2019, doi: 10.1038/s41467-019-10534-0.
[22] Y. K. Tao *et al.*, “Assessment of breast pathologies using nonlinear microscopy,” *PNAS*, vol. 111, no. 43, pp. 15304–15309, Oct. 2014, doi: 10.1073/pnas.1416955111.
[23] N. V. Kuzmin *et al.*, “Third harmonic generation imaging for fast, label-free pathology of human brain tumors,” *Biomed. Opt. Express, BOE*, vol. 7, no. 5, pp. 1889–1904, May 2016, doi: 10.1364/BOE.7.001889.
[24] L. M. G. van Huizen *et al.*, “Compact portable multiphoton microscopy reveals histopathological hallmarks of unprocessed lung tumor tissue in real time,” *Translational Biophotonics*, vol. 2, no. 4, p. e202000009, 2020, doi: 10.1002/tbio.202000009.
[25] T. Matsui *et al.*, “Non-labeling multiphoton excitation microscopy as a novel diagnostic tool for discriminating normal tissue and colorectal cancer lesions,” *Sci Rep*, vol. 7, no. 1, Art. no. 1, Jul. 2017, doi: 10.1038/s41598-017-07244-2.
[26] L. V. Wang, “Multiscale photoacoustic microscopy and computed tomography,” *Nature Photon*, vol. 3, no. 9, Art. no. 9, Sep. 2009, doi: 10.1038/nphoton.2009.157.
[27] L. V. Wang and S. Hu, “Photoacoustic Tomography: In Vivo Imaging from Organelles to Organs,” *Science*, vol. 335, no. 6075, pp. 1458–1462, Mar. 2012, doi: 10.1126/science.1216210.
[28] T. T. W. Wong *et al.*, “Fast label-free multilayered histology-like imaging of human breast cancer by photoacoustic microscopy,” *Science Advances*, vol. 3, no. 5, p. e1602168, May 2017, doi: 10.1126/sciadv.1602168.
[29] R. Cao *et al.*, “Label-free intraoperative histology of bone tissue via deep-learning-assisted ultraviolet photoacoustic microscopy,” *Nat. Biomed. Eng*, vol. 7, no. 2, Art. no. 2, Feb. 2023, doi: 10.1038/s41551-022-00940-z.
[30] F. Fereidouni *et al.*, “Microscopy with ultraviolet surface excitation for rapid slide-free histology,” *Nature Biomedical Engineering*, vol. 1, no. 12, Art. no. 12, Dec. 2017, doi: 10.1038/s41551-017-0165-y.
[31] A. Qorbani *et al.*, “Microscopy with ultraviolet surface excitation (MUSE): A novel approach to real-time inexpensive slide-free dermatopathology,” *Journal of Cutaneous Pathology*, vol. 45, no. 7, pp. 498–503, 2018, doi: 10.1111/cup.13255.
[32] Y. Liu, A. M. Rollins, R. M. Levenson, F. Fereidouni, and M. W. Jenkins, “Pocket MUSE: an affordable, versatile and high-performance fluorescence microscope using a smartphone,” *Commun Biol*, vol. 4, no. 1, Art. no. 1, Mar. 2021, doi: 10.1038/s42003-021-01860-5.
[33] T. Yoshitake *et al.*, “Rapid histopathological imaging of skin and breast cancer surgical specimens using immersion microscopy with ultraviolet surface excitation,” *Scientific Reports*, vol. 8, no. 1, Art. no. 1, Mar. 2018, doi: 10.1038/s41598-018-22264-2.
[34] A. D. Borowsky *et al.*, “A Pilot Validation Study Comparing FIBI, a Slide-Free Imaging Method, with Standard FFPE H&E Tissue Section Histology for Primary Surgical Pathology Diagnosis.” medRxiv, p. 2022.03.10.22272226, Mar. 13, 2022. doi: 10.1101/2022.03.10.22272226.
[35] P. Ledwig and F. E. Robles, “Epi-mode tomographic quantitative phase imaging in thick scattering samples,” *Biomed. Opt. Express, BOE*, vol. 10, no. 7, pp. 3605–3621, Jul. 2019, doi: 10.1364/BOE.10.003605.

[36] P. Ledwig and F. E. Robles, "Quantitative 3D refractive index tomography of opaque samples in epi-mode," *Optica, OPTICA*, vol. 8, no. 1, pp. 6–14, Jan. 2021, doi: 10.1364/OPTICA.410135.
[37] P. C. Costa *et al.*, "Towards in-vivo label-free detection of brain tumor margins with epi-illumination tomographic quantitative phase imaging," *Biomed. Opt. Express, BOE*, vol. 12, no. 3, pp. 1621–1634, Mar. 2021, doi: 10.1364/BOE.416731.
[38] Z. Guang, P. C. Costa, A. Jacobs, C. Filan, and F. E. Robles, "Handheld quantitative phase imaging probe for in-vivo brain tumor margin assessment," in *Label-free Biomedical Imaging and Sensing (LBIS) 2023*, SPIE, Mar. 2023, pp. 69–71. doi: 10.1117/12.2650851.
[39] Z. Guang, P. Ledwig, P. C. Costa, C. Filan, and F. E. Robles, "Optimization of a flexible fiber-optic probe for epi-mode quantitative phase imaging," *Opt. Express, OE*, vol. 30, no. 11, pp. 17713–17729, May 2022, doi: 10.1364/OE.454997.
[40] C. E. Filan, H. Song, M. Platt, and F. E. Robles, "Quantitative phase imaging of sickle cell disease effects on mouse brain vasculature using quantitative oblique back-illumination microscopy," in *Quantitative Phase Imaging IX*, SPIE, Mar. 2023, pp. 77–83. doi: 10.1117/12.2648496.
[41] C. E. Filan, S. Charles, P. C. Costa, B. Cheng, H. Lu, and F. E. Robles, "Tracking early tuberous sclerosis complex diseased organoid development with quantitative oblique back-illumination microscopy," in *Imaging, Manipulation, and Analysis of Biomolecules, Cells, and Tissues XXI*, SPIE, Mar. 2023, pp. 83–90. doi: 10.1117/12.2650755.
[42] I. Goodfellow, Y. Bengio, and A. Courville, *Deep learning*. in Adaptive Computation and Machine Learning. The MIT Press, 2016.
[43] J. Howard and S. Gugger, *Deep Learning for Coders with fastai and PyTorch*. O'Reilly Media, Inc., 2020.
[44] S. Ruder, "An overview of gradient descent optimization algorithms." arXiv, Jun. 15, 2017. Accessed: Apr. 26, 2023. [Online]. Available: http://arxiv.org/abs/1609.04747
[45] O. Russakovsky *et al.*, "ImageNet Large Scale Visual Recognition Challenge," *Int J Comput Vis*, vol. 115, no. 3, pp. 211–252, Dec. 2015, doi: 10.1007/s11263-015-0816-y.
[46] D. Cireşan, U. Meier, J. Masci, and J. Schmidhuber, "Multi-column deep neural network for traffic sign classification," *Neural Networks*, vol. 32, pp. 333–338, Aug. 2012, doi: 10.1016/j.neunet.2012.02.023.
[47] A. Krizhevsky, I. Sutskever, and G. E. Hinton, "ImageNet Classification with Deep Convolutional Neural Networks," in *Advances in Neural Information Processing Systems 25*, F. Pereira, C. J. C. Burges, L. Bottou, and K. Q. Weinberger, Eds., Curran Associates, Inc., 2012, pp. 1097–1105. Accessed: Jan. 13, 2020. [Online]. Available: http://papers.nips.cc/paper/4824-imagenet-classification-with-deep-convolutional-neural-networks.pdf
[48] K. Simonyan and A. Zisserman, "Very Deep Convolutional Networks for Large-Scale Image Recognition," *arXiv:1409.1556 [cs]*, Apr. 2015, Accessed: Jan. 15, 2020. [Online]. Available: http://arxiv.org/abs/1409.1556
[49] K. He, X. Zhang, S. Ren, and J. Sun, "Deep Residual Learning for Image Recognition," in *2016 IEEE Conference on Computer Vision and Pattern Recognition (CVPR)*, Jun. 2016, pp. 770–778. doi: 10.1109/CVPR.2016.90.
[50] C. Szegedy *et al.*, "Going Deeper with Convolutions," *arXiv:1409.4842 [cs]*, Sep. 2014, Accessed: Apr. 07, 2021. [Online]. Available: http://arxiv.org/abs/1409.4842
[51] W. Bulten *et al.*, "Artificial intelligence assistance significantly improves Gleason grading of prostate biopsies by pathologists," *Mod Pathol*, vol. 34, no. 3, pp. 660–671, Mar. 2021, doi: 10.1038/s41379-020-0640-y.
[52] K. Nagpal *et al.*, "Development and validation of a deep learning algorithm for improving Gleason scoring of prostate cancer," *npj Digital Medicine*, vol. 2, no. 1, Art. no. 1, Jun. 2019, doi: 10.1038/s41746-019-0112-2.
[53] K. S. Wang *et al.*, "Accurate diagnosis of colorectal cancer based on histopathology images using artificial intelligence," *BMC Medicine*, vol. 19, no. 1, p. 76, Mar. 2021, doi: 10.1186/s12916-021-01942-5.

[54] M. N. Gurcan, L. E. Boucheron, A. Can, A. Madabhushi, N. M. Rajpoot, and B. Yener, "Histopathological Image Analysis: A Review," *IEEE Reviews in Biomedical Engineering*, vol. 2, pp. 147–171, 2009, doi: 10.1109/RBME.2009.2034865.
[55] J. Yosinski, J. Clune, Y. Bengio, and H. Lipson, "How transferable are features in deep neural networks?," in *Advances in Neural Information Processing Systems 27*, Z. Ghahramani, M. Welling, C. Cortes, N. D. Lawrence, and K. Q. Weinberger, Eds., Curran Associates, Inc., 2014, pp. 3320–3328. Accessed: Jan. 15, 2020. [Online]. Available: http://papers.nips.cc/paper/5347-how-transferable-are-features-in-deep-neural-networks.pdf
[56] J. Long, E. Shelhamer, and T. Darrell, "Fully convolutional networks for semantic segmentation," in *2015 IEEE Conference on Computer Vision and Pattern Recognition (CVPR)*, Jun. 2015, pp. 3431–3440. doi: 10.1109/CVPR.2015.7298965.
[57] K. He, G. Gkioxari, P. Dollár, and R. Girshick, "Mask R-CNN," in *2017 IEEE International Conference on Computer Vision (ICCV)*, Oct. 2017, pp. 2980–2988. doi: 10.1109/ICCV.2017.322.
[58] O. Ronneberger, P. Fischer, and T. Brox, "U-Net: Convolutional Networks for Biomedical Image Segmentation," in *Medical Image Computing and Computer-Assisted Intervention – MICCAI 2015*, N. Navab, J. Hornegger, W. M. Wells, and A. F. Frangi, Eds., in Lecture Notes in Computer Science. Cham: Springer International Publishing, 2015, pp. 234–241. doi: 10.1007/978-3-319-24574-4_28.
[59] L. Fang *et al.*, "Deep learning-based point-scanning super-resolution imaging," *Nat Methods*, vol. 18, no. 4, Art. no. 4, Apr. 2021, doi: 10.1038/s41592-021-01080-z.
[60] I. Goodfellow *et al.*, "Generative Adversarial Nets," in *Advances in Neural Information Processing Systems 27*, Z. Ghahramani, M. Welling, C. Cortes, N. D. Lawrence, and K. Q. Weinberger, Eds., Curran Associates, Inc., 2014, pp. 2672–2680. Accessed: Mar. 27, 2020. [Online]. Available: http://papers.nips.cc/paper/5423-generative-adversarial-nets.pdf
[61] C. Ledig *et al.*, "Photo-Realistic Single Image Super-Resolution Using a Generative Adversarial Network," in *2017 IEEE Conference on Computer Vision and Pattern Recognition (CVPR)*, Jul. 2017, pp. 105–114. doi: 10.1109/CVPR.2017.19.
[62] A. Radford, L. Metz, and S. Chintala, "Unsupervised Representation Learning with Deep Convolutional Generative Adversarial Networks," *arXiv:1511.06434 [cs]*, Jan. 2016, Accessed: Jan. 21, 2020. [Online]. Available: http://arxiv.org/abs/1511.06434
[63] D. S. Gareau, "The feasibility of digitally stained multimodal confocal mosaics to simulate histopathology," *J Biomed Opt*, vol. 14, no. 3, p. 034050, 2009, doi: 10.1117/1.3149853.
[64] D. A. Orringer *et al.*, "Rapid intraoperative histology of unprocessed surgical specimens via fibre-laser-based stimulated Raman scattering microscopy," *Nature Biomedical Engineering*, vol. 1, no. 2, Art. no. 2, Feb. 2017, doi: 10.1038/s41551-016-0027.
[65] M. G. Giacomelli *et al.*, "Virtual Hematoxylin and Eosin Transillumination Microscopy Using Epi-Fluorescence Imaging," *PLOS ONE*, vol. 11, no. 8, p. e0159337, Aug. 2016, doi: 10.1371/journal.pone.0159337.
[66] B. Bai, X. Yang, Y. Li, Y. Zhang, N. Pillar, and A. Ozcan, "Deep learning-enabled virtual histological staining of biological samples," *Light Sci Appl*, vol. 12, no. 1, Art. no. 1, Mar. 2023, doi: 10.1038/s41377-023-01104-7.
[67] Y. Rivenson *et al.*, "Virtual histological staining of unlabelled tissue-autofluorescence images via deep learning," *Nature Biomedical Engineering*, vol. 3, no. 6, Art. no. 6, Jun. 2019, doi: 10.1038/s41551-019-0362-y.
[68] Y. Rivenson *et al.*, "PhaseStain: the digital staining of label-free quantitative phase microscopy images using deep learning," *Light: Science & Applications*, vol. 8, no. 1, Art. no. 1, Feb. 2019, doi: 10.1038/s41377-019-0129-y.
[69] Y. N. Nygate *et al.*, "HoloStain: Holographic virtual staining of individual biological cells," p. 20.
[70] M. Combalia *et al.*, "Digitally Stained Confocal Microscopy through Deep Learning," in *International Conference on Medical Imaging with Deep Learning*, PMLR, May 2019, pp. 121–

129. Accessed: Apr. 14, 2021. [Online]. Available: http://proceedings.mlr.press/v102/combalia19a.html
[71] K. B. Ozyoruk *et al.*, "A deep-learning model for transforming the style of tissue images from cryosectioned to formalin-fixed and paraffin-embedded," *Nat. Biomed. Eng*, vol. 6, no. 12, Art. no. 12, Dec. 2022, doi: 10.1038/s41551-022-00952-9.
[72] K. de Haan, Y. Rivenson, Y. Wu, and A. Ozcan, "Deep-Learning-Based Image Reconstruction and Enhancement in Optical Microscopy," *Proceedings of the IEEE*, vol. 108, no. 1, pp. 30–50, Jan. 2020, doi: 10.1109/JPROC.2019.2949575.
[73] F. Fereidouni *et al.*, "Microscopy with ultraviolet surface excitation for rapid slide-free histology," *Nature Biomedical Engineering*, vol. 1, no. 12, Art. no. 12, Dec. 2017, doi: 10.1038/s41551-017-0165-y.
[74] Y. Rivenson *et al.*, "Virtual histological staining of unlabelled tissue-autofluorescence images via deep learning," *Nature Biomedical Engineering*, vol. 3, no. 6, pp. 466–477, Jun. 2019, doi: 10.1038/s41551-019-0362-y.
[75] Y. Rivenson, T. Liu, Z. Wei, Y. Zhang, K. de Haan, and A. Ozcan, "PhaseStain: the digital staining of label-free quantitative phase microscopy images using deep learning," *Light Sci Appl*, vol. 8, no. 1, pp. 1–11, Feb. 2019, doi: 10.1038/s41377-019-0129-y.
[76] N. Borhani, A. J. Bower, S. A. Boppart, and D. Psaltis, "Digital staining through the application of deep neural networks to multi-modal multi-photon microscopy," *Biomed. Opt. Express, BOE*, vol. 10, no. 3, pp. 1339–1350, Mar. 2019, doi: 10.1364/BOE.10.001339.
[77] I. Goodfellow *et al.*, "Generative Adversarial Nets," in *Advances in Neural Information Processing Systems 27*, Z. Ghahramani, M. Welling, C. Cortes, N. D. Lawrence, and K. Q. Weinberger, Eds., Curran Associates, Inc., 2014, pp. 2672–2680. Accessed: Jan. 21, 2020. [Online]. Available: http://papers.nips.cc/paper/5423-generative-adversarial-nets.pdf
[78] J.-Y. Zhu, T. Park, P. Isola, and A. A. Efros, "Unpaired Image-to-Image Translation Using Cycle-Consistent Adversarial Networks," in *2017 IEEE International Conference on Computer Vision (ICCV)*, Venice: IEEE, Oct. 2017, pp. 2242–2251. doi: 10.1109/ICCV.2017.244.
[79] Z. Yi, H. Zhang, P. Tan, and M. Gong, "DualGAN: Unsupervised Dual Learning for Image-to-Image Translation," in *2017 IEEE International Conference on Computer Vision (ICCV)*, Oct. 2017, pp. 2868–2876. doi: 10.1109/ICCV.2017.310.
[80] S. Hicsonmez, N. Samet, E. Akbas, and P. Duygulu, "GANILLA: Generative adversarial networks for image to illustration translation," *Image and Vision Computing*, vol. 95, p. 103886, Mar. 2020, doi: 10.1016/j.imavis.2020.103886.
[81] P. Isola, J.-Y. Zhu, T. Zhou, and A. A. Efros, "Image-to-Image Translation with Conditional Adversarial Networks," in *2017 IEEE Conference on Computer Vision and Pattern Recognition (CVPR)*, Jul. 2017, pp. 5967–5976. doi: 10.1109/CVPR.2017.632.
[82] M. Arjovsky, S. Chintala, and L. Bottou, "Wasserstein GAN," *arXiv:1701.07875 [cs, stat]*, Dec. 2017, Accessed: Mar. 27, 2020. [Online]. Available: http://arxiv.org/abs/1701.07875
[83] A. Paszke *et al.*, "PyTorch: An Imperative Style, High-Performance Deep Learning Library," in *Advances in Neural Information Processing Systems 32*, H. Wallach, H. Larochelle, A. Beygelzimer, F. d\textquotesingle Alché-Buc, E. Fox, and R. Garnett, Eds., Curran Associates, Inc., 2019, pp. 8026–8037. Accessed: Mar. 27, 2020. [Online]. Available: http://papers.nips.cc/paper/9015-pytorch-an-imperative-style-high-performance-deep-learning-library.pdf
[84] J. Howard and S. Gugger, "Fastai: A Layered API for Deep Learning," *Information*, vol. 11, no. 2, Art. no. 2, Feb. 2020, doi: 10.3390/info11020108.
[85] X. Li *et al.*, "Unsupervised content-preserving transformation for optical microscopy," *Light: Science & Applications*, vol. 10, no. 1, Art. no. 1, Mar. 2021, doi: 10.1038/s41377-021-00484-y.
[86] Z. Wang, A. C. Bovik, H. R. Sheikh, and E. P. Simoncelli, "Image quality assessment: from error visibility to structural similarity," *IEEE Transactions on Image Processing*, vol. 13, no. 4, pp. 600–612, Apr. 2004, doi: 10.1109/TIP.2003.819861.

[87] M. Wang *et al.*, "High-Resolution Rapid Diagnostic Imaging of Whole Prostate Biopsies Using Video-Rate Fluorescence Structured Illumination Microscopy," *Cancer Res.*, vol. 75, no. 19, pp. 4032–4041, Oct. 2015, doi: 10.1158/0008-5472.CAN-14-3806.
[88] J. Dobbs, S. Krishnamurthy, M. Kyrish, A. P. Benveniste, W. Yang, and R. Richards-Kortum, "Confocal fluorescence microscopy for rapid evaluation of invasive tumor cellularity of inflammatory breast carcinoma core needle biopsies," *Breast Cancer Res Treat*, vol. 149, no. 1, pp. 303–310, Jan. 2015, doi: 10.1007/s10549-014-3182-5.
[89] T. T. W. Wong *et al.*, "Fast label-free multilayered histology-like imaging of human breast cancer by photoacoustic microscopy," *Science Advances*, vol. 3, no. 5, p. e1602168, May 2017, doi: 10.1126/sciadv.1602168.
[90] T. N. Engel *et al.*, "Pilot study of fluorescence imitating brightfield imaging for rapid, slide-free dermatopathology," *Journal of Cutaneous Pathology*, vol. 49, no. 12, pp. 1060–1066, 2022, doi: 10.1111/cup.14308.
[91] N. T. Goldsmith, "DEEP FOCUS; A DIGITAL IMAGE PROCESSING TECHNIQUE TO PRODUCE IMPROVED FOCAL DEPTH IN LIGHT MICROSCOPY," *Image Analysis & Stereology*, vol. 19, no. 3, Art. no. 3, 2000, doi: 10.5566/ias.v19.p163-167.
[92] Y. Wu, V. Boominathan, H. Chen, A. Sankaranarayanan, and A. Veeraraghavan, "PhaseCam3D — Learning Phase Masks for Passive Single View Depth Estimation," in *2019 IEEE International Conference on Computational Photography (ICCP)*, May 2019, pp. 1–12. doi: 10.1109/ICCPHOT.2019.8747330.
[93] P. Bankhead *et al.*, "QuPath: Open source software for digital pathology image analysis," *Scientific Reports*, vol. 7, no. 1, Art. no. 1, Dec. 2017, doi: 10.1038/s41598-017-17204-5.
[94] T. Abraham, A. Shaw, D. O'Connor, A. Todd, and R. Levenson, "Slide-free MUSE Microscopy to H&E Histology Modality Conversion via Unpaired Image-to-Image Translation GAN Models," *arXiv:2008.08579 [cs, eess]*, Aug. 2020, Accessed: Sep. 11, 2020. [Online]. Available: http://arxiv.org/abs/2008.08579
[95] D. A. Orringer and S. Camelo-Piragua, "Fast and slide-free imaging," *Nat Biomed Eng*, vol. 1, no. 12, pp. 926–928, Dec. 2017, doi: 10.1038/s41551-017-0172-z.
[96] E. Yew, C. Rowlands, and P. T. C. So, "Application of Multiphoton Microscopy in Dermatological Studies: a Mini-Review," *J Innov Opt Health Sci*, vol. 7, no. 5, p. 1330010, Jan. 2014, doi: 10.1142/S1793545813300103.
[97] E. Dalimier and D. Salomon, "Full-field optical coherence tomography: a new technology for 3D high-resolution skin imaging," *Dermatology*, vol. 224, no. 1, pp. 84–92, 2012, doi: 10.1159/000337423.
[98] J. R. Durkin, J. L. Fine, H. Sam, M. Pugliano-Mauro, and J. Ho, "Imaging of Mohs micrographic surgery sections using full-field optical coherence tomography: a pilot study," *Dermatol Surg*, vol. 40, no. 3, pp. 266–274, Mar. 2014, doi: 10.1111/dsu.12419.
[99] S. Abadie *et al.*, "3D imaging of cleared human skin biopsies using light-sheet microscopy: A new way to visualize in-depth skin structure," *Skin Research and Technology*, vol. 24, no. 2, pp. 294–303, 2018, doi: https://doi.org/10.1111/srt.12429.
[100] C. W. Freudiger *et al.*, "Label-Free Biomedical Imaging with High Sensitivity by Stimulated Raman Scattering Microscopy," *Science*, vol. 322, no. 5909, pp. 1857–1861, Dec. 2008, doi: 10.1126/science.1165758.
[101] R. Mittal *et al.*, "Evaluation of Stimulated Raman Scattering Microscopy for Identifying Squamous Cell Carcinoma in Human Skin," *Lasers Surg Med*, vol. 45, no. 8, pp. 496–502, Oct. 2013, doi: 10.1002/lsm.22168.
[102] A. D. Borowsky *et al.*, "Digital Whole Slide Imaging Compared With Light Microscopy for Primary Diagnosis in Surgical Pathology: A Multicenter, Double-Blinded, Randomized Study of 2045 Cases," *Archives of Pathology & Laboratory Medicine*, vol. 144, no. 10, pp. 1245–1253, Feb. 2020, doi: 10.5858/arpa.2019-0569-OA.

[103] M. K. K. Niazi, A. V. Parwani, and M. N. Gurcan, "Digital pathology and artificial intelligence," *The Lancet Oncology*, vol. 20, no. 5, pp. e253–e261, May 2019, doi: 10.1016/S1470-2045(19)30154-8.
[104] S. Chatterjee, "Artefacts in histopathology," *J Oral Maxillofac Pathol*, vol. 18, no. Suppl 1, pp. S111–S116, Sep. 2014, doi: 10.4103/0973-029X.141346.
[105] B. Schömig-Markiefka *et al.*, "Quality control stress test for deep learning-based diagnostic model in digital pathology," *Mod Pathol*, pp. 1–11, Jun. 2021, doi: 10.1038/s41379-021-00859-x.
[106] C.-K. Sun *et al.*, "Slide-free imaging of hematoxylin-eosin stained whole-mount tissues using combined third-harmonic generation and three-photon fluorescence microscopy," *J Biophotonics*, vol. 12, no. 5, p. e201800341, May 2019, doi: 10.1002/jbio.201800341.
[107] E. Tkaczyk, "Innovations and Developments in Dermatologic Non-invasive Optical Imaging and Potential Clinical Applications," *Acta Derm Venereol*, vol. Suppl 218, pp. 5–13, 2017, doi: 10.2340/00015555-2717.
[108] K. de Haan *et al.*, "Deep learning-based transformation of H&E stained tissues into special stains," *Nat Commun*, vol. 12, no. 1, Art. no. 1, Aug. 2021, doi: 10.1038/s41467-021-25221-2.
[109] A. K. Glaser *et al.*, "Light-sheet microscopy for slide-free non-destructive pathology of large clinical specimens," *Nature Biomedical Engineering*, vol. 1, no. 7, Art. no. 7, Jun. 2017, doi: 10.1038/s41551-017-0084.
[110] F. Jamme *et al.*, "Deep UV autofluorescence microscopy for cell biology and tissue histology," *Biology of the Cell*, vol. 105, no. 7, pp. 277–288, 2013, doi: 10.1111/boc.201200075.
[111] K. B. Patel *et al.*, "High-speed light-sheet microscopy for the in-situ acquisition of volumetric histological images of living tissue," *Nat. Biomed. Eng*, vol. 6, no. 5, Art. no. 5, May 2022, doi: 10.1038/s41551-022-00849-7.
[112] S. Ye *et al.*, "Rapid and label-free histological imaging of unprocessed surgical tissues via dark-field reflectance ultraviolet microscopy," *iScience*, vol. 26, no. 1, Jan. 2023, doi: 10.1016/j.isci.2022.105849.
[113] H. Tu *et al.*, "Stain-free histopathology by programmable supercontinuum pulses," *Nature Photonics*, vol. 10, no. 8, pp. 534–540, Aug. 2016, doi: 10.1038/nphoton.2016.94.
[114] S. Witte *et al.*, "Label-free live brain imaging with third-harmonic generation microscopy," in *CLEO/Europe and EQEC 2011 Conference Digest (2011), paper CLEB1_1*, Optica Publishing Group, May 2011, p. CLEB1_1. Accessed: Apr. 25, 2023. [Online]. Available: https://opg.optica.org/abstract.cfm?uri=CLEO_Europe-2011-CLEB1_1
[115] M. Ji *et al.*, "Rapid, label-free detection of brain tumors with stimulated Raman scattering microscopy," *Sci Transl Med*, vol. 5, no. 201, p. 201ra119, Sep. 2013, doi: 10.1126/scitranslmed.3005954.
[116] P. Ledwig and F. E. Robles, "Epi-mode tomographic quantitative phase imaging in thick scattering samples," *Biomed Opt Express*, vol. 10, no. 7, pp. 3605–3621, Jun. 2019, doi: 10.1364/BOE.10.003605.
[117] P. Ledwig and F. E. Robles, "Quantitative 3D refractive index tomography of opaque samples in epi-mode," *Optica, OPTICA*, vol. 8, no. 1, pp. 6–14, Jan. 2021, doi: 10.1364/OPTICA.410135.
[118] J. Li *et al.*, "Biopsy-free in vivo virtual histology of skin using deep learning," *Light Sci Appl*, vol. 10, no. 1, Art. no. 1, Nov. 2021, doi: 10.1038/s41377-021-00674-8.
[119] M. Boktor *et al.*, "Virtual histological staining of label-free total absorption photoacoustic remote sensing (TA-PARS)," *Sci Rep*, vol. 12, no. 1, Art. no. 1, Jun. 2022, doi: 10.1038/s41598-022-14042-y.
[120] S. Zhao *et al.*, "Intraoperative fluorescence-guided resection of high-grade malignant gliomas using 5-aminolevulinic acid-induced porphyrins: a systematic review and meta-analysis of prospective studies," *PLoS One*, vol. 8, no. 5, p. e63682, 2013, doi: 10.1371/journal.pone.0063682.
[121] C. G. Hadjipanayis, G. Widhalm, and W. Stummer, "What is the Surgical Benefit of Utilizing 5-ALA for Fluorescence-Guided Surgery of Malignant Gliomas?," *Neurosurgery*, vol. 77, no. 5, pp. 663–673, Nov. 2015, doi: 10.1227/NEU.0000000000000929.

[122] J.-C. Tonn and W. Stummer, “Fluorescence-guided resection of malignant gliomas using 5-aminolevulinic acid: practical use, risks, and pitfalls,” *Clin Neurosurg*, vol. 55, pp. 20–26, 2008.
[123] P. A. Valdés *et al.*, “δ-aminolevulinic acid-induced protoporphyrin IX concentration correlates with histopathologic markers of malignancy in human gliomas: the need for quantitative fluorescence-guided resection to identify regions of increasing malignancy,” *Neuro Oncol*, vol. 13, no. 8, pp. 846–856, Aug. 2011, doi: 10.1093/neuonc/nor086.
[124] B. A. Kairdolf *et al.*, “Intraoperative Spectroscopy with Ultrahigh Sensitivity for Image-Guided Surgery of Malignant Brain Tumors,” *Anal Chem*, vol. 88, no. 1, pp. 858–867, Jan. 2016, doi: 10.1021/acs.analchem.5b03453.
[125] W. Stummer, H. J. Reulen, A. Novotny, H. Stepp, and J. C. Tonn, “Fluorescence-guided resections of malignant gliomas--an overview,” *Acta Neurochir Suppl*, vol. 88, pp. 9–12, 2003, doi: 10.1007/978-3-7091-6090-9_3.
[126] L. N. Smith, “A disciplined approach to neural network hyper-parameters: Part 1 -- learning rate, batch size, momentum, and weight decay.” arXiv, Apr. 24, 2018. doi: 10.48550/arXiv.1803.09820.
[127] Abraham, Tanishq Mathew, “UPIT - A fastai/PyTorch package for unpaired image-to-image translation.” GitHub, 2021. doi: 10.5281/ZENODO.7889405.
[128] Y. Winetraub *et al.*, “OCT2Hist: Non-Invasive Virtual Biopsy Using Optical Coherence Tomography.” medRxiv, p. 2021.03.31.21254733, Apr. 06, 2021. doi: 10.1101/2021.03.31.21254733.
[129] M. Oquab, L. Bottou, I. Laptev, and J. Sivic, “Learning and Transferring Mid-Level Image Representations using Convolutional Neural Networks,” presented at the Proceedings of the IEEE Conference on Computer Vision and Pattern Recognition, 2014, pp. 1717–1724. Accessed: Apr. 27, 2023. [Online]. Available: https://openaccess.thecvf.com/content_cvpr_2014/html/Oquab_Learning_and_Transferring_2014_CVPR_paper.html
[130] P. Casteleiro Costa, “Quantitative oblique back-illumination microscopy in the study of biomedical samples,” Georgia Institute of Technology, 2023.
[131] M. Li, J. Lin, Y. Ding, Z. Liu, J.-Y. Zhu, and S. Han, “GAN Compression: Efficient Architectures for Interactive Conditional GANs,” presented at the Proceedings of the IEEE/CVF Conference on Computer Vision and Pattern Recognition, 2020, pp. 5284–5294. Accessed: Apr. 25, 2023. [Online]. Available: https://openaccess.thecvf.com/content_CVPR_2020/html/Li_GAN_Compression_Efficient_Architectures_for_Interactive_Conditional_GANs_CVPR_2020_paper.html
[132] G. Campanella *et al.*, “Clinical-grade computational pathology using weakly supervised deep learning on whole slide images,” *Nat. Med.*, vol. 25, no. 8, pp. 1301–1309, 2019, doi: 10.1038/s41591-019-0508-1.
[133] M. Y. Lu *et al.*, “Data-efficient and weakly supervised computational pathology on whole-slide images,” *Nature Biomedical Engineering*, pp. 1–16, Mar. 2021, doi: 10.1038/s41551-020-00682-w.
[134] I. Zingman, S. Frayle, I. Tankoyeu, S. Sukhanov, and F. Heinemann, “A comparative evaluation of image-to-image translation methods for stain transfer in histopathology.” arXiv, Apr. 06, 2023. doi: 10.48550/arXiv.2303.17009.
[135] N. Altini *et al.*, “The role of unpaired image-to-image translation for stain color normalization in colorectal cancer histology classification,” *Computer Methods and Programs in Biomedicine*, vol. 234, p. 107511, Jun. 2023, doi: 10.1016/j.cmpb.2023.107511.
[136] J. Salido, N. Vallez, L. González-López, O. Deniz, and G. Bueno, “Comparison of deep learning models for digital H&E staining from unpaired label-free multispectral microscopy images,” *Computer Methods and Programs in Biomedicine*, vol. 235, p. 107528, Jun. 2023, doi: 10.1016/j.cmpb.2023.107528.
[137] D. Zha *et al.*, “Data-centric Artificial Intelligence: A Survey.” arXiv, Apr. 02, 2023. doi: 10.48550/arXiv.2303.10158.

[138] J. P. Cohen, M. Luck, and S. Honari, "Distribution Matching Losses Can Hallucinate Features in Medical Image Translation," May 2018, Accessed: Apr. 15, 2021. [Online]. Available: https://arxiv.org/abs/1805.08841v3
[139] M.-Y. Liu, T. Breuel, and J. Kautz, "Unsupervised Image-to-Image Translation Networks," *arXiv:1703.00848 [cs]*, Jul. 2018, Accessed: Apr. 15, 2021. [Online]. Available: http://arxiv.org/abs/1703.00848
[140] J. Kim, M. Kim, H. Kang, and K. Lee, "U-GAT-IT: Unsupervised Generative Attentional Networks with Adaptive Layer-Instance Normalization for Image-to-Image Translation," *arXiv:1907.10830 [cs, eess]*, Apr. 2020, Accessed: Apr. 15, 2021. [Online]. Available: http://arxiv.org/abs/1907.10830
[141] S. Benaim and L. Wolf, "One-Sided Unsupervised Domain Mapping," *arXiv:1706.00826 [cs]*, Nov. 2017, Accessed: Apr. 15, 2021. [Online]. Available: http://arxiv.org/abs/1706.00826
[142] R. Zhang, T. Pfister, and J. Li, "Harmonic Unpaired Image-to-image Translation," *arXiv:1902.09727 [cs]*, Feb. 2019, Accessed: Apr. 15, 2021. [Online]. Available: http://arxiv.org/abs/1902.09727
[143] Z. Jia *et al.*, "Lipschitz Regularized CycleGAN for Improving Semantic Robustness in Unpaired Image-to-image Translation," *arXiv:2012.04932 [cs]*, Dec. 2020, Accessed: Apr. 10, 2021. [Online]. Available: http://arxiv.org/abs/2012.04932
[144] H. Emami, M. M. Aliabadi, M. Dong, and R. B. Chinnam, "SPA-GAN: Spatial Attention GAN for Image-to-Image Translation," *arXiv:1908.06616 [cs]*, Dec. 2020, Accessed: Apr. 20, 2021. [Online]. Available: http://arxiv.org/abs/1908.06616
[145] T. Park, A. A. Efros, R. Zhang, and J.-Y. Zhu, "Contrastive Learning for Unpaired Image-to-Image Translation," *arXiv:2007.15651 [cs]*, Aug. 2020, Accessed: Apr. 20, 2022. [Online]. Available: http://arxiv.org/abs/2007.15651
[146] F. Mahmood, R. Chen, and N. J. Durr, "Unsupervised Reverse Domain Adaptation for Synthetic Medical Images via Adversarial Training," *IEEE Transactions on Medical Imaging*, vol. 37, no. 12, pp. 2572–2581, Dec. 2018, doi: 10.1109/TMI.2018.2842767.
[147] C. Yang, T. Kim, R. Wang, H. Peng, and C.-C. J. Kuo, "Show, Attend and Translate: Unsupervised Image Translation with Self-Regularization and Attention," *IEEE Trans. on Image Process.*, vol. 28, no. 10, pp. 4845–4856, Oct. 2019, doi: 10.1109/TIP.2019.2914583.
[148] P. Dhariwal and A. Nichol, "Diffusion Models Beat GANs on Image Synthesis." arXiv, Jun. 01, 2021. Accessed: Sep. 23, 2022. [Online]. Available: http://arxiv.org/abs/2105.05233
[149] C. Saharia *et al.*, "Palette: Image-to-Image Diffusion Models," in *Special Interest Group on Computer Graphics and Interactive Techniques Conference Proceedings*, Vancouver BC Canada: ACM, Aug. 2022, pp. 1–10. doi: 10.1145/3528233.3530757.
[150] X. Su, J. Song, C. Meng, and S. Ermon, "Dual Diffusion Implicit Bridges for Image-to-Image Translation." arXiv, Mar. 05, 2023. doi: 10.48550/arXiv.2203.08382.
[151] R. Rombach, A. Blattmann, D. Lorenz, P. Esser, and B. Ommer, "High-Resolution Image Synthesis with Latent Diffusion Models." arXiv, Apr. 13, 2022. Accessed: Sep. 20, 2022. [Online]. Available: http://arxiv.org/abs/2112.10752
[152] R. C. Niemeier *et al.*, "Sequential staining technique for acquiring paired images with H&E and microscopy with ultraviolet surface excitation (MUSE)," in *Photonics in Dermatology and Plastic Surgery 2022*, SPIE, Mar. 2022, pp. 20–25. doi: 10.1117/12.2610334.
[153] L. R. Dice, "Measures of the Amount of Ecologic Association Between Species," *Ecology*, vol. 26, no. 3, pp. 297–302, 1945, doi: 10.2307/1932409.
[154] D. M. Metter, T. J. Colgan, S. T. Leung, C. F. Timmons, and J. Y. Park, "Trends in the US and Canadian Pathologist Workforces From 2007 to 2017," *JAMA Netw Open*, vol. 2, no. 5, pp. e194337–e194337, May 2019, doi: 10.1001/jamanetworkopen.2019.4337.